NUMERICAL ANALYSIS OF MICROSTRIP STRUCTURES USING THE COMPLEX IMAGES METHOD

By

Ashraf Badawi

A Thesis

Submitted to the Faculty of Graduate Studies

in Partial Fulfillment of the Requirements

for the Degree of

Doctor of Philosophy

Department of Electrical and Computer Engineering

University of Manitoba

Winnipeg, Manitoba, Canada 2002

THE UNIVERSITY OF MANITOBA

FACULTY OF GRADUATE STUDIES

*****

COPYRIGHT PERMISSION

NUMERICAL ANALYSIS OF MICROSTRIP STRUCTURES USING THE COMPLEX IMAGES METHOD

BY

ASHRAF BADAWI

A Thesis/Practicum submitted to the Faculty of Graduate Studies of The University of Manitoba in partial fulfillment of the requirement of the degree

of

DOCTOR OF PHILOSOPHY

Acknowledgments

I would like to express my deep and sincere gratitude to my advisor *Professor Sebak* for his constant patience, and careful guidance throughout the course of this research. I learned and gained so much working with him on the professional as well as the personal levels. His advice and directive comments were key ingredients in this accomplishment.

Special recognition to the members of my supervising committee for their constructive comments and suggestions. Also, I gratefully acknowledge the financial assistance from *University of Manitoba and NSERC.*

My parents, to whom I dedicate this thesis, are the main motivation and inspiration behind me getting to where I am today. They never ceased to encourage and support me, and they never lost their faith in me.

I apologize to my *children* as I was not there for them as much as I should have. And I thank my entire *family and friends* for their emotions, prayers and encouragement.

Last but not least, to my beloved *wife*, I could not have made it without you.

Abstract

This thesis presents an efficient full wave numerical analysis method for three dimensional microstrip structures inside a stratified media. The method can analyze both vertical and horizontal components of the currents. The conducting structures are modeled using a mixed potential integral equation (MPIE). The boundary conditions on the interfaces between dielectric layers are satisfied through the use of appropriate dyadic Green's functions in the spectral domain. Numerical evaluation of Sommerfeld integrals that are encountered during the transformation of the Green's function to the spatial domain is avoided using the complex images method (CIM). A modified CIM is proposed for efficient solution of vertical conductors currents. The modification maintains the rigorous nature of the full-wave analysis method while achieving the same numerical efficiency for both vertical and horizontal components of currents. The frequency sweep is made more efficient by interpolating the coefficients of the complex images used to represent the Green's functions in the spatial domain.

The CIM is combined with the MPIE and the method of moments (MoM) to produce a versatile numerical analysis tool for printed geometries in multilayered media. The numerical accuracy and convergence of the tool is established via an analytical benchmark. The accuracy of the method is also tested against commercially available full-wave analysis packages. Good agreement is obtained for a wide class of stacked microstrip antennas and circuits. The resulting analysis tool is applied successfully to the numerical analysis of microstrip antennas, and for a variety of feeding techniques. The tool is also

applied to the analysis of microwave circuits, and passive MMIC components in the presence of finite ground planes, slots in the ground plane and to a wide frequency band interconnects. The tool is used to accurately predict the radiated emissions levels from printed interconnect structures. An efficient radiation susceptibility prediction procedure is suggested based on the analysis tool. In combination with time domain convolution, the tool is used to analyze interconnect systems with active circuits in the time domain. This approach does not compromise the accuracy of the analysis of the active circuit nor the interconnect system.

TABLE OF CONTENTS

LIST OF FIGURES

LIST OF TABLES

CHAPTER 1

Introduction and Motivation

1.1 Introduction

Microstrip antennas and circuits that are made of more than one dielectric layer are now widely used in the microwave industry. For optimum design of multilayered structures, it is important that an accurate and computationally efficient method be developed. Several methods have been presented in the literature to analyze these kinds of multilayer structures. Numerous obstacles impede the development of a general-purpose and efficient modeling technique for such structures. One of these obstacles is the increasing diversity of designs and dielectric layer configurations. The numerical technique developed should also have the capability of analyzing various kinds of antenna feeding mechanisms encountered, such as line feeding, probe feeding, and aperture coupled structures.

Furthermore, the introduction of microstrip technology to higher frequency ranges, such as the mm-wave range (frequency > 30GHz), has complicated analysis procedures and numerical computations for arbitrarily shaped microstrip structures. Most solution methods make assumptions based on relative dimensions of the structure with respect to the operating wavelength. Many of these assumptions become invalid in the mm-wave range.

Additionally, the nature of the wave propagation in the dielectric media is altered in that range, with a larger proportion of the wave propagating as surface waves. Only rigorous full wave analysis methods can achieve the required accuracy at these frequency ranges, while maintaining enough flexibility to handle a diverse assortment of geometries.

An extensive and substantial amount of research is reported in the literature towards predicting, verifying, designing and trying to understand and analyze the operation of multilayer antennas and circuits. The purpose of this thesis is to obtain a suitable, accurate and numerically efficient mathematical model which is applicable to a wide variety of microstrip structures, and operating frequency ranges.

1.2 Microstrip Antenna Analysis Models

The main objectives of antenna analysis are to predict the radiation characteristics as well as the near field characteristics [1]. The former includes the radiation pattern, gain and polarization. While the latter includes such characteristics like the input impedance and mutual coupling. The presence of dielectric inhomogeneity, inhomogenous boundary conditions, patch shape and substrate configurations or a variety of feed complicate the analysis of microstrip antennas. Numerous models have been reported in the literature to carry out the numerical analysis of microstrip antennas. These models can be divided into two main categories. The first category includes those models that are based on the simplified analysis, these models achieve simplicity at the cost of accuracy. The second category includes models that are based on full-wave methods. These models offer a better accuracy and provide more information about the interaction of microstrip antennas and their feed networks at the expense of being more complex.

1.2.1 Simplified Analysis Models

The simplified analysis models are based on analytical techniques. These analytical techniques include the transmission line model, the cavity model, the multiport network model and their modified versions. The analytical models were the first to be developed for the analysis of microstrip antennas. They offer simple and analytical solutions that are useful for practical design and provide a simple explanation of the physical phenomena and the operation of the microstrip antenna.

The simplified analysis models use simplifying assumptions to achieve analytical simplicity in the form of closed form eigenfunctions. Closed-form expressions are used for the wall admittance, which make these techniques less computer intensive. To account for various phenomena such as space wave radiation, surface wave radiation and mutual coupling, they employ an add-on approach. In general, these analysis models suffer from a number of limitations. For example, they are only accurate when applied to analyze microstrip antennas with thin substrates and are inaccurate when applied to narrow width microstrip dipoles. Furthermore, these models suffer from the difficulty to model some feed configurations including aperture coupled and proximity coupled microstrip feeds.

1.2.1.1 Transmission Line Models

The physical shapes of rectangular, square and circular patches, annular rings and sectors of circular patches and annular rings make them convenient to model these antennas as sections of transmission lines. The transmission line model was the first technique employed to analyze rectangular microstrip antennas [2]. The interior region of the patch antenna is modeled as a section of transmission line. The characteristic impedance and the

propagation constant of the transmission line are determined by the patch size and substrate parameters. The four walls or edges of the patch can be classified as radiating or nonradiating based on the nature of the field variation along the length of each edge. The effect of the substrate on the input impedance and the radiation is not considered. This transmission line model was approximate and very simple and was only applicable to rectangular patches.

One modification to include the effect of mutual coupling between the radiating edges was introduced in [3]. This was maintained by including a mutual admittance connected between the two ends of the transmission line. The feed, microstrip or coaxial line, can be represented by an ideal current source at the feed point along the transmission line. The input impedance is determined through obtaining the voltage across the feed. This modification allowed for the modeling and analysis of microstrip fed rectangular patch antenna [3], design of a matched broadband rectangular patch antenna [4], calculation of mutual coupling between rectangular patches [5] and prediction of wide band performance of microstrip antennas [6]. Yet, this modified model is only applicable to rectangular and square microstrip patches only. Furthermore, the variation of fields along the width of the patch is not considered and only microstrip line and coaxial feeds can be analyzed.

The analysis of a wide variety of patches that are not necessarily rectangular, required the use of a more versatile technique which is the generalized transmission line model [7]-[8]. The major difference between the transmission line model and the generalized transmission line model is that a patch in the latter is modeled using transmission lines in orthogonal directions. This led to the ability to model the variation of fields along the transverse direction. In order to handle nonrectangular geometries, the used

transmission lines are nonuniform.

One way to modify the generalized transmission line model is to assume a TEM mode approximation along the symmetry axis of the patch [9]. In which case, various losses like the radiation loss, dielectric loss and copper loss are combined and assumed distributed along the length of a transmission line in the form of increased dielectric loss. The transmission line section is divided into a number of small sized sections, each of which has a particular strip width, effective dielectric constant and characteristic impedance. Using the constraint that the power delivered to the lossy transmission line equals the radiated power, the radiation admittance can be obtained. This model has been applied to a number of geometries including rectangular patch, circular patch, stacked antenna geometry, microstrip fed radiating slot and folded dipoles [9]-[10].

1.2.1.2 Cavity Model

The use of the cavity model [11] in the analysis of microstrip antennas is an improvement over the transmission line model as the variation of the field along the transverse direction is accounted for. Being narrow band resonant antennas, microstrip patch antennas can be considered as lossy cavities, which in turn makes the choice of the cavity model to analyze them very convenient. In this model, the interior region of the patch is modeled as a cavity bounded by electric walls on the top and bottom and a magnetic wall along the periphery. This is done under the assumptions that the substrate is thin which implies that the interior region fields do not vary with z, the electric field is only z directed and the magnetic field has only the transverse components in the region bounded by the patch metallization and the ground plane. Also, the assumption that the tangential

component of the magnetic field along the edge is negligible.

The field distribution in the patch can be divided into two regions, the interior fields and the exterior fields. To determine the interior fields, a magnetic wall is assumed all around the periphery of the patch at a certain outward extension. This outward extension takes into account the energy stored in the fringing fields. The interior electric field distribution is obtained in terms of eigenfunctions of the cavity. These eigenfunctions depend on the shape and size of the patch metallization and not on the substrate parameters. The interior fields are then used to determine the input impedance of the antenna. Various types of losses can be included in the cavity model in the form of an effective loss tangent. These include dielectric loss, conductor loss and radiation loss.

The cavity model has also been generalized to analyze nonseparable geometries [12]. The nonseparable geometry is first converted into an equivalent geometry with magnetic walls at the peripheries. The outward extension is based on an educated guess. For nonrectangular geometries, an extension equal to the substrate thickness works well for thin, low dielectric constant substrates. The next step is to segment the geometry with magnetic wall into regular geometries for which eigenfunctions are available. The planar circuit approach is then applied to determine the electric and magnetic fields under the patch. The quality factor Q of the patch's cavity is then calculated and finally the input impedance can be obtained from the ratio of the voltage and current at the feed point. This generalized model has been used to analyze some complex geometries such as rectangular and square rings, a cross shaped patch, an H-shaped patch and a two-port circular patch [13]-[15].

1.2.1.3 Multiport Network Model

The multiport network model [4] can be considered as an extension of the cavity model in which the impedance boundary condition at the periphery is enforced explicitly taking into account the mutual coupling between various edges. In this model, fields in the interior and exterior regions are modeled separately. The interior region is modeled as a multiport planar circuit with the ports located along the periphery, while fields in the exterior region are represented by load admittances. Unlike the transmission line model, all edges, radiating or nonradiating, can be represented as load admittances. Furthermore, the load admittance corresponding to a given edge is equally divided into a number of ports. These loads are then connected to the corresponding ports on the planar circuit. Thus, for a given edge, the number of ports on the multiport network and the load network are identical.

One of the major advantages of this model is the ability to handle and include in the analysis any discontinuity in the patch. The multiport network model has been used to analyze a variety of microstrip antennas including pentagonal shaped patches [16], broadband gap-coupled multiresonator rectangular patches [17] and proximity-coupled rectangular microstrip antennas [18]. It has also been applied to rectangular patches, circular polarization from truncated square patches [19], square patches with diagonal slots [20], direct coupled rectangular patches and two-port rectangular patches [21].

1.2.2 Full-Wave Analysis Models

The limitations of the simplified analysis models can be overcome through the use of full-wave techniques for the analysis of microstrip antennas. These techniques maintain

rigor and accuracy at the expense of simplicity. The full-wave solutions include the effects of the dielectric loss, conductor loss, space wave radiation, surface waves and external coupling. Furthermore, they can be used for arbitrarily shaped microstrip elements and arrays, different kinds of feeding mechanisms, multilayer anisotropic substrates and active antennas. In general, they provide the most accurate solution for the impedance and radiation characteristics. The full-wave analysis models, for arbitrarily shaped microstrip structures, can be divided into two groups, the first is the differential equation based models while the second is the integral equation based models.

1.2.2.1 Differential Equation Based Models

The analysis of the microstrip antennas using differential equation based models like the transmission line matrix (TLM) method [22] and the finite difference time domain (FDTD) [23] have been extensively studied. These models are based on the differential form of Maxwell's equations in time domain. They require the discretization of the entire spatial domain of interest. These models are capable of analyzing microstrip structures on both finite and infinite substrate or ground plane. They are also capable of predicting broad band frequency domain response because the analysis is carried out in the time domain and Fast Fourier Transform (FFT) is used to obtain the frequency domain response. Despite the fact that the differential equation based models are capable of analyzing a wide variety of microstrip antennas, the large amount of computation required for the analysis makes them an inefficient design tool for microstrip antennas and circuits. Numerical analysis of microstrip antenna arrays and electrically large circuits is prohibitively inefficient using these techniques. In today's microstrip antenna CAD environment, the application of the

FDTD and TLM is limited to inhomogenous structures that are difficult to handle using other numerical techniques.

Analysis of EM scattering or radiation problems using the TLM or the FDTD starts by dividing the structure into various regions based on the material properties. The unbounded region, if any, is rendered bounded by terminating it with absorbing medium or termination so that reflections do not occur. Next, the problem's physical space is discretized in the form of a number of cuboids. The time domain is also discretized with a certain interval size. The structure is then excited by an electromagnetic pulse. The wave launched by the pulse in the structure is then studied for its propagation behavior.

In the analysis of microstrip antennas using the TLM method, the conducting surfaces are considered to be perfectly conducting and infinitely thin. The substrates are modeled by specifying appropriate stub values to model permittivity, permeability and conductivity. Match terminations for normal incidence boundary conditions are applied to terminate the exterior mesh boundaries. Due to the requirement of modeling the antenna and the free space region surrounding the antenna, the size of the simulation space required for analyzing microstrip antennas on a finite substrate or ground plane is usually prohibitively large. TLM based models have been applied to analysis of microstrip patch antenna on ferrite substrate [24], mutual coupling of microstrip patch antenna arrays [25], cross-aperture coupled patch [26] and a variety of other microstrip-antenna and circuit structures [27].

In the FDTD, the conducting surfaces are assumed to be perfectly conducting and of zero thickness similar to the TLM. They are thus treated by setting the tangential components of the electric fields to zero. The edge of the conducting surface is modeled

with the tangential electric field components lying exactly on the edge of the microstrip. The remaining five boundaries have to be truncated using suitable absorbing boundary conditions. The FDTD has been used to analyze rectangular patch antenna [28], modeling of a dispersive microstrip antenna [29] and to calculate the reflection coefficient of various microstrip patch configurations [30]. The technique has also been used in the analysis of the mutual coupling between two microstrip antennas [31], as well as, the analysis of microstrip antennas on a curved surface [32]. Moreover, the FDTD has been used to obtain the radar cross section of microstrip patch antennas, and to model the radiation from microstrip patches with a ferrite substrate [33]-[35].

1.2.2.2 Integral Equation Based Models

The integral equation formulations are set up to find unknown source distributions, currents and charges densities, inside the solution domain. They involve the utilization of Green's functions, in the frequency domain, to account for any analytically manageable boundary condition between the material interfaces. The unknown distributions are determined via the Method of Moments (MoM) [36]. The MoM requires the discretization of the unknown distribution, and sets up a set of linear equations that are solved using matrix methods.

The application of the electric field integral equation (EFIE) technique for electric current only [37]-[38], requires segmenting the entire volume of the structure, including the microstrip ground plane, and the dielectric substrate. This formulation is called the volume integral equation, for the volume polarization currents inside the dielectrics. The Green's function used in the volume integral equation is the free space dyadic Green's function,

which is the simplest form for that function and the easiest to manipulate numerically. The volume integral equation is numerically inefficient for solving multilayered problems, as the MoM matrix size becomes excessively large (several thousand unknowns for a simple structure).

If both electric and magnetic currents are used the resulting formulation is called the surface integral equation, with the added mathematical complexity associated with presence of the two types of currents on the surfaces. In general, the surface integral equation involves a smaller number of unknowns, than the volume integral equation for the same structure. When the surface integral equation is restricted to rotationally symmetric structures, the resulting technique becomes efficient. The structure is essentially reduced to a two dimensional structure and the number of unknowns is small. The drawback for this method is its restriction to a certain class of structures, which is rotationally symmetric.

Considering the fact that the majority of microstrip structures are embedded in stratified dielectric media, the boundary conditions between these layers can be accounted for in the derivation of the specialized dyadic Green's functions. Different derivations for these Green's functions are given by several authors [39]-[52].

In conjunction with these specialized Green's functions, the mixed potential integral equation (MPIE) [4] is an accurate and efficient method for characterization of microstrip structures. It allows for the discretization of the electric currents on the conductors only. The term mixed potential is used because a combination of vector and scalar potential functions is used for the analysis. For a general microstrip structure, a smaller MoM matrix would result using the MPIE than either the volume or surface integral equations. The combination of the MPIE and MoM sets up a powerful analysis tool for

various printed geometries in a multilayer dielectric media. For stratified media problems, the MPIE can be solved in two different ways:

1. The integral equation is written and solved in the spectral domain [53]-[55]. This approach is frequently termed the spectral domain approach.

2. In the other approach the spectral domain is used for calculating the Green's functions, but inverse transforms are taken at this stage and the integral equation is solved in the space domain [56]-[63]. Applying the MoM in the spatial domain has the advantage of evaluating the integrands of the MoM matrix elements only over a finite interval for the subsectional basis and testing functions. The method also provides more physical insight into the problem. On the other hand, it requires the evaluation of relevant Green's functions in the spatial domain. This requires the calculation of the inverse Hankel transform of these functions, known as Sommerfeld integrals (SIs). The direct numerical integration of the SIs is a computationally intensive and time-consuming operation.

1.3 Evaluating the Sommerfeld Integrals

The integrated function in the SIs involves a highly oscillatory and slowly decaying kernel; the zeroth-order Bessel function of the first kind. The problem is further complicated by the presence of singularities in the Green's functions near the integration path in the complex k_ρ plane.

Two types of singularities can exist, namely poles and branch points [64]. They occur in complex conjugate pairs in the second and forth quadrants of the k_ρ plane. If the

dielectric material is lossless, then the singularities appear on the real axis. The poles are associated with the TM and TE guided waves in the dielectric slabs. While the branch points occur only for vertically unbounded media, i.e., when the top or the bottom layer is a half space.

Many contributions have been made towards the evaluation of these integrals and they fall into two main categories. The first category is the direct numerical integration approach. The integration path can either be the real axis [65]-[66] or a deformed path on the complex plane [67]. If the integration is done on the real axis the singularities of the integrand should be found out and removed via the residue calculus. Locating the poles (surface waves), and the ensuing evaluation of the numerical residue, with reasonable accuracy, require careful numerical treatment especially for complex geometries. The advantage of this method is that it avoids the evaluation of Bessel function with complex arguments, which might cause difficulties in obtaining accurate results.

As for the deformed integration path, it has been the choice of many authors, see for example [4], [67]. The integration path is deformed into the complex plane to avoid all singularities, eliminating the need for locating the pole singularities. Hence, the deformed path of integration has proven to be the most convenient for multilayer media. The choice of the deformation manner of the integration path is not critical, semi-circle and semi-ellipse approximations have been used. The integration over the real axis tail of the path may be computed as the sum of an alternating series of integrals between zeros of the Bessel function. To speed the convergence series acceleration techniques, such as the method of averages [68] is utilized. A detailed review of the various extrapolation methods that can be used for accelerating the Sommerfeld integral tails is given by Michalski in [69].

The second category is the asymptotic approximation of the Sommerfeld integral. This category depends on a physical or mathematical property of the integrand itself, which when exploited can lead to analytical, or easy numerical evaluation of the integral. This would result in an overall reduction in the time and effort of evaluating the integrals. The limitations of these methods depend on the nature of the approximation technique. Some techniques, while very efficient, work only for a specific class of geometries, and can not be extended for more general cases. Other methods suffer from slow convergence rates in the near field region. For some structures, approximation methods depend on the operating frequency, and may not be applied at higher frequencies.

Examples of the asymptotic expansion methods include the plane-wave spectrum method, which has been used in [70] and then later in [71] where the expressions were modified to enhance the convergence for large separation between the source and field points. The approximation was done for single dielectric layer geometries. The limitation of the method is that it can only handle a single layer of dielectric. Other approximations to the Sommerfeld integral were reported by Barkeshli [72], Dunn [73], King [74], and Hoorfar [75], who added a correction term to the expressions derived in [74] to handle electrically thin substrates.

The modal expansion method, used to approximate the SIs in [76], belongs to this category, which is the precursor to the main method used in this research, the complex images method (CIM). The CIM is thus, an example of the asymptotic representation of the Sommerfeld integrals.

1.3.1 The Complex Images Method

The CIM was first developed by Chow *et al.* [77]. The method derives the asymptotic closed form expressions for the Green's functions. It reduces the time required to fill the MoM matrix by almost two orders of magnitude, with reported accuracy of better than 1% error compared to the direct numerical integration. The technique is attractive because of its relative accuracy and capability to handle several layers of dielectrics, and has been successfully used by several research groups [77]-[95]. In fact, of all the asymptotic expansion techniques, the CIM proved to be the most versatile, and is now adopted to most variations of microstrip structures. From versatility point of view, it is second only to the direct numerical integration, and is more efficient numerically.

In the original formulation of the CIM, the quasi-static images and the surface wave poles are extracted from the integrand of the Sommerfeld integral. Their contributions are handled through the residue theorem. Next, the remaining integrand is approximated via a set of few complex exponentials through the generalized pencil of functions (GPOF) method [78]. This approach was termed the one-level approximation, since it involved using the GPOF to approximate the integrand only once.

The one-level approach suffered from the same limitations encountered in the real axis integration of the SIs. Namely, the pole extraction process was an obstacle for complex geometries. The two-level approach proposed by Aksun [79], alleviates the requirement to locate the poles of the integrand. It can also make the choice of the number of complex images, sampling points, and end points of the sampling region robust. It provides an accurate representation of the Green's functions and is much faster compared to the original one-level approximation.

The CIM was initially limited to horizontal currents, and was used to analyze single layer patches and single layer with a superstrate [80]. It was also extended to handle aperture coupled structures [81]-[82], multilayer transmission lines [83], and MMICs [84]. Later came the extension of the method to include vertical currents, as in vertical wire antennas above a dielectric half-space [85], and coax-fed (probe-fed) patches [86].

1.4 Thesis Outline

In this thesis, the application of the CIM to different types of microstrip radiating structures, including vertical metallization, is presented. This analysis technique is capable of handling several types of feeding mechanisms of the microstrip structure, including line feed, probe feed and aperture coupled problems. A modification to the CIM that leads to a better convergence for the overall Green's function is introduced and applied to many structures. A novel treatment of vertical conductors is also presented. The motivation behind this research is to obtain an accurate and efficient numerical analysis tool that can be applied to a wide class of antennas, microwave circuits and EMI/EMC applications.

The problem is formulated using a mixed potential integral equation, which satisfies the boundary conditions on the conductors. The Green's functions for multilayered structures are derived in the spectral domain. These functions satisfy the boundary condition at the interfaces between the dielectric layers. The CIM is then used to obtain the spatial domain version of these Green's functions. For the horizontal conductors, the two-level approach is modified to offer more flexibility in the application of the GPOF approximation. While, for vertical conductors an efficient approach that requires less pre-processing efforts is presented. The MoM solution is then carried out, with rooftop basis

functions representing the currents.

The analysis procedure is applied to several examples of printed microstrip antennas, microwave circuits, and EMI radiation and susceptibility analysis. The calculated radiation patterns, input impedances and gain for the antennas are compared to other commercially available MoM based software. Good agreement is obtained for all the included results.

In Chapter 2, the integral equation formulation for the horizontal and vertical currents, which can be used with line feeding and probe feeding, is presented. This is followed by the presentation of the integral equation formulation for the aperture coupled problem. The CIM is then presented together with the modification of the method to handle vertical conductors. Expressions of the nonsymmetric components of the Green's functions are then derived. Some numerical examples for using the method in evaluating different types of Green's functions are given.

Chapter 3 gives the details for the MoM solution procedure. The impedance matrix elements are given, and their evaluation is discussed. The method for calculating the radiated emissions from PCBs is also presented, along with the far field approximation of the radiation from antennas. The modification of the MoM procedure for structures containing both vertical and horizontal currents and for aperture coupled structures is included.

In Chapter 4, the application of the analysis method to a number of microstrip antenna geometries is presented. The efficiency of the approach suggested here is also pointed out. Finally, aperture coupled structures are analyzed.

In Chapter 5, the analysis method is applied to varieties of microwave circuits. First,

the numerical accuracy and convergence of the analysis technique is illustrated in comparison to an analytical benchmark. Then, the method is used to calculate the scattering parameters for the microwave circuits tested. The method is also applied to the analysis of wide frequency bandwidth interconnect structures.

Chapter 6 presents the application of the numerical analysis to the radiation and susceptibility analysis of PCBs. Examples from digital circuits are used to present the potential of this method in these applications. Finally the conclusion and future work are discussed in Chapter 7. Final comments on the overall efficiency of the method are also made.

CHAPTER 2

Mixed Potential Integral Equation Formulation

2.1 Introduction

This chapter deals with the derivation of the MPIE used to analyze general microstrip structures. These structures consist of a multilayered dielectric medium, sandwiched between two infinite regions of free space, and contain several conducting objects. The derivation of the integral equation is made first for structures carrying three dimensional electric currents, and then for structures that contain an equivalent magnetic current (aperture coupled problems). The utilized Green's functions are derived in the spectral domain, and the CIM is used to obtain their spatial domain equivalent. The formulation and details of the CIM are given, and how the method can be modified to handle vertical conductors and the nonsymmetric components of the Green's functions.

2.2 Formulation for Horizontal and Vertical Currents

A generic type of the structures that we are analyzing is shown in Fig. 2.1. The dielectric layers are infinite in the horizontal direction, with lossless and infinitely thin conductors. The sources inside the dielectric medium are elementary dipole sources that are used to derive the Green's functions. Therefore, these functions can be thought of as the

impulse response for the system. Once the Green's functions are derived, they are used in the integral equation to calculate the fields everywhere due to the source current distributions. $e^{j\omega t}$ time dependence is assumed and suppressed. The structures can be analyzed using the boundary condition of vanishing electric field on the conductors' surfaces [96]:

$$\hat{\mathbf{n}} \times (\mathbf{E}^e + \mathbf{E}^s) = \mathbf{0} \tag{2.1}$$

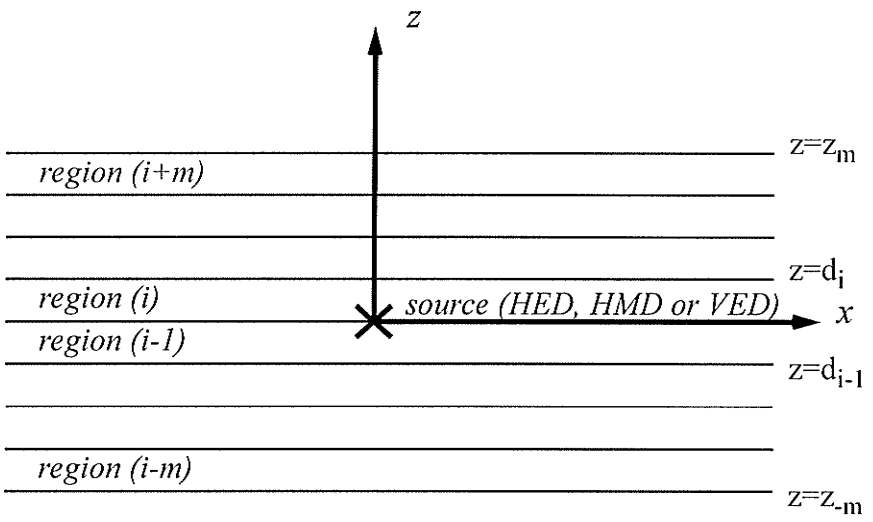

Figure 2.1 Source embedded in a multilayer medium.
(HED = Horizontal Electric Dipole,
HMD = Horizontal Magnetic Dipole,
VED = Vertical Electric Dipole)

where, $\mathbf{E}^e$ is the excitation field, $\mathbf{E}^s$ is the scattered field and $\hat{\mathbf{n}}$ is the unit normal vector to the conducting surfaces. This equation can be considered as a special case of the more

general form $\hat{\mathbf{n}} \times \mathbf{E} = Z_{surf}\hat{\mathbf{n}} \times \mathbf{J}_s$, where Z_{surf} is the surface impedance, which is zero for perfect electric conductors. $\mathbf{J}_s$ is the surface electric current density. The formulation in this chapter is based on equation (2.1).

In terms of the currents on the conductors, the field components can be expressed as:

$$E_x = j\omega \int_s G_A^{xx} \cdot J_x ds + \int_s G_q^x \left(-\frac{1}{j\omega} \nabla \cdot \mathbf{J}\right) ds \tag{2.2}$$

$$E_y = j\omega \int_s G_A^{yy} \cdot J_y ds + \int_s G_q^y \left(-\frac{1}{j\omega} \nabla \cdot \mathbf{J}\right) ds \tag{2.3}$$

$$E_z = j\omega \int_s G_A^{zx} \cdot J_x ds + j\omega \int_s G_A^{zy} \cdot J_y ds + j\omega \int_s G_A^{zz} \cdot J_z ds + \int_s G_q^z \left(-\frac{1}{j\omega} \nabla \cdot \mathbf{J}\right) ds \tag{2.4}$$

where $G_A^{xx,yy,zx,zy,zz}$ and $G_q^{x,y,z}$ are the spatial domain vector and scalar Green's functions, respectively. J_x, J_y, J_z are the components of surface current density $\mathbf{J}$ and s is the surface of the conductors. The choice of the dyadic Green's functions components here is the traditional one [57]:

$$\mathbf{G}_A = (\hat{x} G_A^{xx} + \hat{z} G_A^{zx})\hat{x} + (\hat{y} G_A^{yy} + \hat{z} G_A^{zy})\hat{y} + \hat{z} G_A^{zz} \hat{z} \tag{2.5}$$

The Green's functions for the scalar potential has the property: $G_q^x = G_q^y$, because of the rotational symmetry in the xy plane. These two components are distinct from the G_q^z component. The Green's function can be expressed in the spectral domain as a function of

the radial wave number k_ρ as [89]:

$$\tilde{G}_A^{xx} = \frac{\mu}{2jk_{z_s}} T^{TE} \tag{2.6}$$

$$\tilde{G}_q^{x} = \frac{1}{2j\varepsilon_i k_{z_s}} \left[T^{TE} + \frac{k_{z_f}^2}{k_\rho^2} \left(T^{TE} - \frac{jk_{z_s}^2}{k_{z_f}^2} \frac{\partial T^{TM}}{\partial z_f} \right) \right]. \tag{2.7}$$

where, T^{TE} and T^{TM} are the plane wave transmission coefficients from the plane of the source ($z=z_s$) to the observation plane ($z=z_f$). These transmission coefficients can be derived using equivalent transmission line networks. A complete derivation for all the components of the Green's function is given in Appendix A.

2.3 The Aperture Coupled Problem

To solve the aperture coupling problem, we split the structure of Fig. 2.2 into two regions, equivalent to the upper and lower half-spaces, as shown. Equivalent electric and magnetic currents flow on the microstrip line, microstrip patch and apertures, respectively, of both regions to satisfy the boundary conditions as follows:

• *Boundary condition 1*: The continuity of the tangential electric field components on the aperture is enforced by choosing the magnetic current on the aperture of the lower region, which flows along the x-direction, to be equal and opposite to that on the aperture of the upper region.

• *Boundary condition 2*: The continuity of the tangential magnetic field components on the aperture is satisfied by the following equation:

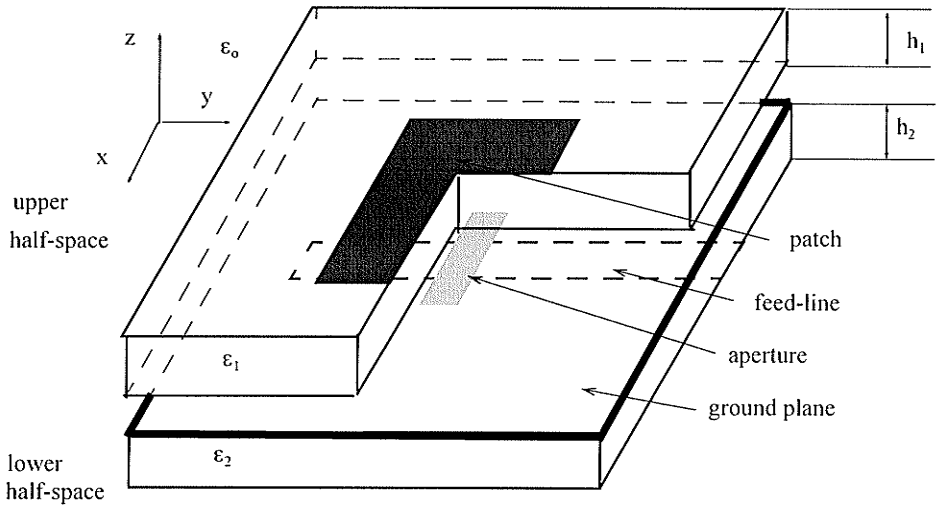

Figure 2.2 Aperture Coupled Patch Antenna.

$$H_x^{(1)}(\mathbf{I}_e^{(1)}) + H_x^{(1)}(I_{mx}^{(1)}) = H_x^{(2)}(I_{ey}^{(2)}) + H_x^{(2)}(I_{mx}^{(2)}) \tag{2.8}$$

where, $\mathbf{I}_e^{(1)}$, $I_{ey}^{(2)}$ are the electric currents flowing on the upper and lower microstrips, respectively, while $I_{mx}^{(1)}$, $I_{mx}^{(2)}$ are the x-directed magnetic currents flowing on the aperture in the upper and lower regions, respectively. $H_x^{(1)}(\mathbf{I}_e^{(1)})$, $H_x^{(2)}(I_{ey}^{(2)})$ are the x-directed magnetic field on the aperture of region 1 and region 2 caused by a y-directed electric current on the microstrip line or an x-directed magnetic current on the aperture, respectively.

The fields in equation (2.8) can be expressed in terms of the mixed potentials of electric and magnetic currents [93], as follows:

$$H_x^{(i)}(I_{mx}^{(i)}) = -j\omega \int_{Aper} G_F^{xx(i)} J_{mx}^{(i)} ds + \frac{1}{j\omega} \int_{Aper} \frac{\partial}{\partial x}\left[G_{qm}^{(i)} \frac{\partial J_{mx}^{(i)}}{\partial x} \right] ds \tag{2.9}$$

$$H_x^{(i)}(\mathbf{I}_e^{(i)}) = H_{x,yy}^{(i)}(\mathbf{I}_e^{(i)}) + H_{x,zy}^{(i)}(\mathbf{I}_e^{(i)}) \tag{2.10}$$

where:

$$H_{x,yy}^{(i)}(\mathbf{I}_e^{(i)}) = \left[\vec{\nabla}_y \int_{s_i} G_A^{xx(i)} \mathbf{J}_e^{(i)} \hat{y} ds \right] \cdot \hat{x} \tag{2.11}$$

$$H_{x,zy}^{(i)}(\mathbf{I}_e^{(i)}) = \left[\vec{\nabla}_y \int_{s_i} G_A^{zx(i)} \mathbf{J}_e^{(i)} \hat{z} ds \right] \cdot \hat{x} \tag{2.12}$$

In equation (2.9), the continuity equation for magnetic current and charge [93] has been used. $G_F^{xx(i)}$ in equation (2.9) is the Green's function for the x-directed electric vector potential due to an x-directed magnetic current in the i^{th} region, while G_{qm} is the scalar potential due to magnetic charge. $G_A^{xx(i)}$ in equation (2.11) is the Green's function for the x-directed magnetic vector potential due to an x-directed electric current in the i^{th} region, where $G_A^{zx(i)}$ in equation (2.12) is the Green's function for the z-directed magnetic vector potential due to an x-directed electric current, with both source and field located inside a microstrip substrate. Detailed derivation of these Green's functions are given in Appendix A. $\mathbf{J}_e^{(i)}$ is the electric current density flowing on the i^{th} region, and $J_{mx}^{(i)}$ is the x-directed magnetic current density flowing on the aperture in the i^{th} region. In these equations, $\hat{x}$, $\hat{y}$ are unit vectors in the x- and y-directions, respectively, and s_i is the surface of the conductor of the i^{th} region.

• *Boundary condition 3*: The vanishing of the tangential electric field on the microstrip lines of the upper and lower regions is satisfied by:

$$E_{x,y}^{(i)}(\mathbf{I}_e^{(i)}) + E_{x,y}^{(i)}(I_{mx}^{(i)}) = -E_y^{in} \tag{2.13}$$

where i=1, 2 correspond to the upper and lower regions, respectively. $E^{(i)}$ and E^{in} are the scattered and impressed electric fields, respectively. The solution then proceeds to segmenting the currents on the patch, aperture, and feed line. These currents are solved for using the MoM as outlined in section 3.3.

2.4 Method of Complex Images

The evaluation of the Green's function in the spatial domain is carried out using the Sommerfeld integral [4]:

$$G_{A,q} = \frac{1}{4\pi}\int_{SIP} dk_\rho k_\rho H_o^{(2)}(k_\rho\rho)\tilde{G}_{A,q}(k_\rho) \tag{2.14}$$

where SIP is the Sommerfeld integration path. Equation (2.14) relates the spatial domain Green's functions $G_{A,q}$ to the spectral domain Green's functions $\tilde{G}_{A,q}$.

The CIM approximation method depends on the Sommerfeld's identity [77]:

$$\frac{e^{-jkr}}{r} = -\frac{j}{2}\int_{SIP} dk_\rho k_\rho H_o^{(2)}(k_\rho\rho)\frac{e^{-jk_z|z|}}{k_z} \tag{2.15}$$

Thus, if the spectral domain Green's function is approximated in terms of exponential functions, the Sommerfeld integral (2.14) can be evaluated analytically in a closed form for

each exponential. This process is more computationally efficient compared to a numerical evaluation of the transform in (2.14).

The original approximation method [77] is outlined here to illustrate our modification. The spectral Green's function is divided into three components as follows:

$$\tilde{G}_A = \tilde{G}_{A_0}(\text{quasi-static}) + \tilde{G}_A^{sw}(\text{surface waves}) + \tilde{G}_A^{ci}(\text{complex images}) \qquad (2.16)$$

where $\tilde{G}_{A_0}, \tilde{G}_A^{sw}$, and $\tilde{G}_A^{ci}$ are defined as:

$$\tilde{G}_{A_0} = \lim_{k_o \to 0} \tilde{G}_A \qquad (2.17)$$

$$\tilde{G}_A^{sw} = \sum_{i=1}^{N_{poles}} k_\rho^{p(i)} H_o^{(2)} Res_A(i) \qquad (2.18)$$

$$\tilde{G}_A^{ci} \cong \sum_{m=1}^{N_{ci}} a_m e^{-b_m k_{z_i}} \qquad (2.19)$$

$\tilde{G}_{A_0}$ is the quasi-static spectral contribution, corresponding to the real images of the source in the multilayer environments. $\tilde{G}_A^{sw}$ is the surface wave contribution, calculated using residue calculus at the location of the poles of the Green's functions. Appendix B includes a detailed discussion on surface waves. N_{poles} is the number of poles and Res (i) is the residue at the i^{th} pole.

In (2.19), $\tilde{G}_A^{ci}$ is derived using the GPOF, N_{ci} is the number of complex images used for the approximation (typically 3-7 in the original formulation), and a_m and b_m are

complex numbers. For the GPOF transformation to be applied, the Green's function must be sampled along a real variable of a complex valued function. Thus the Green's function is sampled along the SIP or another path in the k_ρ plane.

Since all three components (2.17), (2.18) and (2.19) are expressed in exponential format, the Sommerfeld identity can be applied to evaluate the spatial domain Green's functions.

Aksun [79] suggested the two-level approach for the approximation, mainly to render the approximation method robust and more suitable for CAD software. The two-level approach avoids calculating the quasi-static (real images) contribution and the surface waves contribution. Instead the GPOF approximation is directly applied to the spectral domain Green's functions. The direct application of the GPOF would require high sampling rate to capture the rapid variations of the functions specially near the locations of the singularities. Hence, the sampling is done through two stages (two levels). In the first stage the distance between $0 \le k_\rho \le k_{\rho_{max}}$ is sampled with high sampling rate. While in the second stage the remainder of the distance $k_{\rho_{max}} < k_\rho < \infty$ is sampled with a lower sampling rate, hence decreasing the total number of used samples for accurate representations of the Green's functions. The motivation behind this approach is to avoid both the analytic effort of extracting the real images, and the numerical effort calculating the location of the surface wave poles. The pole extraction process cannot be automated for arbitrary layer configuration, and must be repeated for different dielectric constants for the same number of layers involved [89].

In this thesis, we suggest the use of a combination of the two approaches as follows, extract the real images for the associated layer geometry, and proceed to apply the one- or

two-level approach of the GPOF approximation. The extraction of the real images contribution in expression forms depends only on the layer configuration. This extraction, leads to a less stringent requirements on the sampling scheme, and better convergence for the overall Green's function approximation, as will be shown in the results section. This approach suggested here has one more significant advantage. The contribution of the quasi-static images is dominant in the near-field and these components are extracted in an exact analytical manner. Hence we expect that the calculation of the input impedance of the patch antennas to be more accurate.

2.5 Handling Vertical Conductors

The approximation technique just described works well for geometries with only horizontal conductors. Vertical conductors pose a different problem to the approximation technique GPOF. The approximated function needs to be sampled. This sampling requires fixing values for z appearing in the expressions of the Green's function, i.e. the approximation is only valid for a certain source and observation planes. In cases of only horizontal conductors, this poses no problem because the source and observation planes are already fixed. However, in the case of a vertical conductor one needs to integrate along the length of the conductor, i.e. along z. If the technique is used directly, the exponential approximation needs to be performed for every integration point. This results in an extremely inefficient approach to incorporate vertical conductors. Solutions to this problem were suggested by Aksun [84] and Kipp [97]. Different approaches to tackle this problem will be discussed here.

First it should be noted that for single layer geometries, the expressions for the

Green's functions are not dependant on z, hence the GPOF approximation can proceed normally. Next, short vertical conductors $(\text{length} \leq 0.1\lambda)$ can be modeled using only one basis function, hence only three distinct pairs of values for z_f and z_s need to be considered. The approximation can be repeated for each pair of values; the numerical computation overhead is not great in this case.

2.5.1 Handling Long Vertical Conductors

Long vertical conductors can be of any length, span several dielectric layers or be in free space, there is a choice of ways to handle them.

2.5.1.1 Interpolation

This solution is a numerical one, and does not require additional analytical manipulation for the Green's functions. The distance in the z direction is divided into N levels, the GPOF approximation is performed on N(N+1)/2 combinations of z_f and z_s. Other values are found by linear interpolation. Care should be exercised when using the appropriate expression for the Green's function, specially vertical conductors that span more than one layer of dielectric.

While this solution and its results are expensive numerically, the solution serves as a check for other solutions discussed in the following sub-sections.

2.5.1.2 Analytic Solution

The Green function component associated with vertical currents can be written as

follows, (a complete derivation of all the components of the Green's functions is given in Appendix A):

$$\tilde{G}_A^{zz} = \frac{\mu}{2jk_{z_f}}[e^{-jk_{z_f}|z|} + Ae^{jk_{z_f}z} + Be^{-jk_{z_f}z}] \tag{2.20}$$

Equation (2.20) can be written in an expanded form as a summation of four terms. Each of these four terms is an exponential term multiplied by a generalized reflection coefficient. These reflection coefficients are not function of z, hence the GPOF approximation can be applied to each one of these multipliers. The Sommerfeld identity can be used in each term separately. The resulting expression would be a series of exponentials resulting from the GPOF approximation, multiplied by the exponentials used for the expansion of equation (2.20). Similar treatment can be applied to other components of the Green's functions.

This solution requires a specific analytical treatment for each set of dielectric layers that is used. However, the numerical overhead is not excessive (applying the GPOF approximation three extra times). The numerical efficiency is preserved at the added expense of analytic manipulation for each new dielectric profile.

2.5.2 A Novel treatment for the Vertical Conductors

In this section we propose a different approach to this problem, by making the approximation in terms of k_ρ instead of k_z. First, the Sommerfeld identity (2.15) can be written as:

$$\frac{e^{-jkr}}{r} = -j \int_{SIP} dk_\rho k_\rho J_o(k_\rho \rho) \frac{e^{-jk_z|z|}}{k_z} \tag{2.21}$$

Then, through the use of the following identity [98]:

$$\int_0^\infty e^{-\alpha x} J_v(\beta x) x^{v+1} dx = \frac{2\alpha(2\beta)^v \Gamma\left(v + \frac{3}{2}\right)}{\sqrt{\pi}(\alpha^2 + \beta^2)^{v+\frac{3}{2}}} \tag{2.22}$$

Adopting this identity to the integral in (2.21), we set $x = k_\rho$, $\beta = \rho$ and $v = 0$, we have:

$$\int_0^\infty e^{-\alpha k_\rho} J_0(k_\rho \rho) k_\rho dk_\rho = \frac{\alpha}{(\alpha^2 + \rho^2)^{3/2}} \tag{2.23}$$

Next, the GPOF approximation method is applied in the k_ρ plane with the sampling performed on the real axis. Thus $\tilde{G}_{A,q}(k_\rho)$ are expressed by a series of complex exponentials as:

$$\tilde{G}_{A,q}(k_\rho) = \sum_{i=1}^{N_{ci_{A,q}}} a_i e^{-b_i k_\rho} \tag{2.24}$$

This expansion is made possible because k_ρ is a real variable. The main difference so far from the original formulation (2.16) is that the approximation is done in terms of k_ρ instead of k_z. Identity (2.22) can be used in place of the Sommerfeld identity to obtain the Green's function in closed form in the spatial domain:

$$G_{A,q} \cong \sum_{i=1}^{N_{ci_{A,q}}} \frac{a_i b_i}{(b_i^2 + \rho^2)^{3/2}} \tag{2.25}$$

The advantage of this new approximation is that fixing the values of z does not interfere with the application of the GPOF. In the overall procedure the contribution from equation (2.25) replaces that from equation (2.19). The quasi-static contribution and the surface wave contribution are still added as normal. Vertical conductors can be modeled using this approach in an efficient manner. There is no extra numerical or analytic effort needed

The trade-off from using this approach is that the two-level approximation is not applicable any more, since the surface wave poles have to be located and dealt with. However, this is not critical, since most practical substrates have loss associated with them. So the surface wave poles will not lie exactly on the real axis, but rather close to it. This would facilitate locating these poles numerically [64].

2.6 Evaluation of the Nonsymmetric Components of the Green's Functions

A general representation for G_A^{zx}, the z component magnetic vector potential due to an infinitesimal x directed electric dipole is [99]:

$$G_A^{zx}(\rho, z) = \int_{-\infty}^{\infty} \tilde{G}_A^{zx}(k_\rho, z) H_o^{(2)}(k_\rho \rho) k_\rho dk_\rho \tag{2.26}$$

where,

$$\tilde{G}_A^{zx}(k_\rho, z) = \frac{-\mu_s k_x}{2jk_{zs}k_\rho^2}\left(\frac{\mu_f k_{zs}}{\mu_s}T_{TM}^{H,e} + j\frac{\partial T_{TE}^{H,e}}{\partial z_f}\right) \tag{2.27}$$

$T_{TM}^{H,e}$ and $T_{TE}^{H,e}$ are the spectral TM and TE transfer functions between the source and field points. These transfer functions are functions of the radial spectral variable k_ρ, the source and observation or field points positions, as well as the frequency and the physical parameters of the layered medium. The parameters $z_{s,f}$ are distances along the z direction from the lower interface of the embedding medium to the source and field points. The radial spectral vector variable is defined as $\mathbf{k}_\rho = k_x\hat{x} + k_y\hat{y}$ and $k_{zi} = \sqrt{\varepsilon_{ri}k_o^2 - k_\rho^2}$ in medium i.

From equation (2.27), $\tilde{G}_A^{zx}$ is not only a function of k_ρ but also a function of k_x and therefore can not be approximated in terms of the exponentials of $k_{zi} = \sqrt{\varepsilon_{ri}k_o^2 - k_\rho^2}$ by means of the GPOF method. However, $\tilde{G}_A^{zx}/jk_x$ is clearly a function of only k_ρ and can thus be approximated by GPOF method leading to a closed form expression for the integral of G_A^{zx} with respect to x in the spatial domain. The spatial representation of G_A^{zx} can then be found by simple differentiation of the latter integral with respect to x.

The quasi-static $(k_o \to 0)$ asymptote for G_A^{zx} can be derived from equation (2.26) as follows:

$$G_{A_0}^{zx} = \lim_{k_o \to 0} G_A^{zx} = \frac{\partial}{\partial x}\int G_A^{zx} dx\Big|_{k_o \to 0} \qquad (2.28)$$

$$= \frac{-1}{2\pi}\cos\phi \int_0^{\infty} J_1(k_\rho \rho)\frac{\tilde{G}_{A_0}^{zx}}{-jk_x}k_\rho^2 dk_\rho$$

where $\tilde{G}_{A_0}^{zx} = \tilde{G}_A^{zx}\Big|_{k_o \to 0}$ and $\phi = \text{acos}(x/\rho)$ is the field point with respect to the x axis.

The static asymptote $\tilde{G}_{A_0}^{zx}$ can be derived from equation (2.27) by letting $k_o \to 0$ and therefore $k_{z_i} \to -jk_\rho$. This limiting process is also equivalent to the situation where the field point approaches the source. When the source and the field points are in adjacent layers, the final result is:

$$\frac{G_{A_0}^{zx}}{-jk_x} = \frac{-\mu_s}{2k_\rho^2}\exp\{-k_\rho(d - z_s - z_f)\} \qquad (2.29)$$

$$x\left\{\frac{\mu_f}{\mu_s}\left(1 + R_{TM}^{lu}\Big|_{k_o = 0}\right) - \left(1 + R_{TE}^{lu}\Big|_{k_o = 0}\right)\right\}$$

In this equation R_{TE}^{lu} and R_{TM}^{lu} are the static limits of the reflection coefficient at the interface between the source and field layers. In this representation, only the first static term is considered. This approximation is valid for regions near the source point.

If the source and the field points are in the same layer, then

$$\frac{G_{A_0}^{zx}}{-jk_x} = \frac{-\mu_s}{2k_\rho^2}\left[\left(R_{TE}^{u}\Big|_{k_o = 0} + R_{TM}^{u}\Big|_{k_o = 0}\right)\exp\{-k_\rho(2d - z_s - z_f)\}\right. \qquad (2.30)$$

$$\left. -\left(R_{TE}^{l}\Big|_{k_o = 0} + R_{TM}^{l}\Big|_{k_o = 0}\right)\exp\{-k_\rho(z_s + z_f)\}\right]$$

where $R_j^i\big|_{k_o=0}$ (i= l,u;,j= TE,TM) is the static limit of the reflection coefficient at the upper (i=u) or lower (i=l) boundary of the source layer and d is the thickness of the source layer. It is further assumed that $z_s \le z_f$. Only the first three static terms are enough to provide an accurate approximation of the potential function near the source point. When the source and the field point are located in the same layer, the nonsymmetrical component given by equation (2.30) does not contain any term corresponding to the direct interaction between the source and the field point, and only reflections from the top and bottom layers contribute to $\tilde{G}_{A_0}^{zx}$ as is expected. Substituting equations (2.29) and (2.30) in equation (2.28) and using the identity:

$$\int_0^\infty \exp(-au) J_1(u\rho)\,du = \frac{\sqrt{a^2+\rho^2}-a}{\rho\sqrt{a^2+\rho^2}} \tag{2.31}$$

The static asymptote $G_{A_0}^{zx}$ can be obtained in closed form.

In the case where the source point and the field point are located in the same layer of a multilayer medium, the near field approximation can be derived based on the above static asymptote. The result is:

$$\begin{aligned}\frac{G_{A_0}^{zx}}{-jk_x} \approx \frac{\mu_s \cos\phi}{4\pi}\Bigg[&\left(R_{TE}^u\big|_{k_o=0} + R_{TM}^u\big|_{k_o=0}\right) \\ &x\frac{\sqrt{(2d-z_s-z_f)^2+\rho^2}-(2d-z_s-z_f)}{\rho\sqrt{(2d-z_s-z_f)^2+\rho^2}} \\ &-\left(R_{TE}^l\big|_{k_o=0} + R_{TM}^l\big|_{k_o=0}\right) \\ &x\frac{\sqrt{(z_s+z_f)^2+\rho^2}-(z_s+z_f)}{\rho\sqrt{(z_s+z_f)^2+\rho^2}}\Bigg]\end{aligned} \tag{2.32}$$

When the source and the field point are in adjacent layers, one obtains

$$G_{A_0}^{zx} \approx \frac{\mu_s \cos\phi}{4\pi}\left\{\frac{\mu_f}{\mu_s}\left(1 + R_{TM}^{lu}\Big|_{k_o=0}\right) - \left(1 + R_{TE}^{lu}\Big|_{k_o=0}\right)\right\} \qquad (2.33)$$

$$x\frac{\sqrt{(d - z_s + z_f)^2 + \rho^2} - (d - z_s + z_f)}{\rho\sqrt{(2d - z_s + z_f)^2 + \rho^2}}$$

In the special case where the source and the field points are both located on the interface between a dielectric substrate and the air in a typical microstrip line structure, equation (2.33) with $z_f = 0, z_s = d$ can be used to find the asymptote for this configuration:

$$G_{A_0}^{zx} \approx \frac{-\mu_f \cos\phi}{4\pi}\left(\frac{\varepsilon_r - 1}{\varepsilon_r + 1}\right)\frac{1}{\rho} \qquad (2.34)$$

The static asymptote defined by equation (2.28) should not be identified with the static field due to a hypothetical constant current element oriented along the x direction. In fact the static G_A^{zx} due to a constant current element is zero. the static asymptote $G_{A_0}^{zx}$ defined in equation (2.28) provides a very accurate approximation for the dynamic G_A^{zx} in the near field zone.

In the intermediate region $-1 \le \log(k_o r) \le 1$, the following complex images representation is employed:

$$G_{A,ci}^{zx} = \frac{\partial}{\partial x}\sum_{i=1}^{N_{ci}} a_i \frac{\exp(-jkR_i)}{4\pi R_i}$$
$$= \frac{\cos\phi}{4\pi}\sum_{i=1}^{N_{ci}} a_i \frac{\rho}{R_i}\left(\frac{-jk}{R_i} - \frac{1}{R_i^2}\right)\exp(-jkR_i) \qquad (2.35)$$

Beyond $(\log(k_o r) \geq 1)$, surface wave terms are dominant and are given by:

$$G_{A,sw}^{zx} = \cos\phi \sum_{i=1}^{N_{TE}+N_{TM}} B_i H_1^{(2)}(k_{\rho p}\rho) \qquad (2.36)$$

2.7 Numerical Results for the Evaluation of the Green's Function

To illustrate the procedure of the calculation for the Green's functions in the spatial domain, the example in Fig. 2.3 is considered. The structure is a two layer dielectric substrate, with the dielectric constants and heights as illustrated. The perfect conductor ground plane is introduced at the bottom layer. The source and the observation points are located at the interface of the two dielectric layers. The source is assumed to be a horizontal electric dipole (HED). The Green's function is evaluated using the original one-level approach, the two-level approach and the two level approach with the extraction of the quasi-static images. All three evaluation methods are compared.

For the geometry in Fig. 2.3, the parameters in the Green's functions expressions are given by:

$$T_{TE} = \frac{(1 + R_{TE}^{2,1} e^{-j2k_{z2}z})(1 + R_{TE}^{1,0} e^{-jk_{z2}(2d_1 - z)})}{1 - R_{TE}^{1,0} R_{TE}^{2,0} e^{-j2k_{z2}d1}} \tag{2.37}$$

$$T_{TM} = \frac{(1 - R_{TE}^{2,1} e^{-j2k_{z2}z})(1 - R_{TM}^{1,0} e^{-jk_{z2}(2d_1 - z)})}{1 - R_{TM}^{1,0} R_{TM}^{2,0} e^{-j2k_{z2}d1}} , \tag{2.38}$$

and

$$R_{TE,\,TM}^{i+1,\,i} = \frac{r_{TE,\,TM}^{i+1,\,i} + e^{-jk_{z_i}2d_i}}{1 - r_{TE,\,TM}^{i+1,\,i} e^{-jk_{z_i}2d_i}} \tag{2.39}$$

d2=11.1mm	ε_{r2}=1.2
d1=1.5mm	ε_{r1}=2.2

Figure 2.3 A two layer dielectric substrate.

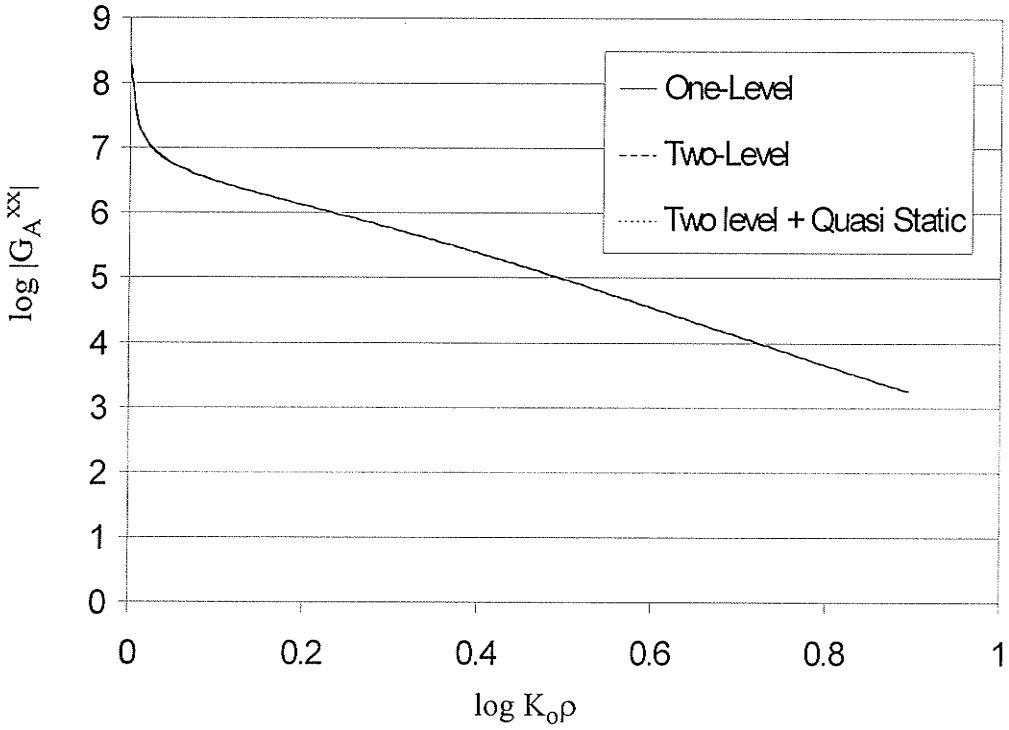

Figure 2.4 The magnitude for the Green's function of the magnetic vector potential.

$$r_{TE}^{i+1,i} = \frac{k_{z_{i+1}} - k_{z_i}}{k_{z_{i+1}} + k_{z_i}} \tag{2.40}$$

$$r_{Tm}^{i+1,i} = \frac{\varepsilon_{i+1} k_{z_{i+1}} - \varepsilon_i k_{z_i}}{\varepsilon_{i+1} k_{z_{i+1}} + \varepsilon_i k_{z_i}} \tag{2.41}$$

In this example we look only at G_A^{xx} for a frequency of 30GHz. Extracting the quasi-static image contribution we have:

$$G_{A_0}^{xx} = \frac{\mu}{4\pi}\left(\frac{e^{-jk_i r}}{r} - \frac{e^{-jk_i r_a}}{r_a}\right) \tag{2.42}$$

where

$$r_a = \sqrt{\rho^2 + (2d_i + z)^2} \tag{2.43}$$

All three approximation methods proceed as explained earlier. For the one-level approach, after the subtraction of the quasi-static and surface wave contribution, the GPOF is applied. The number of complex images used is 4, and 40 sampling points were used.

In the two level approach, in the first step number of complex images is 5, number of samples is 100. In the second step number of complex images is 8, number of samples is 200. Finally for the two-level approach after the subtraction of the complex images in the first step only 4 complex images are needed with 40 sampling points, and in the second step only 6 complex images were used and 120 samples. There is an obvious reduction of the number of samples needed to achieve the same accuracy after subtracting the quasi-static images. Fig. 2.4 shows the magnitude for the Green's function for the vector potential

obtained using the three approaches.

In the next example, a similar geometry is considered in Fig 2.5. This example is used to illustrate the computation of the different components of the Green's functions at different source and field points and different frequencies.

The first set of results is shown in Fig 2.6, in which the magnitude of the magnetic vector potential is plotted versus the normalized electrical distance. The computations are carried out at 6GHz for a HED source. The three curves represents different source and field layers. The layer closest to he ground plane is layer 1 and the layer adjacent to the air half-space is layer 2. i.e, curve 1,2 represents the field at a point on the first layer due to an HED source on the second layer. The corresponding electric scalar potential results are shown in Fig 2.7.

For the same geometry and for a source on layer 1 the observer on layer 2 the results for the vector and scalar Green's functions are evaluated at different frequencies. The results are shown in Fig 2.8 and Fig 2.9. The frequencies are 2, 4, 6GHz, as shown on the graphs.

2.8 Conclusion

In this chapter, the MPIE for in the analysis of general microstrip structures is presented. The Green's functions are derived in the spectral domain and the CIM is used to avert the numerical evaluation of the SIs. The method is modified for the vertical current components and the nonsymmetric components. The numerical efficiency of the original CIM is preserved through each modification. The results presented for the calculation of the Green's function show excellent agreement between the original approach and the

modified approaches. Numerical results also show very good agreement with results based on numerical integration. In the next chapter, the MoM solution to the MPIE is presented. The efficient forms for the Green's functions obtained through the CIM are vital to the rapid evaluation of the MoM matrix elements as shown in the next chapter.

d2=0.78mm	ε_{r2}=2.2
d1=0.78mm	ε_{r1}=9.8

Figure 2.5 A two layer dielectric substrate.

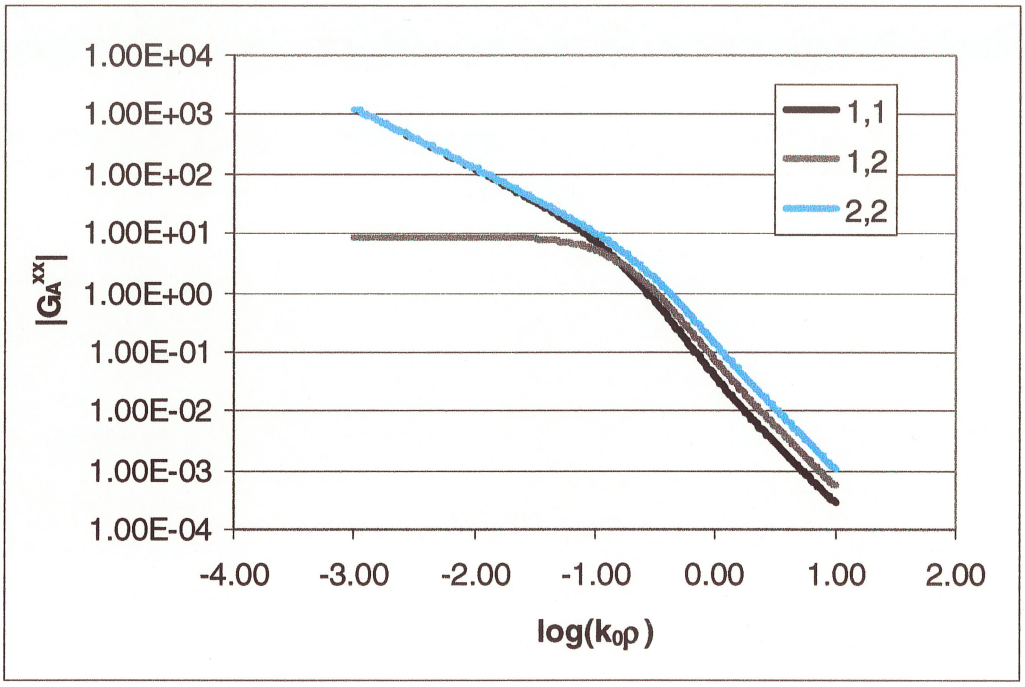

Figure 2.6 The magnitude for the Green's function of the magnetic vector potential.

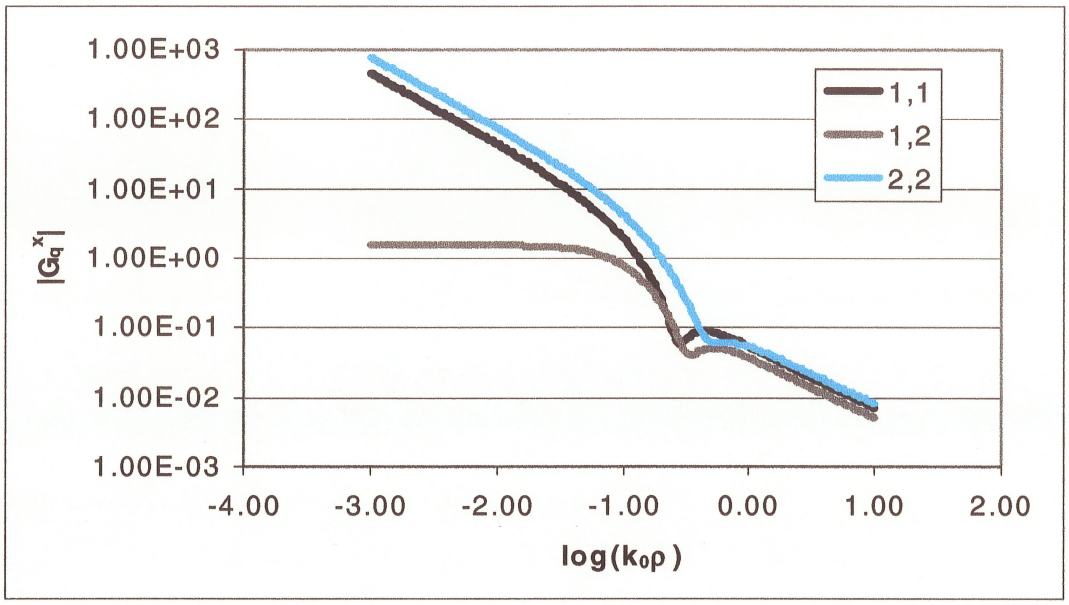

Figure 2.7 The magnitude for the Green's function of the electric scalar potential.

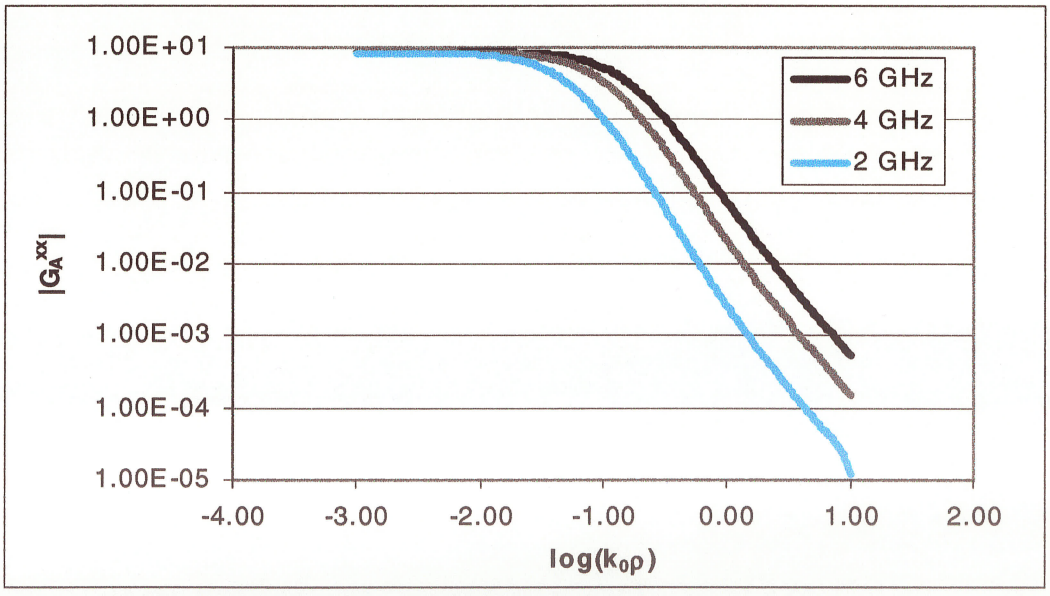

Figure 2.8 The magnitude for the Green's function of the magnetic vector potential.

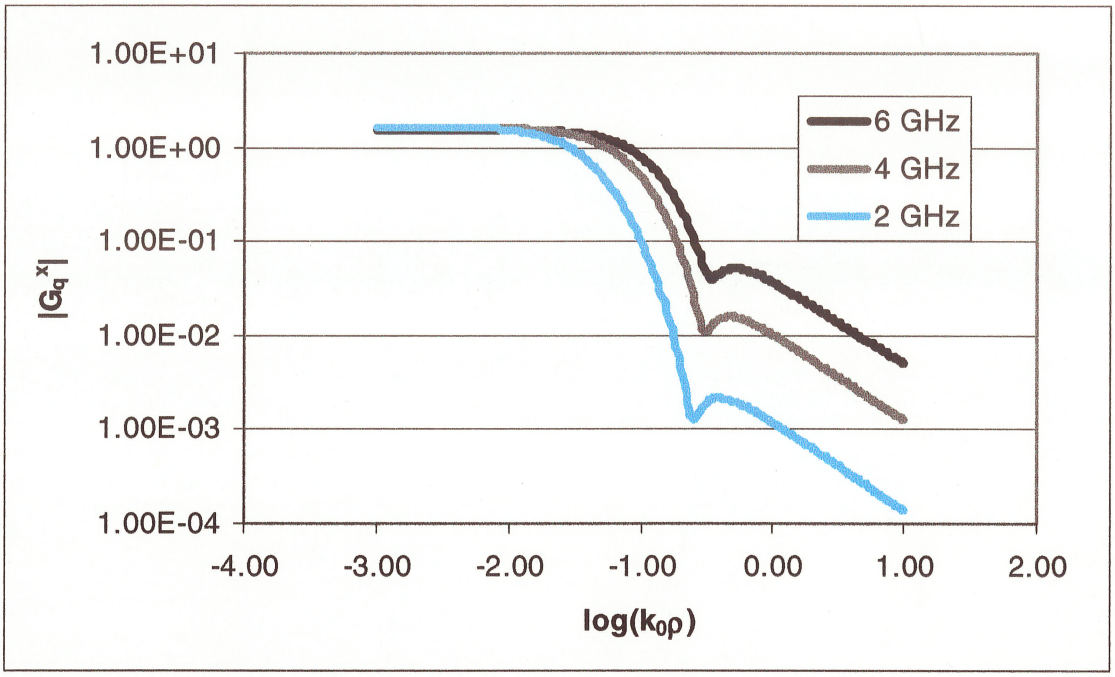

Figure 2.9 The magnitude for the Green's function of the electric scalar potential.

CHAPTER 3

Method of Moments

3.1 Introduction

The well established MoM is used to transform the MPIE into an algebraic matrix equation of the form $A\mathbf{x} = \mathbf{b}$, which can be solved using normal matrix inversion techniques. The MoM can be used to discretize any continuous operator, such as an integral equation. In the MoM procedure, the unknown surface currents are expanded in a set of known basis or expansion functions with unknown coefficients. The integral equation is then tested, in the integral sense, with another set of functions called test functions, resulting in a set of simultaneous equations. The testing functions can be identical to the basis functions, in which case the testing process is called Galerkin's method.

A Galerkin testing procedure is used is this research. Although numerically intensive, it leads to a symmetric matrix, which can further reduce the time required to fill the MoM matrix by one half.

3.2 MoM Solution for Line Feeding

In the case of a microstrip line-fed patch or for microstrip circuits containing only horizontal currents, equations (2.2) and (2.3) only are considered. The MoM matrix

equation, resulting from the current segmentation process, is given by:

$$\begin{bmatrix} V_x^{m'} \\ V_y^{n'} \end{bmatrix} = \begin{bmatrix} [Z_{xx}^{m',m}] & [Z_{xy}^{m',n}] \\ [Z_{yx}^{n',m}] & [Z_{yy}^{n',n}] \end{bmatrix} \begin{bmatrix} I_x^m \\ I_y^n \end{bmatrix} \tag{3.1}$$

where

$$Z_{xx}^{m',m} = \langle J_x^{m'}, G_A^{xx} \otimes J_x^m \rangle - \left(\frac{1}{\omega^2} \langle \frac{\partial J_x^{m'}}{\partial x}, G_q \otimes \frac{\partial J_x^m}{\partial x} \rangle \right) \tag{3.2}$$

$$Z_{yy}^{n',n} = \langle J_y^{n'}, G_A^{yy} \otimes J_y^n \rangle - \left(\frac{1}{\omega^2} \langle \frac{\partial J_y^{n'}}{\partial y}, G_q \otimes \frac{\partial J_y^n}{\partial y} \rangle \right) \tag{3.3}$$

$$Z_{xy}^{m',n} = -\frac{1}{\omega^2} \langle \frac{\partial J_x^{m'}}{\partial x}, G_q \otimes \frac{\partial J_y^n}{\partial y} \rangle \tag{3.4}$$

$$Z_{yx}^{n',m} = -\frac{1}{\omega^2} \langle \frac{\partial J_y^{n'}}{\partial y}, G_q \otimes \frac{\partial J_x^m}{\partial x} \rangle \tag{3.5}$$

and the left hand side elements of the matrix are given by (the source is in the x direction)

$$V_x^{m'} = \langle J_x^{m'}, G_A^{xx} \otimes J_s \rangle + \left(\frac{1}{\omega^2} \langle \frac{\partial J_x^{m'}}{\partial x}, G_q \otimes \frac{\partial J_s}{\partial x} \rangle \right) \tag{3.6}$$

$$V_y^{n'} = \frac{1}{\omega^2} \langle \frac{\partial J_y^{n'}}{\partial y}, G_q \otimes \frac{\partial J_s}{\partial x} \rangle \tag{3.7}$$

J_x^i (i=m,n) are the current density basis functions. V_x and V_y are the excitation currents in the x and y directions respectively. $Z_{xx}^{m',m}$ denotes the mutual impedance between the

m'^{th} testing function and the m^{th} basis function, and $V_x^{m'}$ represents the excitation voltage at the m'^{th} position of the matrix due to the current source, $\otimes$ denotes convolution, and $\langle\ ,\ \rangle$ denotes inner product integral, which is used to define the testing process.

3.2.1 Current Segmentation

The current segmentation process is used to transform the integral equation into the impedance matrix equation (3.1). This section describes the current segmentation and the selection for the basis functions. The choice of the basis functions plays an important rule in determining the rate of convergence of the integrals associated with the evaluation of the matrix elements. An improper choice can lead to non-convergent integrals [100] and erroneous results [101].

The dyadic Green functions associated with the multilayer dielectric structures that are analyzed in this thesis have algebraic singularities of the first order, i.e., $G \sim O(1/|r - r'|)$. They are easier to manipulate numerically than the Green's functions associated with the electric field integral equation which have algebraic singularities of the third order, i.e., $G \sim O(1/|r - r'|^3)$.

Each of the elements of the impedance matrix contains one or two inner products. The inner products that contain differentiation will lead to higher order singularity than those that do not contain those derivatives. Thus it will be sufficient to study only the terms with the derivatives in order to ensure the convergence of all integrals. This inner product is evaluated as follows:

$$\langle \frac{\partial J_x^{m'}}{\partial x}, G_q \otimes \frac{\partial J_x^{m}}{\partial x} \rangle = \int_{D(T)} \int \int_{D(B)} \int \frac{\partial J_x^{m'}}{\partial x} G_q(x-x', y-y') \frac{\partial J_x^{m}}{\partial x} dx dy dx' dy' \tag{3.8}$$

In accordance with the discussion presented in [100] this four fold integral is guaranteed to exist if the basis functions are at least piecewise differentiable. Thus, any choice for the basis functions must satisfy this condition.

Accordingly, the current discretization proceeds as follows, all metallic surfaces, are meshed with rectangular cells. Every two neighboring cells are modeled with a rooftop basis function for the current. The rooftop basis functions are piecewise differentiable, and also have simple mathematical expressions that enable them to be analytically manipulated to simplify the evaluation of the inner product integrals.

$$J_x(x, y) = \sum_{n=1}^{N} \sum_{m=1}^{M-1} I_x^{nm} J_x^{nm}(x, y) \tag{3.9}$$

$$J_y(x, y) = \sum_{n=1}^{N-1} \sum_{m=1}^{M} I_y^{nm} J_y^{nm}(x, y) \tag{3.10}$$

Using a Galerkin MoM procedure, the basis and testing functions (Fig. 3.1) are given by:

$$J_x^{nm}(x, y) = \frac{1}{w}\left[1 - \frac{|x - mh_x|}{h_x}\right] \tag{3.11}$$

$$J_y^{nm}(x, y) = \frac{1}{h_x}\left[1 - \frac{|x - nw|}{w}\right] \tag{3.12}$$

The source contribution to the current density on the microstrip line is accounted for using

the following basis function:

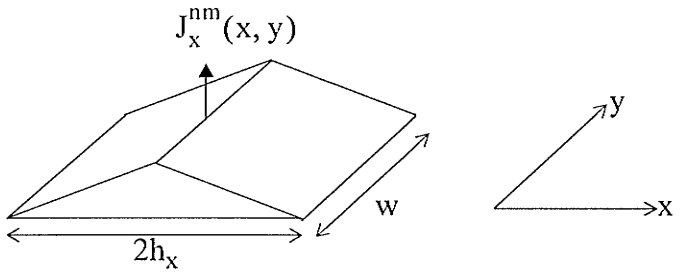

Figure 3.1 The rooftop basis function in the x direction.

$$J_s(x, y) = \begin{cases} \frac{-1}{w} \cdot \left[1 + \frac{x}{h_x}\right] & -h_x \le x \le 0 \\ \frac{1}{w} \cdot \left[1 - \frac{x}{h_x}\right] & 0 \le x \le h_x \end{cases} \tag{3.13}$$

These basis functions are compatible with the rooftop basis function used for representing the current density on the microstrip. However, these functions are piecewise continuous, while the rooftops are piecewise differentiable functions. It should be noted that calculating the divergence of these basis functions includes a singularity, since they are only piecewise continuous. Consequently, the integrals corresponding to the basis function of the source would be divergent unless some other physical constraints are applied to force convergence [100]. The problem of piecewise continuous basis functions for the source representing the source current density is the discontinuity which gives rise to infinite, non-physical charge density, i.e., a singularity in its derivative. If this singularity can be justified physically, it can be removed, and the integral involving these basis functions becomes convergent. The question that arises is about the justification of ignoring the impulse function resulting from the derivative of the piecewise continuous basis function.

To answer this question we recall the principle of conservation of charge at the location of the source, the junction x=0. This junction is the center of the source basis function as evident from (3.13). The current carrying connection (physical source) is connected to the microstrip structure at this point, which implies that the charge density can not be singular and must be finite (the current continuity equation states that there can be no accumulation of charge at any point). Hence, the divergence of the current at the load terminal must be finite. Therefore, it is safe to conclude that the singularities in the derivative of the source basis function are not physical singularities; hence they can be ignored whenever they appear as a result of the divergence of the current.

The entries of the impedance matrix (3.8) include four fold integrals, provided that the closed form Green's functions are used. This integration is numerically extensive even though the integration is over the finite domain of the basis and testing functions. The four fold integration can be reduced to double fold by transferring the convolution integral to the basis functions, and performing this convolution analytically. Our choice of basis functions does permit this analytical evaluation.

There is no separate segmentation process for the charge, which is modeled through the continuity equation, as evident from the integral equation in the used formulation.

3.2.2 Radiation Fields and Radiated Emissions

After solving for the current distribution on the microstrip structure, both the near and far field components of the radiated fields can be calculated by using the corresponding Green's functions. The radiated power can be obtained through the integration of the Poynting vector over a closed surface which could be a rectangular box enclosing the

microstrip structure. In this section, the radiated fields and radiated emissions will be calculated. The electric field components are transformed into the spectral domain where they can be represented as:

$$\tilde{E}_x(k_x, k_y, z) = \tilde{G}_E^{xx}(k_x, k_y, z)\tilde{J}_x(k_x, k_y) + \tilde{G}_E^{xy}(k_x, k_y, z)\tilde{J}_y(k_x, k_y) \quad (3.14)$$

$$\tilde{E}_y(k_x, k_y, z) = \tilde{G}_E^{yx}(k_x, k_y, z)\tilde{J}_x(k_x, k_y) + \tilde{G}_E^{yy}(k_x, k_y, z)\tilde{J}_y(k_x, k_y) \quad (3.15)$$

$$\tilde{E}_z(k_x, k_y, z) = \tilde{G}_E^{zx}(k_x, k_y, z)\tilde{J}_x(k_x, k_y) + \tilde{G}_E^{zy}(k_x, k_y, z)\tilde{J}_y(k_x, k_y) \quad (3.16)$$

Similarly, the magnetic field in the spectral domain can represented as:

$$\tilde{H}_x(k_x, k_y, z) = \tilde{G}_H^{xx}(k_x, k_y, z)\tilde{J}_x(k_x, k_y) + \tilde{G}_H^{xy}(k_x, k_y, z)\tilde{J}_y(k_x, k_y) \quad (3.17)$$

$$\tilde{H}_y(k_x, k_y, z) = \tilde{G}_H^{yx}(k_x, k_y, z)\tilde{J}_x(k_x, k_y) + \tilde{G}_H^{yy}(k_x, k_y, z)\tilde{J}_y(k_x, k_y) \quad (3.18)$$

$$\tilde{H}_z(k_x, k_y, z) = \tilde{G}_H^{zx}(k_x, k_y, z)\tilde{J}_x(k_x, k_y) + \tilde{G}_H^{zy}(k_x, k_y, z)\tilde{J}_y(k_x, k_y) \quad (3.19)$$

The Green's functions for the electric and magnetic fields, for the observers located in free space, $z > 0$, are obtained using the immittance approach and are given by:

$$\tilde{G}_E^{xx} = -\frac{\tilde{Z}_e k_x^2 + \tilde{Z}_h k_y^2}{k_x^2 + k_y^2} e^{-jk_{zo}z} \quad (3.20)$$

$$\tilde{G}_E^{yx} = \tilde{G}_E^{xy} = -\frac{(\tilde{Z}_e - \tilde{Z}_h)k_x k_y}{k_x^2 + k_y^2} e^{-jk_{zo}z} \quad (3.21)$$

$$\tilde{G}_E^{zx} = -\frac{\tilde{Z}_e k_x}{k_{zo}} e^{-jk_{zo}z} \tag{3.22}$$

$$\tilde{G}_E^{yy} = -\frac{\tilde{Z}_e k_y^2 + \tilde{Z}_h k_x^2}{k_x^2 + k_y^2} e^{-jk_{zo}z} \tag{3.23}$$

$$\tilde{G}_E^{zy} = -\frac{\tilde{Z}_e k_y}{k_{zo}} e^{-jk_{zo}z} \tag{3.24}$$

$$\tilde{G}_H^{xx} = -\tilde{G}_H^{yy} = -\frac{(Y_{TE0}\tilde{Z}_h - Y_{TM0}\tilde{Z}_e)k_x k_y}{k_x^2 + k_y^2} e^{-jk_{zo}z} \tag{3.25}$$

$$\tilde{G}_H^{yx} = -\frac{\tilde{Z}_e Y_{TM0} k_x^2 + \tilde{Z}_h Y_{TE0} k_y^2}{k_x^2 + k_y^2} e^{-jk_{zo}z} \tag{3.26}$$

$$\tilde{G}_H^{zx} = -\frac{\tilde{Z}_h k_y}{\omega \mu_o} e^{-jk_{zo}z} \tag{3.27}$$

$$\tilde{G}_H^{xy} = \frac{\tilde{Z}_e Y_{TM0} k_y^2 + \tilde{Z}_h Y_{TE0} k_x^2}{k_x^2 + k_y^2} e^{-jk_{zo}z} \tag{3.28}$$

$$\tilde{G}_H^{zy} = \frac{\tilde{Z}_h k_x}{\omega \mu_o} e^{-jk_{zo}z} \tag{3.29}$$

where

$$Y_{TM0} = \frac{\omega \varepsilon_o}{k_{zo}} \qquad Y_{TM1} = \frac{\omega \varepsilon_o \varepsilon_{r1}}{k_{z1}} \tag{3.30}$$

$$Y_{TE0} = \frac{kz_o}{\omega \mu_o} \qquad Y_{TE1} = \frac{kz_1}{\omega \mu_o} \tag{3.31}$$

$$\tilde{Z}_e = \frac{jk_{z0}k_{z1}\sin(k_{z1}d_1)}{\omega\varepsilon_o[\varepsilon_{r1}k_{z0}\cos(k_{z1}d_1) + jk_{z1}\sin(k_{z1}d_1)]} \tag{3.32}$$

$$\tilde{Z}_h = \frac{j\omega\mu_o\sin(k_{z1}d_1)}{[k_{z1}\cos(k_{z1}d_1) + jk_{z0}\sin(k_{z1}d_1)]} \tag{3.33}$$

Note that Y_{TM0}, Y_{TE0}, Y_{TM1} and Y_{TE1} are wave admittances in free space and in the dielectric medium, respectively. While, $\tilde{Z}_e$ and $\tilde{Z}_h$ may be defined as Green's function for TM and TE waves, respectively.

Once the field components in the spectral domain are obtained, the electric fields in the spatial domain can be evaluated by applying the inverse Fourier transform.

$$E(x, y, z) = \frac{1}{(2\pi)^2}\int_{-\infty}^{\infty}\int_{-\infty}^{\infty} dk_x dk_y \tilde{E}(k_x, k_y, z)e^{-j(k_x x + k_y y + k_z z)} \tag{3.34}$$

The inverse operation is achieved through the use of a two-dimensional Fast Fourier Transform (FFT) algorithm. In (3.34), no far field approximations are used, therefore, this equation can be used for near field as well as far field computations.

The power radiated into the upper half-space is calculated by integrating the z-component of Poynting's vector over the $z = z_o$ plane. This yields

$$P = \frac{1}{2}\mathrm{Re}\int_S\int E \times H^* \cdot dS = \frac{1}{2}\mathrm{Re}\int_S\int (E_x H^*_y - E_y H^*_x)dxdy \tag{3.35}$$

where the asterisk denotes a complex conjugate operation. The computation time can be

saved by transforming the field components in the spatial domain into the spectral domain. The radiated power can be expressed in the spectral domain as:

$$P = \frac{1}{2}\mathrm{Re}\left\{\frac{1}{4\pi^2}\int_{-\infty}^{\infty}\int_{-\infty}^{\infty}(E_x H^*_y - E_y H^*_x)dk_x dk_y\right\} \tag{3.36}$$

Since the value of z is greater than zero, the Green's functions in (3.20)-(3.29) become decaying functions for most of the spectrum, and this leads to the rapid convergence of the double integral in (3.36). Physically, this represents the electromagnetic wave which propagates into the upper half free space transporting away electromagnetic energy.

3.2.2.1 Far Field Radiation Pattern

In this section the far field radiation pattern of the microstrip antenna will be calculated. The method of stationary phase evaluation of the finite Fourier transform integrals asymptotically yields simple and numerically efficient results. The electric field in the upper half space ($z > 0$) can be represented in the form given by equation (3.34). This equation states that the field can be regarded as a superposition of plane waves of the form $\tilde{E}(k_x, k_y, z)e^{-j(k_x x + k_y y + k_z z)}$. Those waves for which k_z is real are propagating and will contribute to the energy flow at infinity, while those waves for which k_z is purely imaginary will be evanescent. It is apparent that the far field radiation arises only from that part of k_x, k_y spectrum for which $k_x^2 + k_y^2 \le k_o^2$.

The method of stationary phase is based on the observation that when r is very large, a function such as $e^{-jk \cdot r}$ oscillates very rapidly between equal positive and negative

values except for certain values of k_x and k_y for which $k \cdot r$ remains stationary. When a slowly varying function of k_x and k_y is multiplied by $e^{-jk \cdot r}$ and integrated over k_x and k_y, the contribution of the integral arises predominantly from those values of k_x and k_y for which the phase remains stationary. For those values of k_x and k_y that make the phase $k \cdot r$ vary rapidly, the contribution of the integral is small because of the cancellation of the positive and negative parts of the integrand. In the limit as r approaches infinity, the leading term in the asymptotic expansion of the integral is given by the contributions arising from the stationary phase points only.

The final expressions for the far field radiation pattern can be written as follows:

$$E_\theta(\theta,\phi) = \tilde{E}_x(k_x, k_y, z_o)\cos\phi + \tilde{E}_y(k_x, k_y, z_o)\sin\phi \tag{3.37}$$

$$E_\phi(\theta,\phi) = [\tilde{E}_x(k_x, k_y, z_o)\sin\phi + \tilde{E}_y(k_x, k_y, z_o)\cos\phi]\cos\theta \tag{3.38}$$

where $\tilde{E}_x$ and $\tilde{E}_y$ are the x and y components of the electric field in the spectral domain, respectively. In (3.37) and (3.38) no integrations are involved, therefore, highly efficient numerical evaluation can be achieved.

3.2.2.2 Input Impedance for a Line Fed Patch

The input impedance at the feed point can be evaluated using the following method. Let the feed line and the patch be modeled by a transmission line terminated with a load impedance. It follows that the microstrip line fed patch antenna can be represented as an equivalent transmission line of characteristic impedance Z_o, terminated with a load

impedance $Z_{load.}$ The transmission line is assumed to support one propagating mode only, and the reference plane is chosen to be far enough from the junction so that all the higher order modes have decayed to insignificant values. With this representation, the current distribution on the feed line may be written as:

$$I(x) = Ae^{-j\beta x} + Be^{j\beta x} \tag{3.39}$$

The unknown coefficients to be determined are A, B and β, where A and B are the coefficients for the incident and the reflected waves, respectively, and β is the propagation constant of the feed line. To determine the unknown coefficients A, B and β, a least square parameter estimation method is used. The constraint that only two exponential terms with identical exponents (propagation constants) except for their sign are used to approximate the current distribution on the feed line is imposed. Once the unknown coefficients are determined, the reflection coefficient at the reference plane can easily be found from the ratio of B to A. Hence, the input impedance can be determined from the reflection coefficient.

3.3 MoM Solution for Probe Feeding and Vertical Conductors

In this section the MoM solution for structures containing all three components (x, y and z) of the current is formulated. Similar to the pervious section, rooftop functions are chosen as the basis functions to represent x, y, and z components of the current density. The sources are modeled as current filaments, therefore, it is suitable to use half-rooftop basis functions at the source terminals, as well as at the sink terminals where the shorting pins or via holes are terminated in the ground plane. At the intersections of vertical and horizontal conductors, half-rooftop and saw-tooth basis functions are employed on the vertical and

horizontal conductors, respectively, whose amplitudes are related to satisfy the conservation of charges.

The boundary conditions for the tangential electric fields are implemented in integral sense through the testing procedure of the MoM, for which the field expressions are multiplied by rooftop testing functions, and are integrated on the conductors. This leads to a matrix equation for the unknown coefficients of the basis functions as:

$$\begin{bmatrix} V_x^{m'n'} \\ V_y^{m'n'} \\ V_z^{l'} \end{bmatrix} = \begin{bmatrix} [Z_{xx}^{m'n',\,mn}] & [Z_{xy}^{m'n',\,mn}] & [Z_{xz}^{m'n',\,l}] \\ [Z_{yx}^{m'n',\,mn}] & [Z_{yy}^{m'n',\,mn}] & [Z_{yz}^{m'n',\,l}] \\ [Z_{zx}^{l',\,mn}] & [Z_{zy}^{l',\,mn}] & [Z_{zz}^{l',\,l}] \end{bmatrix} \begin{bmatrix} I_x^{mn} \\ I_y^{mn} \\ I_z^{l} \end{bmatrix} \tag{3.40}$$

The matrix entries corresponding to horizontal conductors, namely Z_{xx}, Z_{xy}, Z_{yx}, and Z_{yy} are written explicitly and treated in the previous section. The remaining entries, associated with vertical metallization, are given here:

$$Z_{zx}^{l',\,mn} = \langle J_z^{l'},\, G_A^{zx} \otimes J_x^{mn} \rangle - \left(\frac{1}{\omega^2} \langle \frac{\partial J_z^{l'}}{\partial z},\, G_q^{x} \otimes \frac{\partial J_x^{mn}}{\partial x} \rangle \right) \tag{3.41}$$

$$Z_{zy}^{l',\,mn} = \langle J_z^{l'},\, G_A^{zy} \otimes J_y^{mn} \rangle - \left(\frac{1}{\omega^2} \langle \frac{\partial J_z^{l'}}{\partial z},\, G_q^{y} \otimes \frac{\partial J_y^{mn}}{\partial y} \rangle \right) \tag{3.42}$$

$$Z_{zz}^{l',\,l} = \langle J_z^{l'},\, G_A^{zz} \otimes J_z^{l} \rangle - \left(\frac{1}{\omega^2} \langle \frac{\partial J_z^{l'}}{\partial z},\, G_q^{z} \otimes \frac{\partial J_z^{l}}{\partial z} \rangle \right) \tag{3.43}$$

$$Z_{xz}^{m'n',\,l} = -\frac{1}{\omega^2} \langle \frac{\partial J_x^{m'n'}}{\partial x},\, G_q^{z} \otimes \frac{\partial J_z^{l'}}{\partial z} \rangle \tag{3.44}$$

$$Z_{yz}^{m'n',l} = -\frac{1}{\omega^2}\langle \frac{\partial J_y^{m'n'}}{\partial y}, G_q^z \otimes \frac{\partial J_z^{l'}}{\partial z} \rangle \tag{3.45}$$

Evaluating these terms in the impedance matrix is done in a similar fashion to the horizontal currents case. The special treatment for the Green's functions components associated with vertical currents is done in the manner described in the previous chapter.

3.3.1 The Attachment Mode Basis Function

A special basis function is used to ensure the continuity of currents between the coaxial probe and the antenna. Special attachment modes have been employed in the past when studying wires attached to various structures and were shown to greatly increase the accuracy and efficiency of the MoM solution. For thin microstrip structures, a simple, computationally efficient model of the coaxial feed region used in the past assumes that a constant vertical current flows on the coaxial probe and upon reaching the patch this current spreads out horizontally in an assumed manner. The assumed current distribution on the probe and patch is then used to calculate the excitation fields and thus the independent vector of the MoM matrix equation.

This procedure breaks down, however, when the true probe current distribution is not uniform or when the true current distribution on the patch due to the probe differs significantly from the assumed current distribution. The attachment mode employed here is an extension of this idea yet does not restrict the current distribution in the feed region. The currents on the probe are not assumed to be constant but are expanded in a set of

overlapping triangle functions. At the top of the probe a half triangle basis function connects the probe to a small rectangular region where the current is assumed to spread out linearly. The normal x and y directed basis functions on the patch also partially model the current distribution in the feed region. This mode no longer creates the excitation fields but rather is treated as a specialized MoM basis function whose amplitude is included as an unknown in the MoM matrix equation. Mathematically the attachment mode basis function is written as:

$$J(x,y,z) = \hat{x}\frac{I}{2d_y}\mathrm{sgn}(x)\left[1-\frac{|x|}{d_x}\right] + \hat{y}\frac{I}{2d_x}\mathrm{sgn}(y)\left[1-\frac{|y|}{d_y}\right] + \hat{z}\delta(x)\delta(y)\left[1-\frac{2|h-z|}{d_z}\right] \tag{3.46}$$

This basis function is non zero only over a rectangle ($2d_x$ by $2d_y$) on the patch from z=h (the air dielectric interface) to z=h-d_z along the coaxial probe where d_z is one half the length of a normal basis function used on the probe. The current distribution associated with this basis function is depicted in Fig 3.2. A special testing function is also introduced that is employed with the attachment mode that consists of four line test segments on the patch and a short stub along the coax as shown in Fig 3.3.

Several more complex attachment modes have been incorporated and tested in the present model. While the attachment mode of (3.46) does not strictly model the proper singularity of the currents near the coaxial junction, it provides an excellent balance between computational efficiency and the overall accuracy of the calculated impedance data.

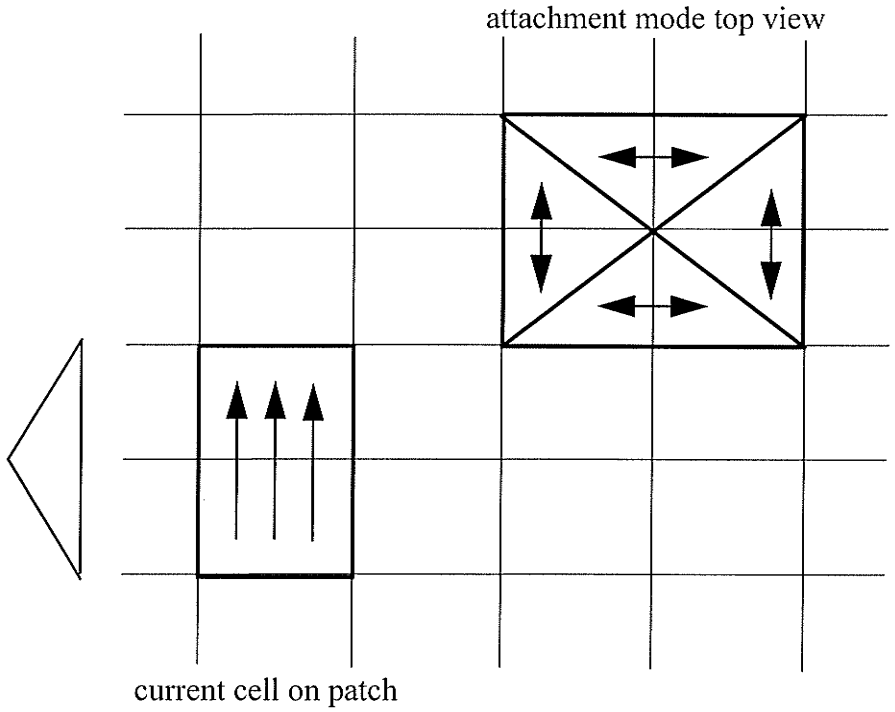

Figure 3.2 Top view of the segmented microstrip patch showing the relative positions of the current cells and the attachment mode.

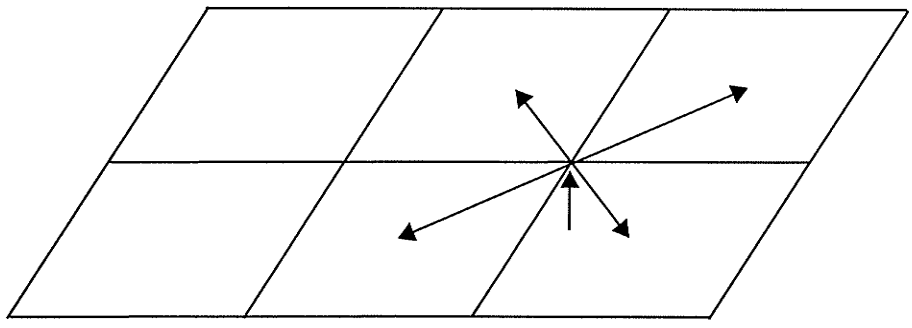

Figure 3.3 Perspective view of the attachment mode testing function.

3.3.2 Calculation of Input Impedance and Coupling Parameters

The input impedance of the antenna is given by U/I(0), where U is the voltage of the frill used to excite the antenna and I(0) is the current at the base of the coaxial probe found via the MoM procedure. When studying antennas with multiple coaxial excitations it is more convenient to work with the port admittance matrix with elements given by:

$$Y_{ij} = \frac{I_j(0)}{U_i} \qquad U_j = 0, j \neq i \tag{3.47}$$

Where U_i is the voltage of the frill at the excited port and $I_j(0)$ is the MoM current at the base of the j^{th} coaxial probe. Once filled, this matrix is inverted to obtain the port impedance matrix that can be used to compute the scattering parameters of the multiport.

3.4 MoM Solution for the Aperture Coupled patch

The electric current density on the patch and on the feed line, and magnetic current density on the aperture are expanded as follows:

$$\mathbf{J}_{e(x,y)}(x,y) = \sum_{n=1}^{N} \sum_{m=1}^{M-1} I_{x,y}^{nm} P_{e(x,y)}^{nm}(x,y) \tag{3.48}$$

and

$$J_{mx}(x) = \sum_{l=1}^{L} K_x^l P_{mx}^l(x) \tag{3.49}$$

where N, M and L are the number of segments on the microstrip and aperture, respectively. P_e, P_m are rooftop basis functions.

The Galerkin moment method [102] is applied to equations (2.8) and (2.13), using the expansion functions of eqs. (3.48) and (3.49) also as weighting functions. This results in the following matrix equation:

$$\begin{bmatrix} \mathbf{0} \\ \mathbf{0} \\ V_{in} \end{bmatrix} = \begin{bmatrix} [Z_{ee}^{(1)}] & [Z_{em}^{(1)}] & [0] \\ [Z_{me}^{(1)}] & [Z_{mm}^{(1)}] + [Z_{mm}^{(2)}] & -[Z_{me}^{(2)}] \\ [0] & [Z_{me}^{(2)}] & [Z_{ee}^{(2)}] \end{bmatrix} \begin{bmatrix} \mathbf{I}_e^{(1)} \\ I_{mx}^{(1)} \\ I_{ey}^{(2)} \end{bmatrix} \tag{3.50}$$

where $Z_{ee}^{(1)}$ and $Z_{ee}^{(2)}$ are the lower and upper microstrip impedance matrices, respectively. These matrices are similar to the ones in section 3.2. $Z_{mm}^{(1)}$and $Z_{mm}^{(2)}$ are the lower and upper magnetic-magnetic aperture impedance matrices, respectively. These represent the dual of the electric-electric impedance matrices in 3.2. $Z_{me}^{(1)}$ and $Z_{me}^{(2)}$ are the matrices for the magnetic voltages on the aperture due to unit electric currents on the microstrip line. $Z_{em}^{(2)}$and $Z_{em}^{(2)}$are the matrices for the electric voltages on the microstrips of the lower and upper subproblems, respectively, due to unit magnetic currents on the aperture.

3.5 Conclusion

This chapter gives the details of the MoM solution to the MPIE. Impedance matrix elements are given for several cases including horizontal currents, vertical and horizontal currents, and for the aperture coupled case. The method used to predict the radiated emission from microstrip circuits is outlined and the expressions to calculate radiated far fields from planar microstrip antennas are derived. In the following chapters numerical

examples will be given for the application of the MoM to various applications. The next chapter deals with the application of the method to multilayer antenna problems.

CHAPTER 4

Application to Multilayer Antennas

4.1 Introduction

In order to check the validity of the analysis technique that is formulated in the previous chapters, extensive numerical tests are performed and compared to the analysis results obtained from commercial CAD software. The examples given in this chapter are selections from these tests. The presented geometries are practical microstrip antennas and their feeding circuits. The results obtained prove the versatility of the method, and its applicability to the design and optimization of microstrip antennas.

4.2 Multilayer Antennas

In this section, tests are carried out to check the validity of the MoM solution for examples of stacked microstrip antennas. The results are compared to those obtained from the CAD software IE3D [103]. The structures tested in this section contain only horizontal metallization.

The first example, shown in Fig. 4.1, involves the analysis of an electomagentically coupled patch. The lower dielectric layer has the feed line, while the patch is located on the upper layer. The simulation is at a frequency of 1.46GHz. The results are shown in Fig. 4.2.

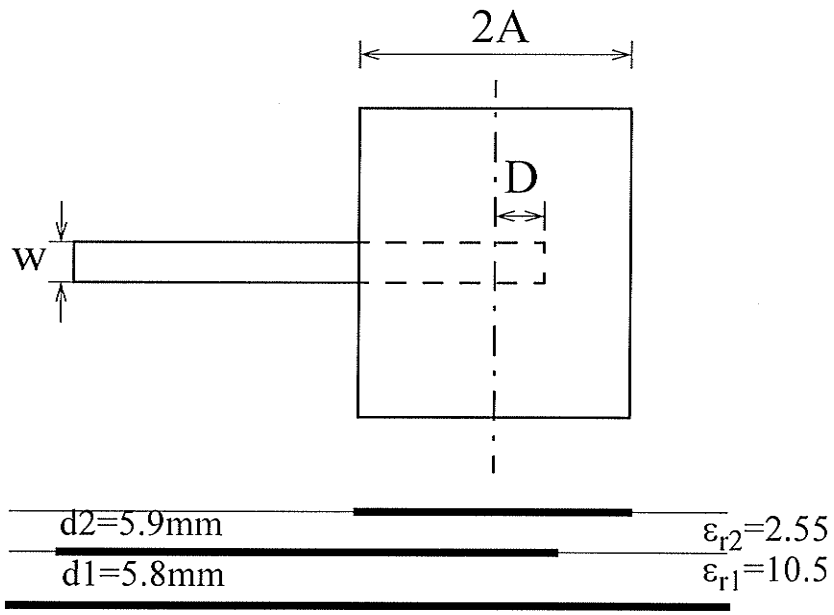

Figure 4.1 Electromagnetically coupled patch, 2A=67.85mm, w=4.53mm.

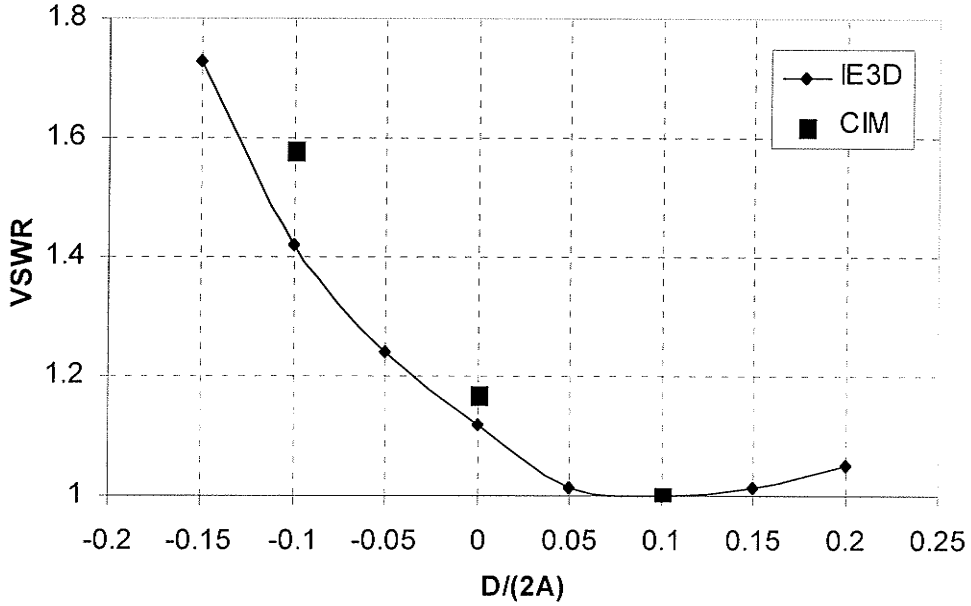

Figure 4.2 VSWR for the electromagnetically coupled patch.

The ratio of D/(2A) is varied, and the voltage standing wave ratio (VSWR) is calculated. The results are in good agreement with those obtained from IE3D. The CIM method is used for calculating the Green's functions. The quasi-static portion is subtracted first, then the two level approach is applied, as explained in Chapter 2.

The structure is not complex, only 80 current cells are used for the segmentation (for D/2A = 0). The filling time for the matrix was the dominant factor, and took 55% of the total running time. This percentage would increase to 73% if we did not subtract the quasi-static images first, which is a 25% time-increase. Hence, utilizing the approach suggested here results in a considerable overall time saving for the solution.

In the second example, a two layer stacked patch is studied, the geometry is shown in Fig. 4.3. The results for the input impedance are shown on the smith chart of Fig. 4.4. The frequency range for the simulation is 1.4-1.8GHz. Close agreement for the results with the IE3D is also obtained. The number of current cells for this example is 152. The time saving achieved by subtracting the quasi static images is less than 10% of the overall solution time. The reason for this is that the time required for the matrix inversion is starting to increase.

4.3 Probe-Fed Microstrip Antennas

In this section, the pervious formulation is applied to probe-fed microstrip antennas and the results again are compared to those obtained from the software IE3D [103]. The structures contain both vertical and horizontal metallization, in a multilayer dielectric environment to demonstrate the various aspects of the application of the CIM, and the ability of the modified CIM to handle vertical conductors. The S-parameters reported are

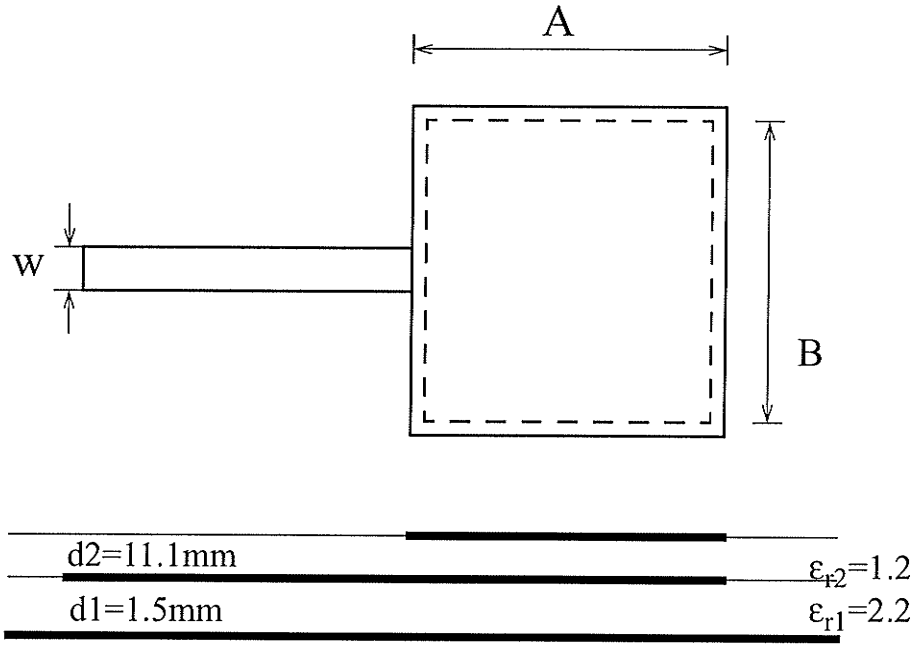

Figure 4.3 Stacked microstrip patch antenna,A=67.85 mm, B=62.56mm, w=4.53mm

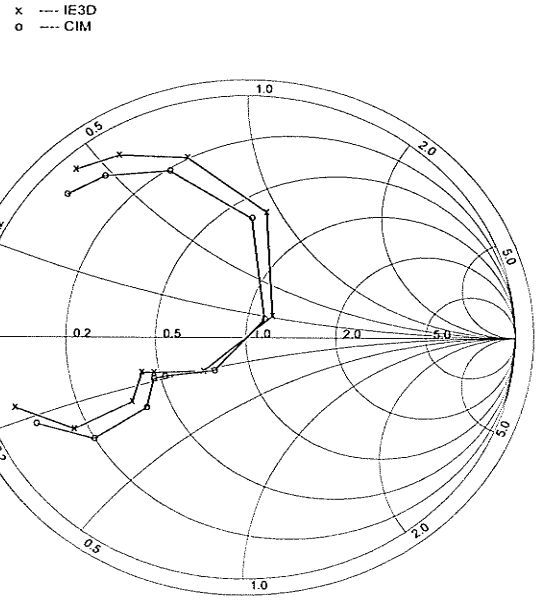

Figure 4.4 Input impedance for the stacked patch antenna.

with respect to a 50ohms reference impedance.

The example, shown in Fig. 4.5, is a two layer stacked microstrip patch antenna. The lower patch is fed via a probe connected to a coaxial cable. The upper patch is slightly larger, and is fed through electromagnetic coupling from the lower patch. Both patches have a square geometry. The details for modeling the probe connection to the patch in the MoM matrix can be found in [86]. The top layer is covered with a third dielectric radome layer. The simulation is carried out for the geometry in the frequency range 1.4-1.8GHz. The results for the magnitude of the input reflection coefficient S_{11} is shown in Fig. 4.6. The input impedance clearly shows the two resonant dips in the S_{11} return loss. The reference plane for these results is at junction of the coaxial probe and the lower patch. The close agreement between the simulation results obtained from the CIM and the CAD software IE3D is evident.

4.4 Aperture Coupled Antenna

To test the validity of the numerical model for aperture coupled problems, the geometry in Fig. 4.7 is analyzed using the technique described in the previous chapter. The configuration used for the substrate thickness and dielectric constants mimics the monolithic phased array applications. The feed substrate could be gallium arsenide for phase shifters and other active circuitry. The Smith chart results for the calculated input impedance are shown in Fig. 4.8. In which the results obtained using the CIM are compared with the results published in [104]. It can be noticed that there is a good agreement with the measurements over the considered frequency band. The frequency values on the smith chart are in MHz.

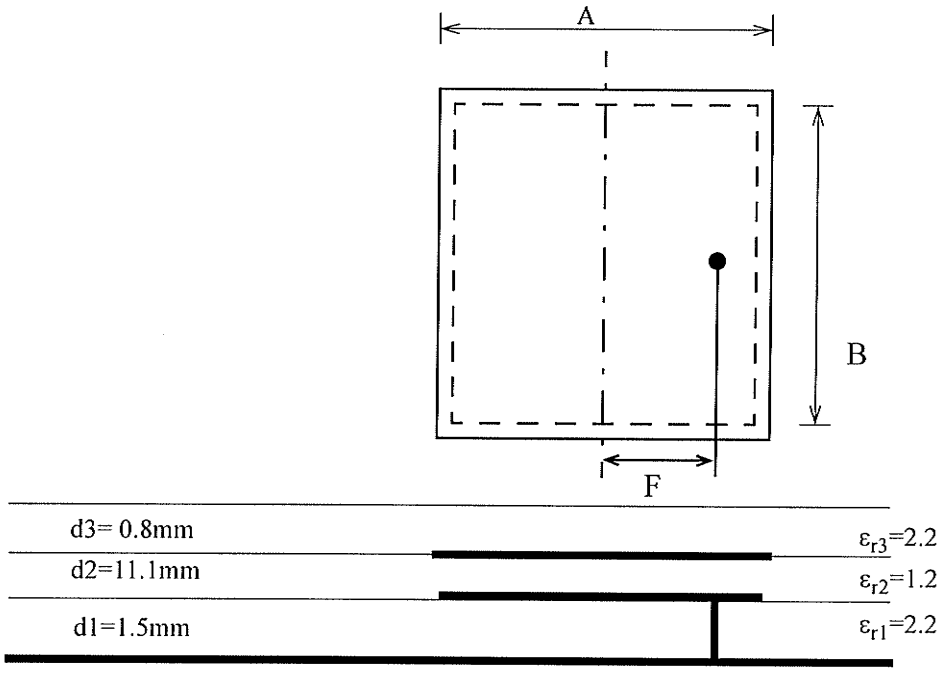

Figure 4.5 Stacked coax-fed microstrip A=67.85mm, B=62.56mm, F=29mm.

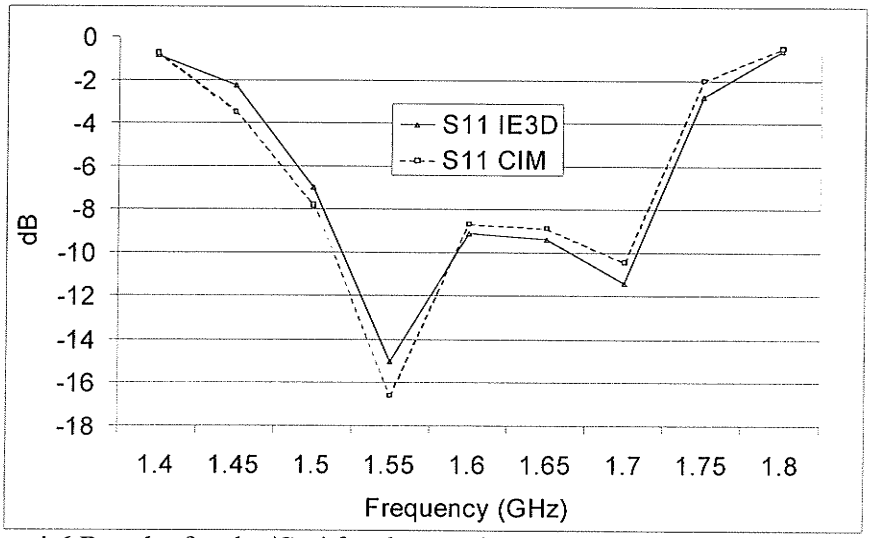

Figure 4.6 Results for the $|S_{11}|$ for the two layer probe fed microstrip antenna.

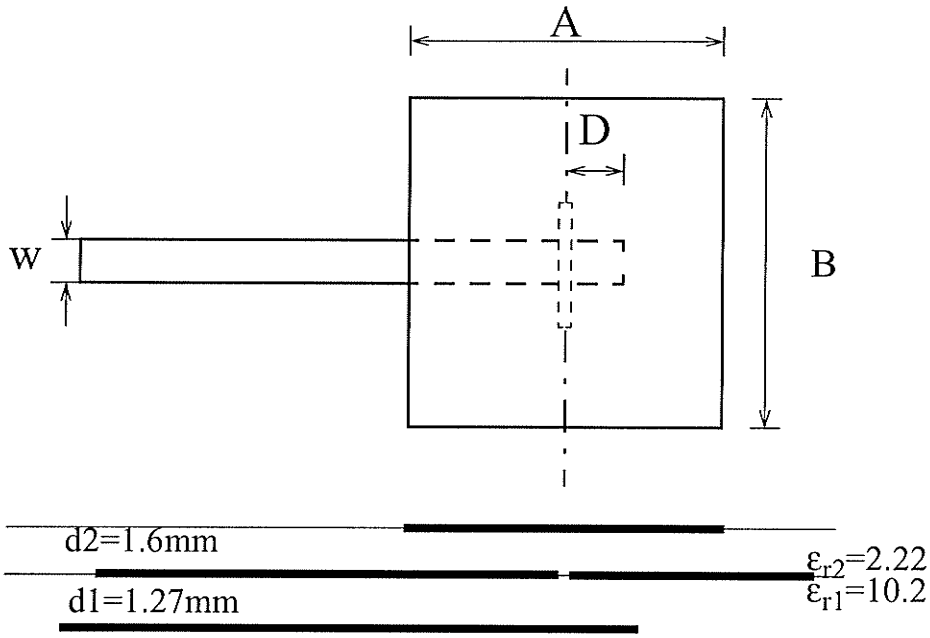

Figure 4.7 Geometry for the aperture coupled antenna, A=3cm, B=4cm, w=1.16mm, D=.12cm, Slot width=.06mm, length=.2cm.

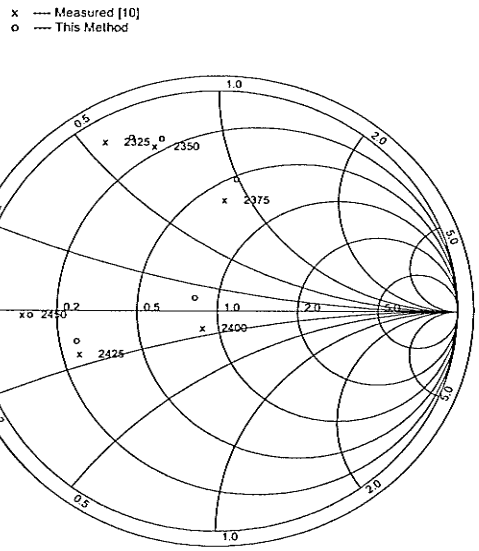

Figure 4.8 Input Impedance for the aperture coupled antenna.

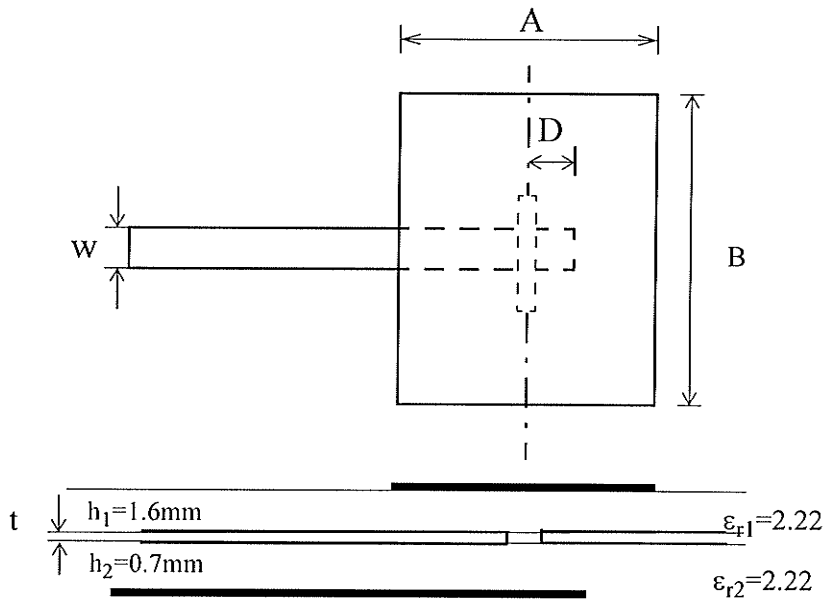

Figure 4.9 Geometry for an aperture coupled microstrip patch. A=3.145cm, B=2.2cm, w=2.47mm, D=1.4cm, Slot width=1mm, length=0.92cm, t is the ground plane thickness.

The second example integrates the usage of the aperture coupled formulation with the vertical currents formulation. The geometry shown in Fig. 4.9 is an aperture coupled microstrip patch through a thick ground plane. The structure was first suggested by Haddad and Pozar [105] as a solution to the heat dissipation problem associated with integrated microwave circuits. The thick ground plane can provide the extra heat sink needed for the active components. The coupling between the upper and lower layers decreases with the increase in the ground plane thickness.

The analysis in [105] was performed using the reciprocity method and modeling the volume created via the ground plane as a cavity. Here, the analysis is carried out via assuming two distinct unknown magnetic currents on the upper and lower faces on the thick ground plane, in addition electric currents on the vertical walls of the ground plane are considered. Only z directed currents on the walls are assumed. The results predicted here should be more accurate than those reported earlier, since no assumption are made on the nature of the field inside the cavity formed in the slot volume.

The results for the variation of the input resistance versus the normalized ground plane thickness are shown in Fig. 4.10. The first point on the graph corresponds to the original zero thickness ground plane. The results show the decrease in the resonant input resistance with the thickness of the ground plane. Again close agreement between the IE3D results for the resonant input resistance and the CIM results is demonstrated.

The variation of the gain versus the ground plane thickness simulation results is shown in Fig. 4.11. This simulation results show the trade-off between the required ground plane thickness for heat dissipation, and the required gain of the element. This curve can be a useful design aid. In this graph, the ground plane thickness is normalized with respect to

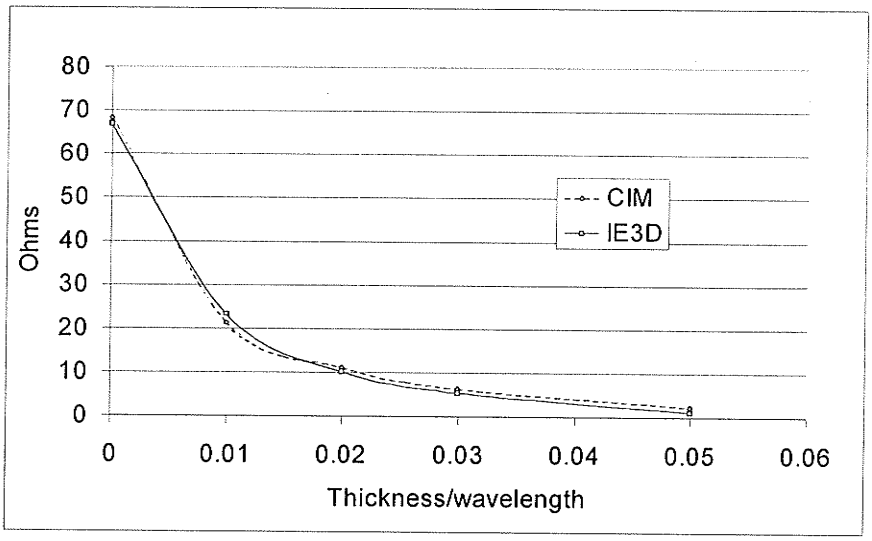

Figure 4.10 Calculated resonant input resistance versus normalized ground plane thickness.

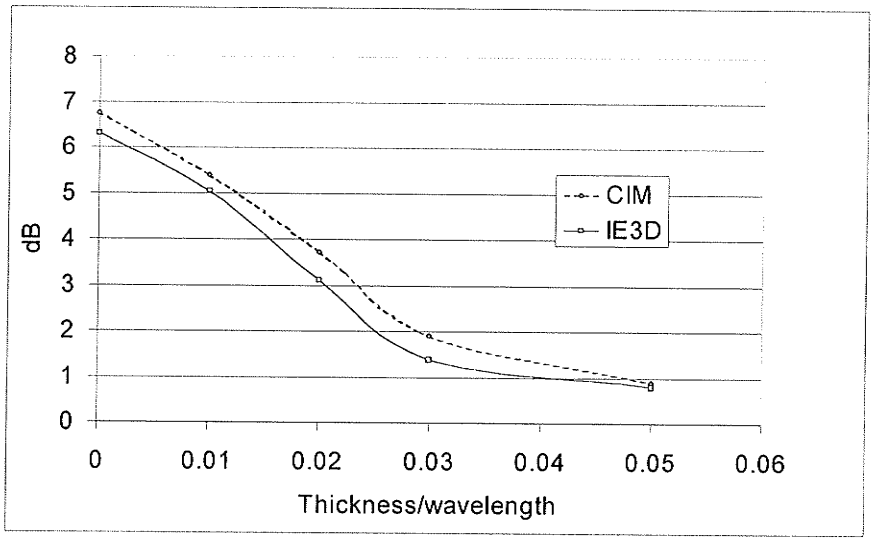

Figure 4.11 Calculated Gain versus normalized ground plane thickness.

the wavelength. The frequency at which the simulation is carried out is 3GHz. It is evident that as the ground plane thickness approaches 2% of the wave length (2mm) the element loses its efficiency as a radiator. Acceptable agreement between the two simulation results is obtained.

4.5 Microstrip Antenna Arrays

The MoM code is applied to an example of microstrip array in this section. The example is a corporate fed array of linearly polarized microstrip patch antennas. The corporate fed arrays typically suffer from low efficiency due to the losses in the corporate feed network. Because of their low profile and low cost of manufacturing on a single layer dielectric, corporate fed microstrip arrays are candidates for use as LMCS subscriber terminals [106].

The most common method of realizing these arrays is to feed the patches along their radiating edges. An alternative, simpler and more efficient feed network design [107] consists of patch elements fed along their non-radiating edges, as shown in Fig. 4.12. The array is built on a substrate with height h=0.794mm and ε_r=2.55. The array is built utilizing a 2 X 2 subarray element that is used as a basic building block. The block is repeated four times to create the 16 element planar array. All the elements are placed in the same direction and have the same excitation. The array is designed to operate at a center frequency of 12GHz. The elements are spaced 0.75λ, and the feed lines are 50ohm lines with 2.1mm width each. Each thick part of the feed network is a quarter wavelength matching section with 35.35ohms and 3.8mm width. The details of the design can be found in [108]. The array is simulated using both IE3D and the proposed MoM code. The results of the

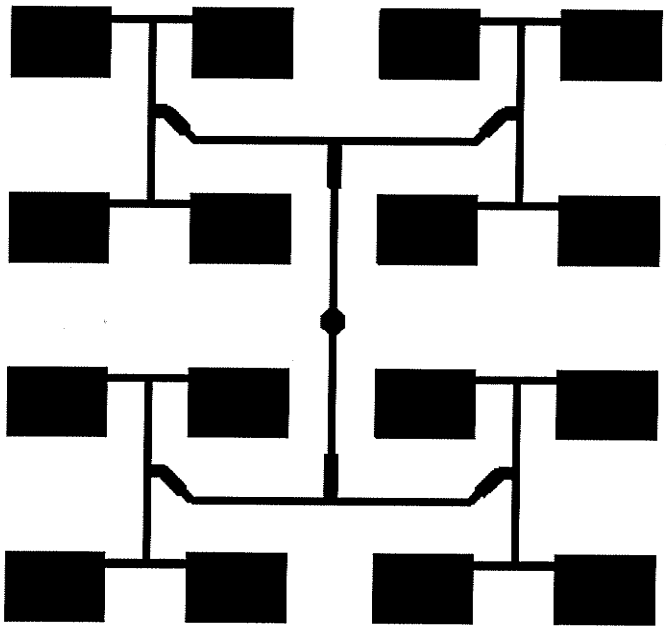

Figure 4.12 Microstrip array geometry.

simulations are shown in Fig. 4.13 and Fig. 4.14.

While simulating the array using the CIM method, and in order to get better results, the metals had to be discretized into fine segments. The feed network needed to be segmented into 4 current cells for the width of the transmission line. Using uniform segmentation this translates into a cell size of 0.5 X 0.5mm. The impedance matrix size is excessively large (more than 10 thousand current elements) and the simulation time is in the order of 14 hours on a Pentium III 400MHz processor workstation for 50 frequency steps. The fine segmentation is needed to obtain the precise results. On the other hand, the time for simulating the array on IE3D for the same number of frequency steps is in the order of 4 hours on the same workstation. This is because the commercial CAD software is taking advantage of variable size mesh and interpolation for frequency steps. Besides, the geometry contains one dielectric layer only which is the simplest case for the Green's functions computations.

4.6 Conclusion

The examples discussed in this chapter are for microstrip antenna elements and arrays. The numerical tests performed compare the accuracy of the method versus commercial electromagnetic design software packages. As expected and has been proven through running these tests, there is a trade-off between efficiency and accuracy. The developed code has a simple segmentation scheme, versus the advanced capabilities of the commercial package. In all cases the segmentation used is uniform and preserves the 10 segments/wavelength guideline that is the norm for traditional MoM codes. If simple segmentation is used, the solutions are not precise, as evident from the parasitically coupled

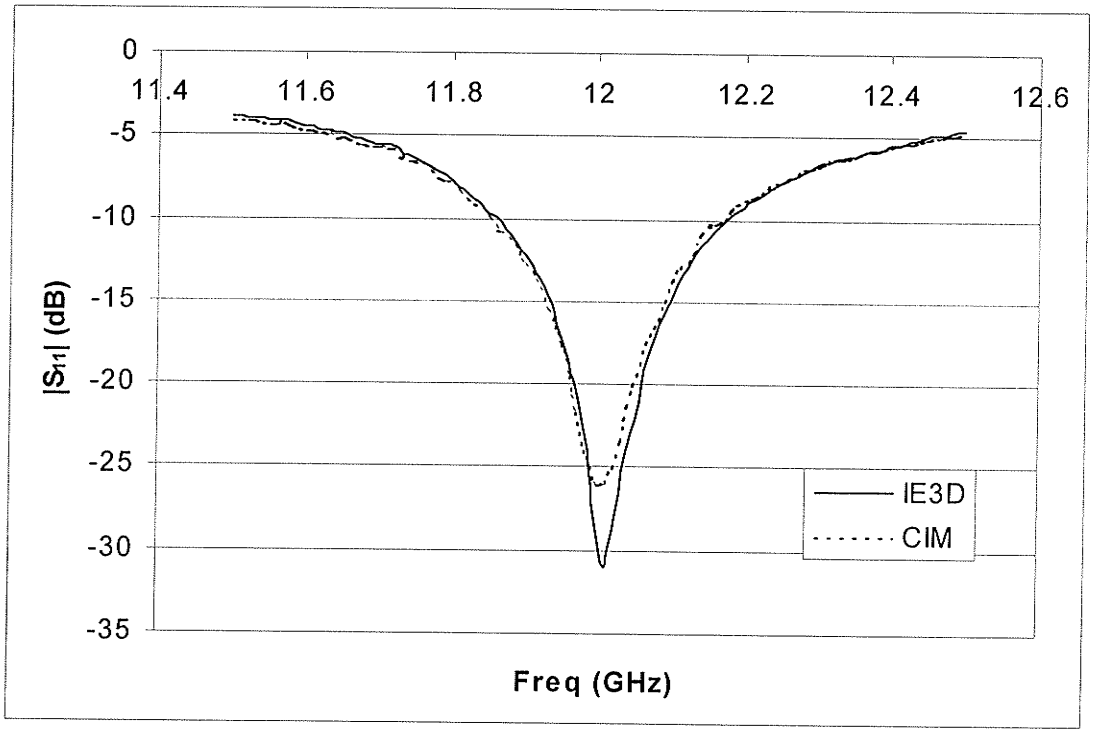

Figure 4.13 Simulated $|S_{11}|$ versus frequency.

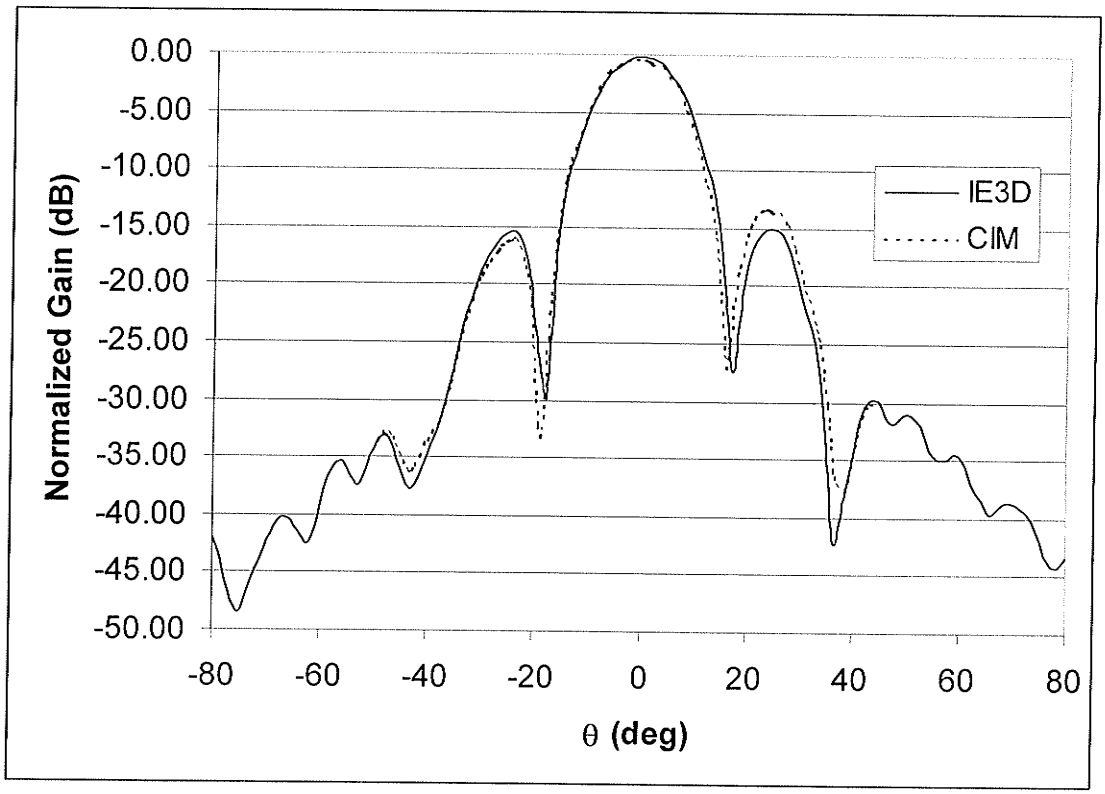

Figure 4.14 Variation of the normalized gain with the azimuthal angle.

patch example. In that particular example the number of current elements used is similar to the number of current segments used by the commercial code. The efficiency of the CIM code is discussed, as explained by the results of the example. On the other hand for more complex geometries, such as the thick ground plane aperture coupled patch or the microstrip array, much more current elements are used by the CIM code, the result is a longer simulation time, but the accuracy is improved. The solution for this trade off would be to use the advanced segmentation methods used by the commercial software, hence ending up with a similar size impedance matrix while preserving the efficiency of the CIM method.

CHAPTER 5

Application to Microwave Circuits

5.1 Introduction

Recent advances in monolithic microwave integrated circuits (MMIC's) and ever-increasing speed of digital circuits have prompted the need for a rigorous and efficient electromagnetic (EM) modeling technique. Therefore, there have been a flurry of activities in the area of computational electromagnetics to develop computationally efficient and accurate numerical techniques for modeling and simulating the electrical performances of such circuits.

Conventional microwave CAD analysis packages, such as Libra, rely on closed form expressions that are driven using conformal mapping techniques and assuming a quasi-TEM behavior for the microstrip elements. These packages further assume that individual discontinuities and lines do not interact. Both assumptions become invalid as the frequency increases and the structures become electrically large ($1 \ll \frac{l}{\lambda}$). At these frequencies, distributed effects dominate the performance and the accuracy of the conventional analysis method falls sharply.

On the other hand, planar electromagnetic simulators can look at the whole picture,

rather than breaking the circuit down into building blocks. This rigorous analysis involves solving Maxwell's equations for two and three-dimensional circuits. Two-dimensional field simulators are used to calculate the modal characteristics and electromagnetic fields for a cross section of transmission lines embedded between layers of dielectrics. The frequency dependant modal characteristics are generated and processed for impedances, voltages, currents, powers, propagation velocities and effective dielectric constants. The three dimensional simulators can calculate the field pattern surrounding a general metal-dielectric structure.

In this chapter, we discuss the application of the MPIE to the numerical analysis of various examples of microwave circuits. The aim of this work is to demonstrate the versatility and accuracy of the analysis method presented in this thesis. In addition, since no restriction is made in the derivation to have an infinite ground plane, the capability of the method to analyze structures with finite ground plane is demonstrated.

5.2 Accuracy of the Analysis Method

Most of the results presented in this thesis are compared to published or computed results from commercial CAD software packages. The accuracy criterion used in judging the results is how good is the agreement between the two sets of data points. In this section, quantitative definition for the accuracy is used. The aim is to evaluate the accuracy of the analysis method against exact solutions and other well-established bench marks.

5.2.1 Stripline Analysis

A lossless stripline with zero thickness has an exact theoretical solution and is ideal

for use as a benchmark for evaluation of the accuracy of electromagnetic numerical analysis methods. The standard stripline that is used for this analysis has been published in [109]. To within the indicated tolerances, this line is precisely 50ohm line and its length is exactly 90 degrees at 15GHz. The ground plane spacing allows single mode propagation up to about 100GHz. The fundamental idea of the standard stripline is that the correct answer is known exactly, thus, we can easily calculate the error in its analysis using numerical techniques. For this particular stripline, by placing two measurement points at either ends of the line, the measured value of S_{11} should be zero and the value for the phase angle of S_{21} should be -90 degrees.

Note that percent error criteria (calculated - correct/correct) of S_{11} is not useful, since its correct value is zero and division by zero is undefined. Instead the following error percentage criteria will be used:

$$E = 100\left(|S_{11}| + \frac{|90 + \angle S_{12}|}{90}\right) \tag{5.1}$$

In the analysis of striplines, in any subsectional basis functions based method, the number of cells into which the width of the line is divided is of primary importance for analysis accuracy. Accordingly, the change of percentage error with the number of cells is studied. The specific analysis information are:

- Frequency: 15GHz.
- Ground plane spacing: B = 1.0mm, exactly.
- Substrate dielectric constant: 1.0, exactly.
- Line width: W = 1.4423896.
- Line length: L = 4.99654097, exactly a quarter wavelength.

• Conductor and dielectric loss: lossless.

Results are shown in Table 5.1. The discretization parameter is cells per line width, which ranges from 1 to 16 cells per line width. The line is divided into 16 cells along its length for all cases. This is why the S_{21} phase is nearly constant. In the table, The first column, labeled "N", is the discretization parameter. The next two columns are for the magnitude of S_{11} and the phase of S_{21}. At 15GHz, the correct value of S_{11} magnitude is zero and the correct value of the phase of S_{21} is -90 degrees. The last column is the error E as defined in equation (5.1).

Generally, an error in the 10% range is unacceptable for most engineering applications. A range around 1% error may be the most commonly required level, yielding a high probability of success on first fabrication. In a few rare cases, 0.1% error may be desired.

One important shortcoming of this accuracy test is that it does not test dispersion. Lossless stripline operated in the fundamental TEM mode, has no dispersion. On the other hand, being dispersionless, there is no uncertainty as to the characteristic impedance. Even with these limitations, this stripline comparison allows the precise quantitative investigation of the accuracy of our proposed numerical analysis method.

Table 5.1: Error variation with the number of segments.

N	$\|S_{11}\|$	Phase (S_{12})	Error%
1	0.035	-89.999	3.53
2	0.019	-89.999	1.96
4	0.0102	-89.999	1.03
8	0.0052	-90.0	0.52
16	0.00138	-90.0	0.14

5.3 Numerical Examples

The examples analyzed in this section are microwave circuits and building blocks for microwave and MMIC circuits. The size of the circuits analyzed is of the order of the operating wavelength, where the numerical technique is most efficient.

5.3.1 Quadrature Hybrid Circuit

The first example analyzed is for an H-hybrid circuit shown in Figure 5.1. This hybrid is 3 dB directional coupler with a 90 degrees phase shift difference in the outputs of the through and coupled arms. This type of hybrid is also known as branch-line hybrid. The basic operation of the coupler is as follows, with all the ports matched, power entering port 1 is evenly divided between ports 2 and 3 with a 90 degrees phase shift between these outputs. No power is coupled to port 4, hence it is called the isolated port. Because of the symmetry of the coupler, any port can be used as input port, the isolated port will always be in the same side as the input port.

The specific geometry that is used to run the simulation has a center frequency of 4.7GHz. The dimensions shown on the figure are calculated at this center frequency. The length of the four branches of the coupler is one full wavelength, this particular length was chosen to ensure accurate calculation of the S-parameters and to decrease any effects for higher order modes launched at the feeding ports. This length is not critical to the operation of the coupler provided that the feeding ports are sufficiently removed from the coupling arms. Experimentations with the geometry suggest that the minimum length for these feeding ports has to exceed half wavelength, and the near ideal operation can be achieved as the length approaches one wavelength. As the length exceeds one wavelength the

operation of the coupler is not affected, only the numerical calculations are increased.

The coupler is implemented as a microstrip circuit. The relative dielectric constant for the substrate is 2.1 and its height is 1.6mm. The discretization is carried out such that the length of the microstrip line has 16 divisions per wavelength and the width has 4 divisions. The width of the lines is 5.1mm, calculated to have 50ohms impedance. The results are shown in Figure 5.2. The calculated S-parameters are consistent with the anticipated basic operation for the coupler. This particular coupler has a theoretical frequency bandwidth of 10-20%. From the results, the bandwidth of the operation of the coupler in this particular example is estimated to be 12%. The results for the example confirm the accuracy of the numerical analysis and the extraction of the S-parameters for a matched port termination.

5.3.2 T-Junction

Another example for a basic microwave circuit is shown in Figure 5.3. This is a microstrip T-junction. The T-junction is the most basic form for a microwave power divider/combiner. The incident power on port 1 is divided between ports 2 and 4 based on the impedance of each arm. If the two arms have equal impedance, the power is split equally between the two ports. The reflection coefficient at port 1 can be made zero by making the impedance of the arm attached to port 1 equal to the parallel combination of the impedances of the arms for ports 2 and 3. This kind of power division is not symmetric, i.e. port 2 can not be used to divide the power between ports 1 and 3, otherwise the reflection coefficient would not be equal to zero.

The T-junction in Figure 5.3 is implemented as a microstrip circuit. The dimensions

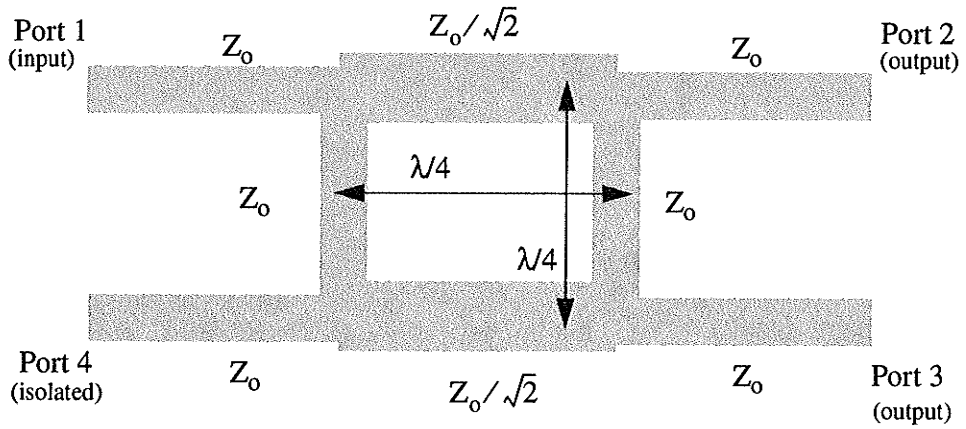

Figure 5.1 Geometry of a directional coupler.

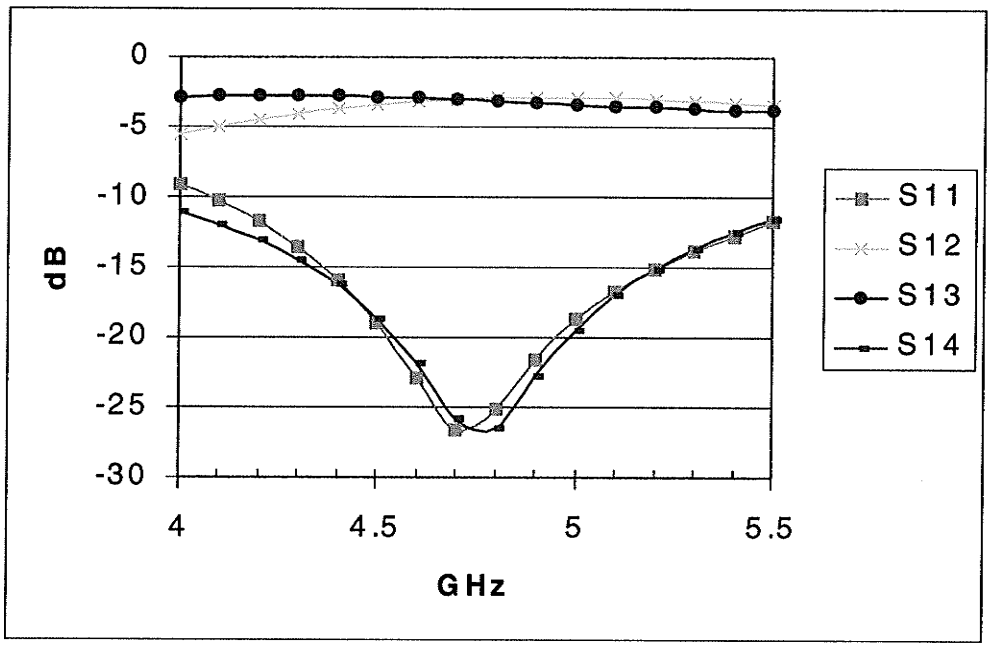

Figure 5.2 S- parameters for the branch-line directional coupler.

are shown in the figure, the width of the lines are all set to be 0.5cm. The relative dielectric constant of the substrate is 9.8, height is 3mm. The ground plane on which the substrate is mounted is finite. The size of the ground plane is 6X4cm. The dielectric substrate is still considered infinite in the lateral dimensions.

The frequency of the simulation starts at 300MHz, and the results are shown in Figure 5.4. The behavior of the S-parameters is as expected, the reflection coefficient at the input port (S_{11}) is not zero, since the impedance of the arms at ports 2 and 3 is not balanced, as explained earlier. The power is divided equally between the two ports ($S_{12} = S_{13}$).

The example confirms the accuracy of the numerical technique for finite ground plane structures and for thin dielectric substrates. The dielectric height used is considered thin at the frequency of the simulation.

5.3.3 Two Layer Microstrip Circuit

The next example analyzed is a two layer transmission line circuit, shown in Figure 5.5. Two microstrip lines run parallel to each other. One of them descends to the lower layer through a vertical connection. This geometry, although simple, can not be analyzed using most microwave circuits analysis packages (such as Agilent's Libra), because of the presence of the two layers of dielectric and the discontinuity in the transmission line. Only a full-wave analysis methods are applicable.

The parameters for the geometry are shown in on the figure, an infinite ground plane is assumed. All the ports have open circuit terminations. The vertical connection between the two segments of the transmission line is modeled as thin vertical conductor strip, with the same thickness as the transmission line itself. This connection does not

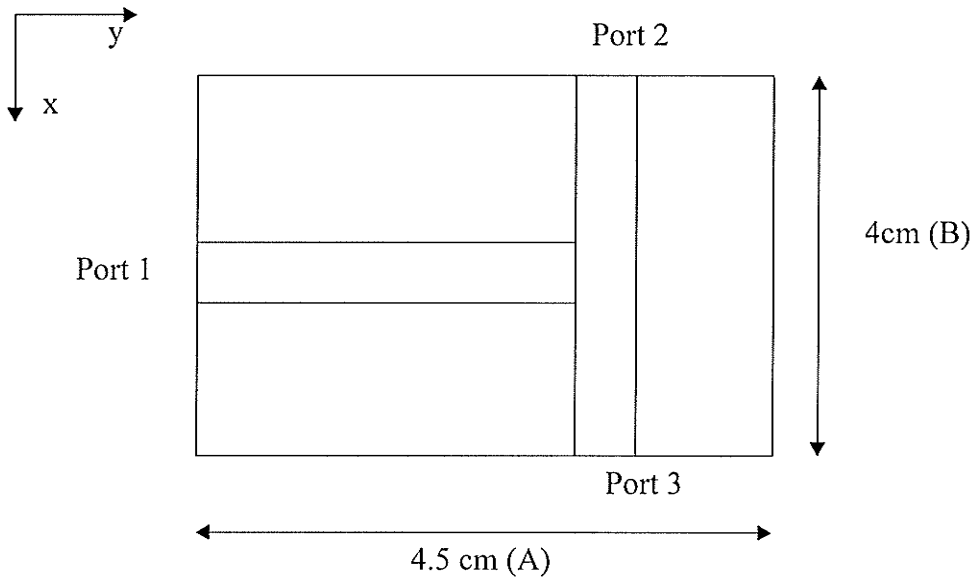

Figure 5.3 Geometry of the T-Junction.

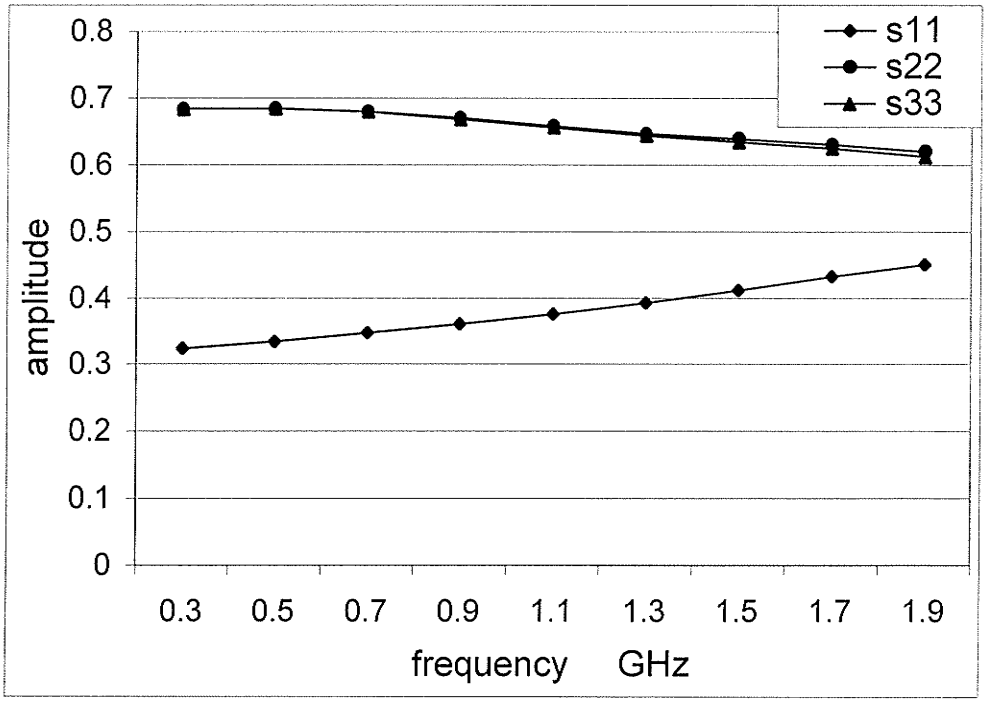

Figure 5.4 S- parameters for the T- Junction

resemble a via, as such a connection would introduce an impedance discontinuity in the current of the transmission line. The purpose of the example is to isolate the effects of the coupling only in the S-parameters extraction.

The results for the simulated S-parameters are shown in Figure 5.6. For the frequency range of the simulations it is shown that the coupling is not significant. A good agreement with the results from IE3D is obtained. The example demonstrates the accuracy of the technique for multiyear structures and in the presence of vertical conductors.

5.3.4 The Air-Bridge Circuit

The second example, shown in Figure 5.7 is an air bridge circuit. This circuit is used in MMICs, and can be a part of passive microwave components. The configuration consists of two microstrip transmission lines, crossing at right angel to each other. At the area of the crossing, one of the line is elevated in during the manufacturing process, such that no electrical connection exists between the two lines. The two lines share the common ground plane.

The simulation of the circuit is carried out, with matched termination for all ports. The parameters for the circuit are shown in the figure. The piece of the transmission line in the air is modeled by assuming an air dielectric layer with the relative dielectric constant is equal to one. This layer have zero reflection coefficients with the half-space air layer on the top. The vertical section of the transmission line has the same thickness as the horizontal section, similar to the pervious example.

The obtained current on the lines is utilized in the port de-embedding process to predict the S-parameters. The calculated S-parameters versus those obtained from the CAD

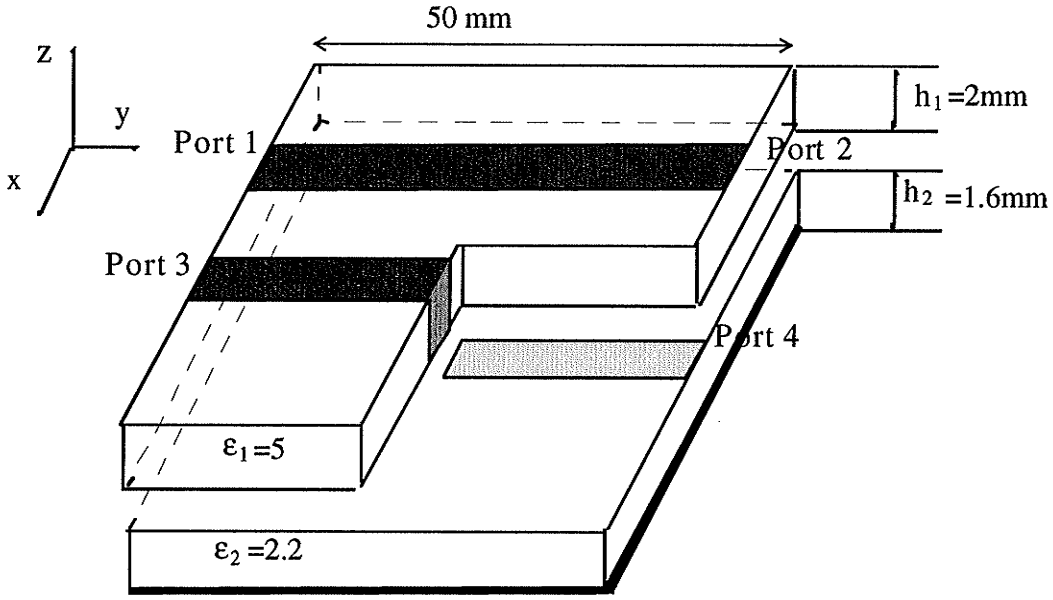

Figure 5.5 Geometry for transmission line circuit.

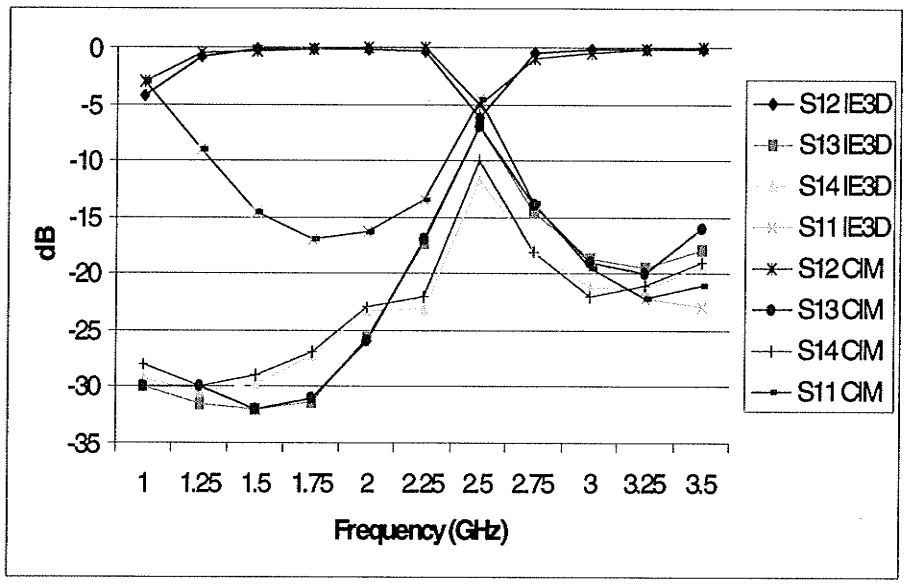

Figure 5.6 S-parameters for the transmission line circuit.

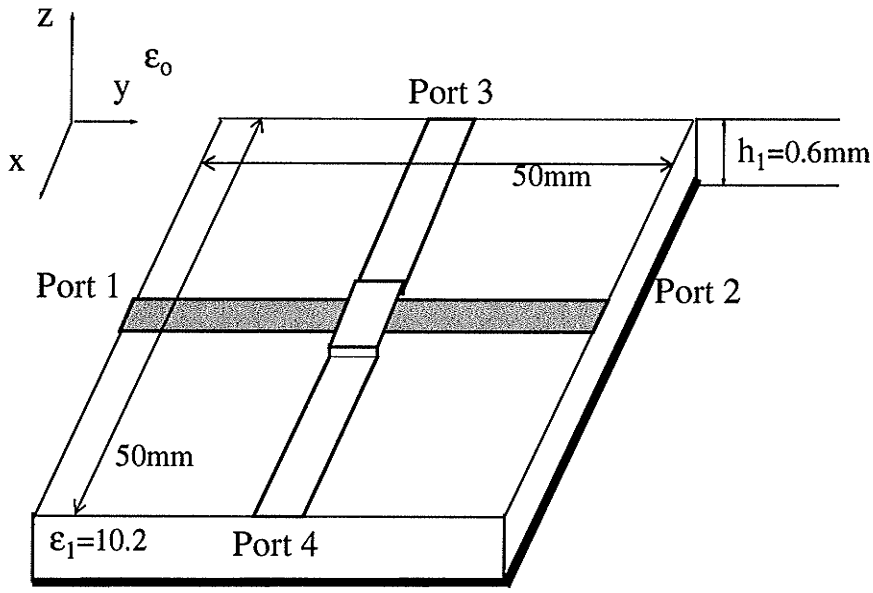

Figure 5.7 Geometry for the air bridge circuit

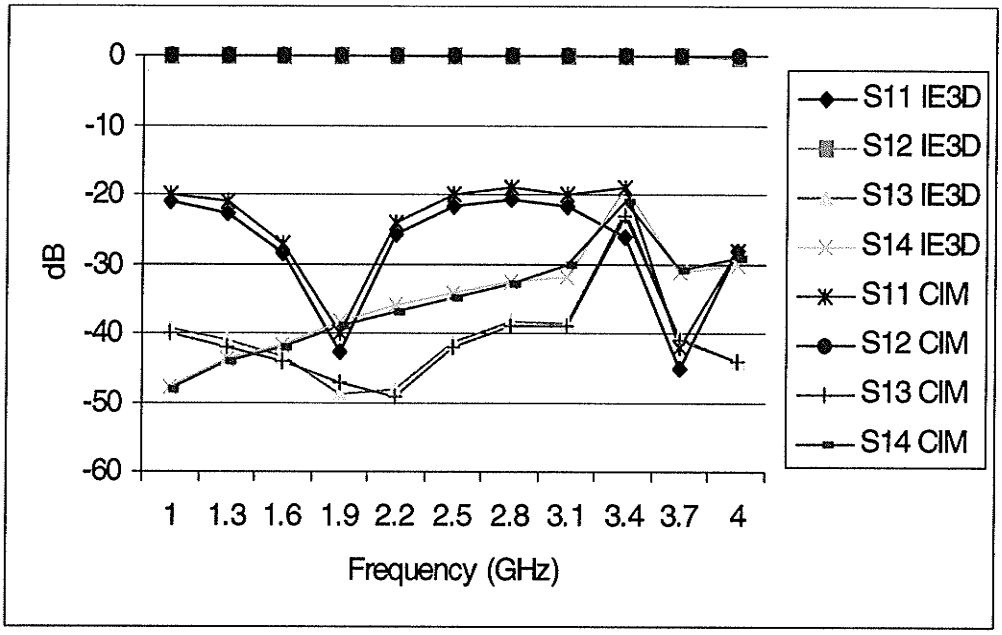

Figure 5.8 S- Parameters for the air bridge circuit.

software are shown in Figure 5.8. The agreement obtained is acceptable. The example shows the numerical accuracy of the analysis method for vertical conductors and air-suspended current segments.

5.3.5 Double-Stub Tuner

This example is for the microwave circuit shown in Figure 5.9. This circuit is a double stub tuner. The operation of the circuit is such that the reflection coefficient between the two ports is zero for all frequencies, until the resonance frequency band of the stubs. At this band, the reflection coefficient becomes high, and the circuit is non-conducting.

First, the geometry is implemented as a microstrip circuit. The dimensions of the circuit are shown in Figure 5.9. An infinite ground plane is assumed for the basic circuit. The first simulation results are shown in Figure 5.10, the extracted S-parameters are compared to those calculated by Ensemble. The results do not exactly match because the exact same discretization could not be used for both results. Ensemble utilizes a combination of triangular and rectangular basis functions to model the current. The agreement is still acceptable and confirms the expected operation for the tuner. There is no information from independent analytical or otherwise exact results or measurements to suggest which result is more accurate.

The circuit is then modified. A metallic plate is added to represent a finite ground plane. The new geometry is shown in Figure 5.11, and the dimensions of the finite ground plane are also marked. The simulation is repeated and the results are shown in figure 5.12. The results show how the operation of the circuit is altered by the presence of the finite ground plane. The current on the ground plane is modeled using the same rooftop basis

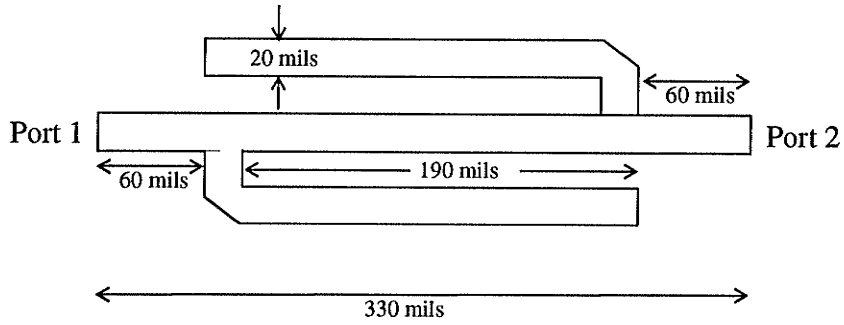

Figure 5.9 Geometry of the double stub tuner with infinite ground plane.

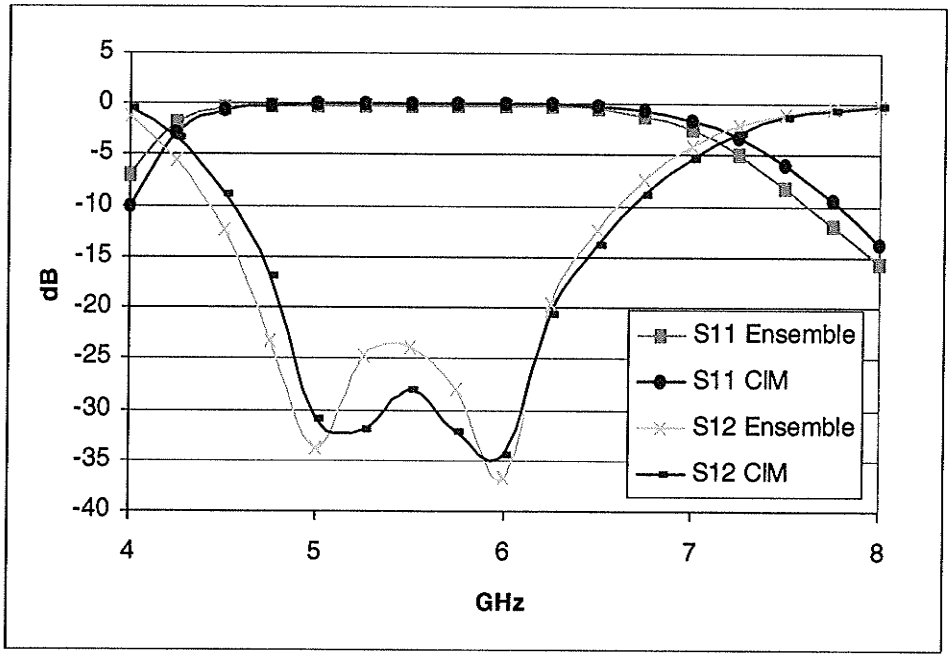

Figure 5.10 S-parameters for the double stub tuner with infinite ground plane.

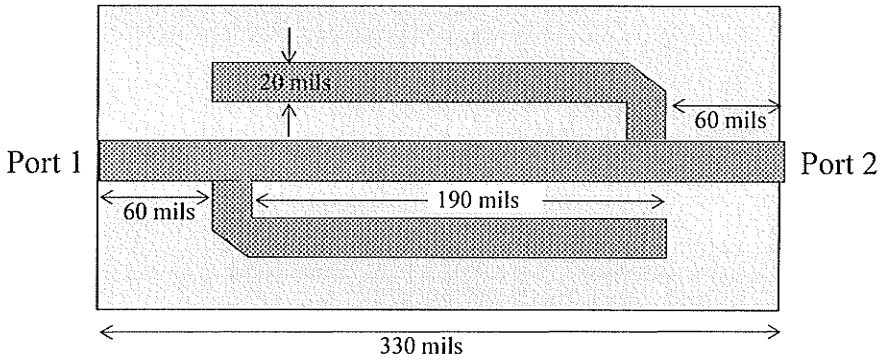

Figure 5.11 Geometry of the double stub tuner on finite ground plane.

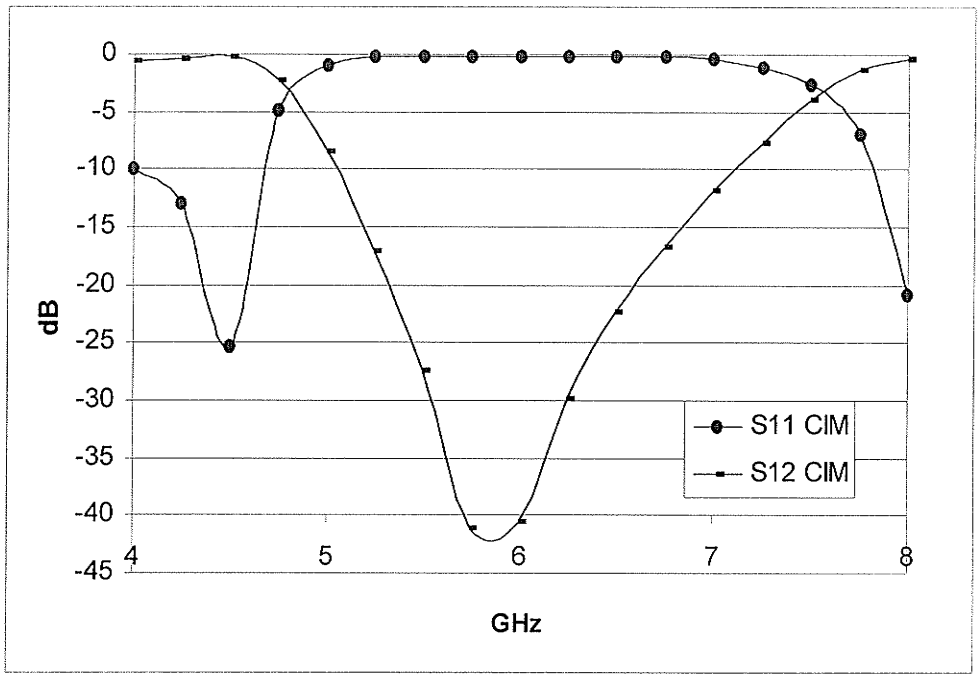

Figure 5.12 S-parameters for the double stub tuner on finite ground plane.

functions used for the other conductors. The feeding ports are terminated on the ground plane.

Next, the alteration is made to the original circuit to have an aperture in the ground plane, the geometry is shown in Figure 5.13. the dimensions of the aperture are shown on the figure. The results for the extracted S-parameters are shown in Figure 5.14. The results again show how the performance of the circuit is altered in these conditions, which might resemble a cut in the ground plane for the circuit. The current on the aperture is modeled using an equivalent magnetic current, as discussed in Chapter 3.

Finally those two modifications are combined, such that the circuit will have a finite ground plane with an aperture in it. The geometry is shown in Figure 5.15. The simulated S-parameters are shown in figure 5.16. The results are significantly altered from the original case and the basic operation of the circuit is almost entirely lost. The current on the ground plane is modeled as electric current, no equivalent magnetic current is assumed on the aperture, since the ground plane is finite.

This example proves the versatility of the methods and its capability to model basic and complex microwave circuits in a variety of operating conditions. The discretization used in this model is to divide the width of the line into 4 cells and the length to have 32 divisions per wave length for the transmission lines. The finite ground plane and the aperture needed fewer divisions, with 16 divisions per wavelength for the length and width are used.

5.4 Coplanar Waveguide Structures

Coplanar waveguide (CPW) structures are preferred over microstrip lines or

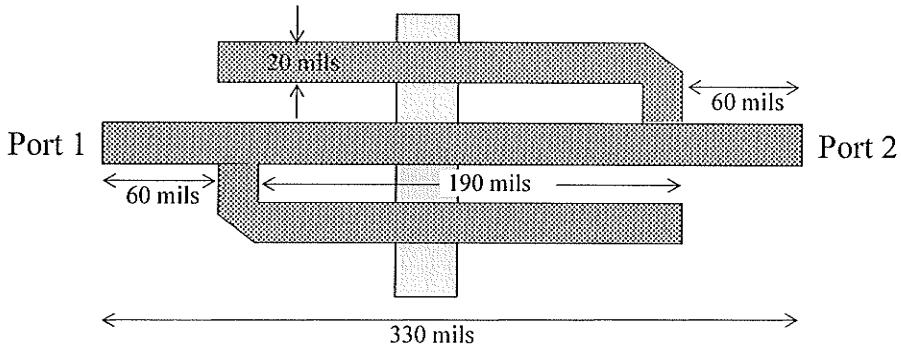

Figure 5.13 Geometry of the double stub tuner with infinite ground plane and slot in the ground plane.

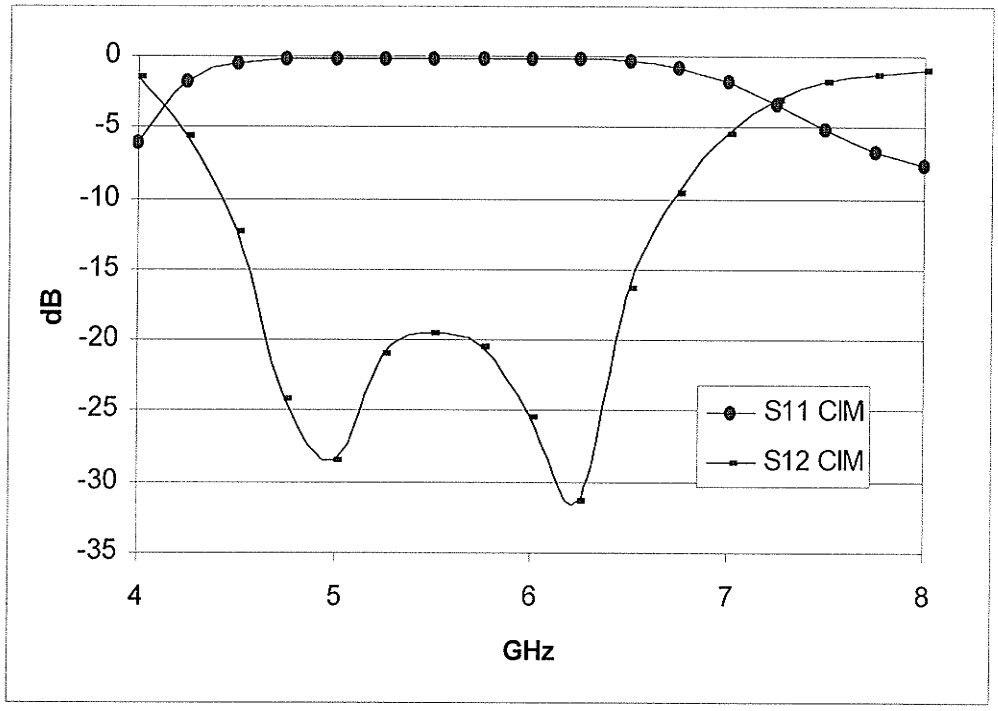

Figure 5.14 S-parameters for the double stub tuner with infinite ground plane and slot in the ground plane.

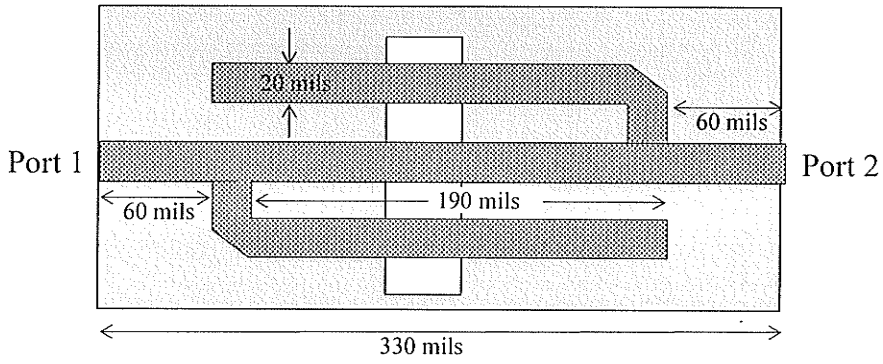

Figure 5.15 Geometry of the double stub tuner with finite ground plane and slot in the ground plane.

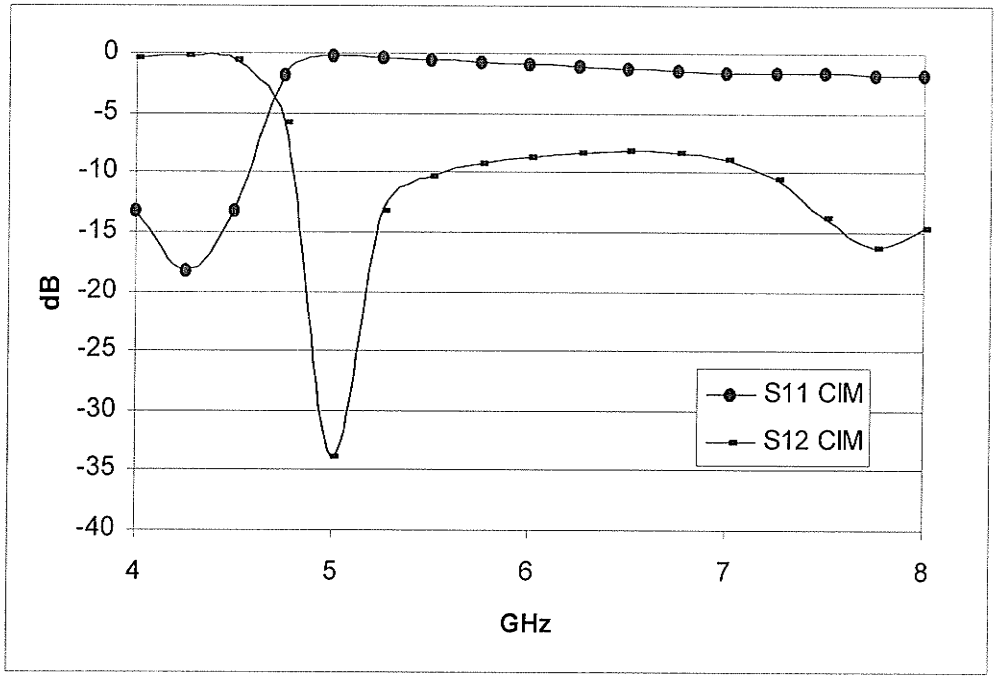

Figure 5.16 S-parameters for the double stub tuner with finite ground plane and slot in the ground plane.

striplines in millimeterwave circuits [90]. This is due to some of the appealing properties of the CPWs such as: there is no need to drill via holes for grounding purposes and for shunt connections as in microstrip lines. In addition, the impedance of CPWs is controlled via the slot to strip ratio, hence there is no need to use thin substrates in order to get higher impedances such as in stripline or microstrip circuits. The main drawback from a physical point of view is that CPW lines take considerably more area to implement than microstrip lines.

In this section, the application of the CIM to CPW structures used in [110] is investigated. The structure is an interconnect that is used as a transition from a flip-chip device to a printed circuit board. The structure is shown on figure 5.17. The width of the center conductor in the structure is kept constant throughout the simulations at 50 μm. The gap width V, height of the transition H and the length of the overlap lp between the two CPW sections are varied to study their effect on the electrical performance of the structure.

The structure is simulated from 1GHz to 100GHz with a step of 4.2GHz. The wide bandwidth is needed for digital signals at 10-20GHz that have a power spectral density components that exceeds 100GHz, starting from DC. Hence, the structure needs to have good electrical performance over this wide frequency band. The structure is physically small and is modeled as finite. Thus the two ground segments are taken as 200 μm wide segments and the electrical current on them is segmented and modeled, similar to the center conductor. The vertical transition region is modeled as vias. No magnetic current is assumed in the gap since the structure is finite. The dielectric layers are assumed infinite in the lateral directions. Since the structure is much smaller than the simulation wavelength at the lower frequencies, the segmentation is not critical. The segmentation is altered for

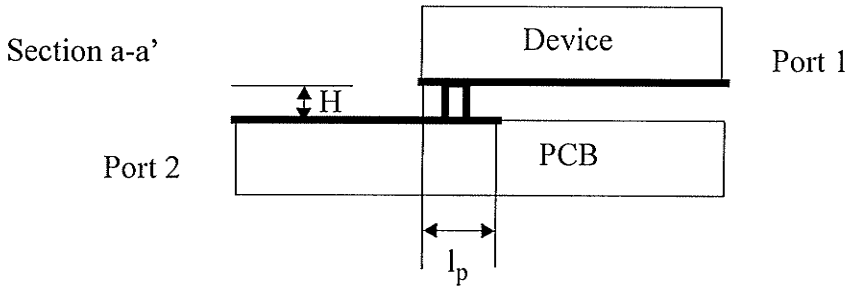

Flip chip interconnect, CPW transition and its dimensions

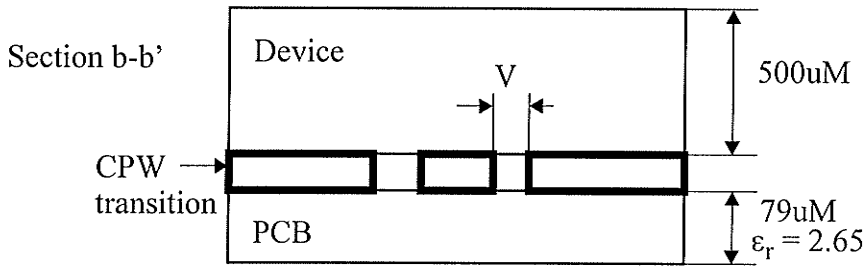

Section through the CPW transition

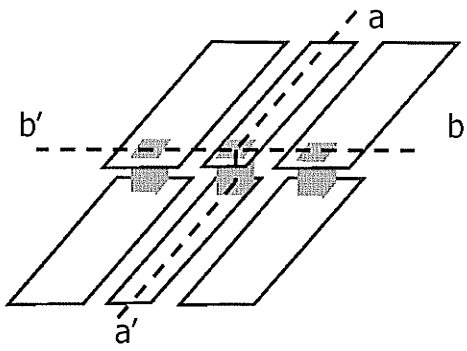

Figure 5.17 Geometry of the coplanar waveguide (CPW).

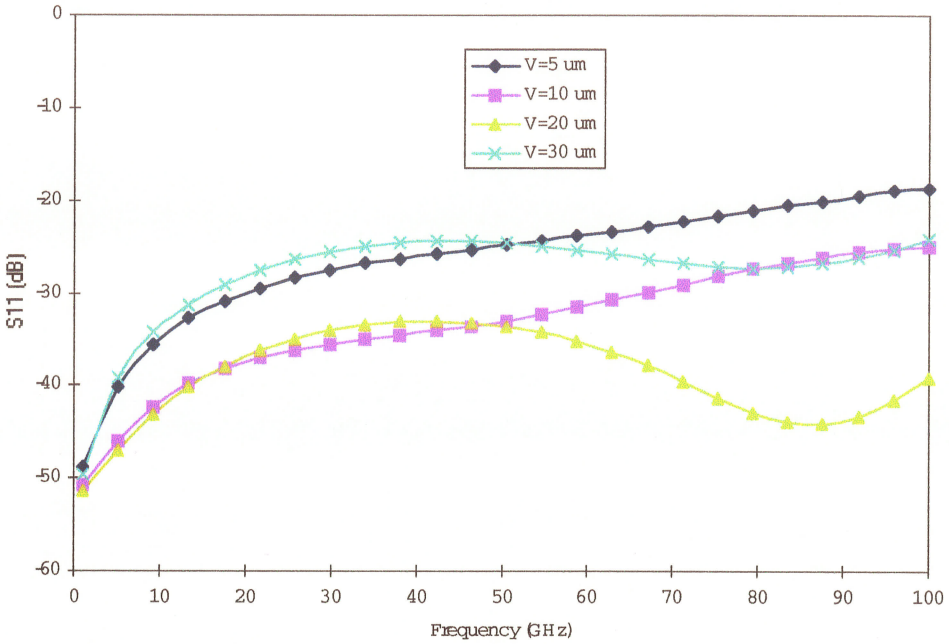

Figure 5.18 Magnitude of S_{11} versus frequency for the CPW structure H=40 μm, lp= 40.

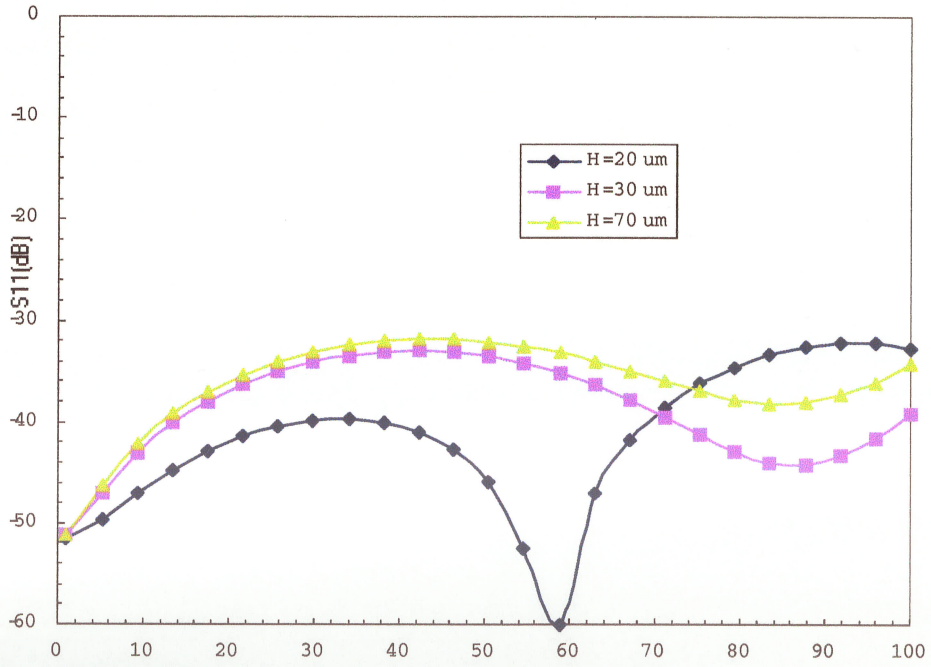

Figure 5.19 Magnitude of S_{11} versus frequency for the CPW structure V=30 μm, lp= 40.

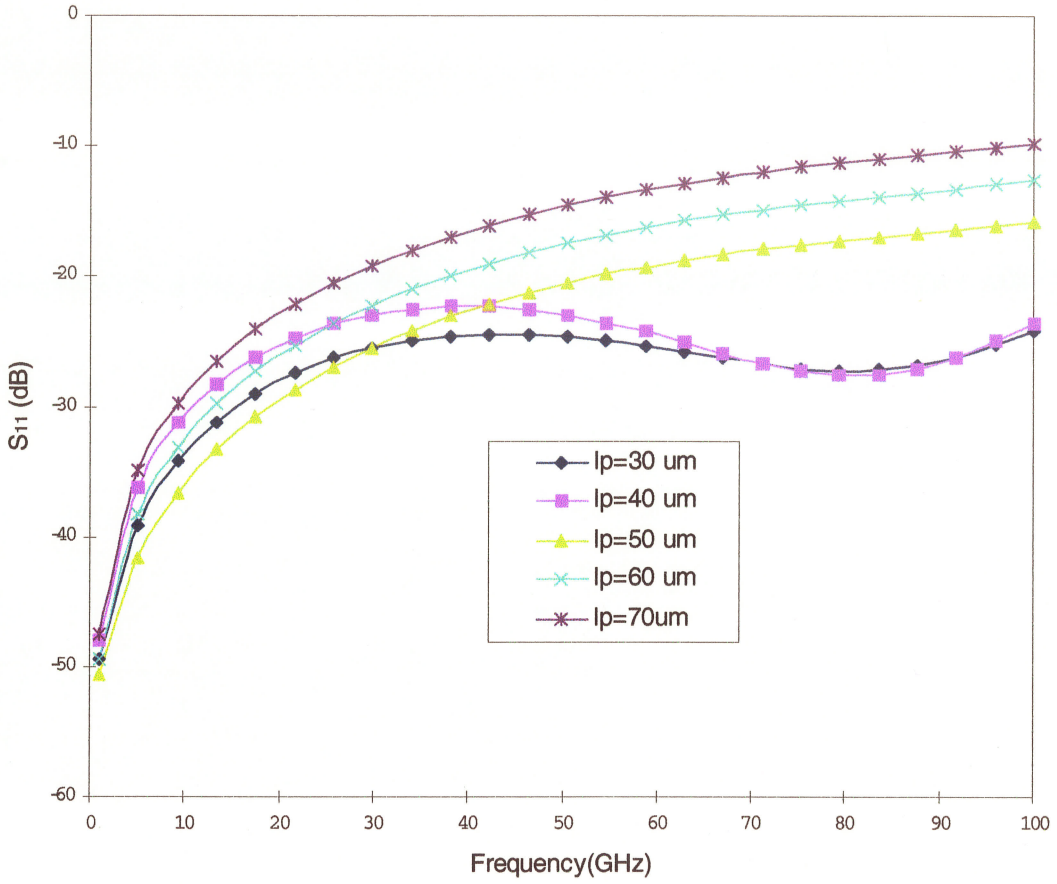

Figure 5.20 Magnitude of S_{11} versus frequency for the CPW structure V=30 μm, H= 40.

higher frequencies, starting at 30GHz, with each frequency having a different segmentation.

The results for the simulations are shown in figures 5.18, 5.19 and 5.20. In each of the three plots two of the three parameters (V, H and lp) are kept constant and the third is varied. The magnitude of the reflection coefficient S_{11} is plotted against the simulations frequency. It is evident from the simulation that the reflection can be kept below 30 dB for the entire frequency range of interest with the careful selection of the parameters. The structure shows promise for using in flip-chip technology.

5.5 Conclusion

This chapter presented the application of the CIM analysis method to a variety of microwave circuits and circuit building blocks. The accuracy of the method is first assessed versus an exact analytical solution for a quarter wave length stripline. Very small error levels can be obtained by increasing the number of divisions across the line width.

Other examples presented confirmed the accuracy of the method against known analytical and commercial CAD software packages. The analysis method is versatile and is able to handle a wide mix of geometries in different operating conditions, while maintaining the numerical efficiency of the CIM. In the example of the CPW structure, the method is applied to a wide frequency band with consistent results. This shows that the method can be used in the millimeter wave range.

CHAPTER 6

Application to Electromagnetic Compatibility in PCBs and MMICs

6.1 Introduction

Virtually any electronic system components can pick up unintended radiation. These components are called unintentional receivers, as opposed to antennas which are intended to receive radiation. The source of this radiation can be external systems, such as FM radio waves or signals used in wireless communications, or internal system components such as surges in the power supply system or emissions from high frequency components. This unintentional reception can compromise the signal integrity inside the electronic system, or interfere with its over all function. The problem becomes more emphasized when the component size approaches one tenth or more of the signal wavelength ($D \geq 0.1\lambda$) .

Hence, the science of electromagnetic compatibility (EMC) is concerned mainly with the design of electronic systems such that the interference to or from these systems will be minimized. A system will be electromagentically compatible if it satisfies two criteria [111]:

1. It does not cause interference with other systems or itself.

2. It is not susceptible to emissions from other systems.

The compatibility standards with other systems are usually regulated by laws imposed by the regulatory agencies. While the interference within the system components is studied during the product design.

There are three aspects to EMC problem dealing with interference between the various components of the system under study. These aspects are the source (emitter) of the radiation, the coupling path, and the receptor. Accordingly, there are three ways to prevent this interference, namely, to suppress the emission at its source, to make the coupling path inefficient, and to make the receptor less susceptible to the emissions.

6.2 Electromagnetic Interference (EMI) Analysis

The electromagnetic interference analysis to any electronic system deals with various aspects. The two aspects that are related to radiation are radiated emissions and susceptibility or immunity [112]. Both are tightly monitored in any consumer electronics market. As printed circuit boards (PCBs) are the heart of most systems, modeling of radiated emissions and susceptibility to radiation for PCBs are an integral part of the design process of all new high-speed digital products. The increase in clock frequency and the associated decrease in rise/fall times make the early detection of emissions problems from PCBs in the design process vital.

Most of the focus in EMI modeling has been on radiated emissions rather than immunity. The problem of radiated emissions normally had precedence over immunity as it is tied directly to the ability to sell the product, i.e. if the product exceeds the limit in

radiation testing it could not be sold until this problem is fixed. On the other hand, immunity to radiation was considered a product performance issue and thus less critical. The new regulatory requirements and the increased density of electronic devices expand the emphasis on susceptibility or immunity issues. Many of the techniques developed for the analysis of radiated emissions from PCBs can be modified to model immunity problems. Table 6.1 shows types of EMI/EMC tests conducted according to the European standards, the second row in the table is the test concerned with the emissions and immunity.

Table 6.1: Various EMC/EMI tests.

European Norm	**Area of Application**
EN 61000-4-2	Electrostatic Discharge (ESD)
EN 61000-4-3	Radiated EM field
EN 61000-4-4	Burst/ electrical fast transients
EN 61000-4-5	Surge
EN 61000-4-6	Conducted RF disturbance
EN 61000-4-8	Power frequency Magnetic Field
EN 61000-4-11	Voltage dips, interruptions

6.2.1 Radiated Emissions Modeling

Calculating radiated emissions from PCBs is a straight forward process once the currents on all the conductors are accurately determined. However, predicting the currents becomes more challenging with the increasing complexity of the PCB layout. A compromise is usually necessary between accurately modeling the electric function of the active components on the PCB and the exact geometry of the interconnects system, namely the traces, vias and the ground plane.

Two main approaches are used to simulate PCB topologies, they are: the signal integrity simulations (also known as circuits-based simulations or Spice-type simulations) and the full-wave electromagnetic solutions. Each approach puts an emphasis on one part of the PCB and makes simplifying assumptions regarding the other. The first part being the active devices and the other is the interconnects system.

In the signal integrity approach, the electrical devices are modeled accurately, the appropriate excitations are given, but the geometry is greatly simplified. For example, all ground planes are considered ideal. These simulations are thus unable to correctly predict the currents in the interconnects system in the presence of slots, holes or cutouts in the ground plane. These modifications to the ground plane make the return path for the current on the traces imperfect, thus increasing the common mode currents. In contrast to differential mode currents, common mode currents have a significant contribution to the overall radiated emission, since image currents on the ground plane do not cancel them.

Full-wave electromagnetic solutions are able to analyze accurately all parts of the interconnects system, geometry wise. If we also take into account the increasing clock frequency in digital systems, using full-wave field solutions to accurately predict radiated emissions levels becomes inevitable. Integrating active devices into the full-wave solution is necessary to the overall accuracy of the modeling process.

Time domain based full-wave analysis techniques such as the finite-difference time domain (FDTD), and the transmission line matrix method (TLM) have been used to predict emissions from PCBs. These techniques are versatile, and able to model complex, inhomogeneous geometries. Running the simulations in the time domain, allows for the frequency response at multiple frequency points to be obtained using a single simulation.

On the other hand, it is computationally very intensive, and modeling small features on the conductors puts restrictions on the grid size used. Variable mesh size can be used at different locations at the expense of a much added complexity to the numerical technique.

The mixed potential integral equation (MPIE) presents an interesting alternative full-wave solution. Coupled with the method of moments it proves to be a powerful modeling tool in the microstrip antennas and microwave circuits areas. As discussed in earlier chapters, dyadic Green's functions are used to account for the boundary conditions between different dielectric layers. Utilizing the CIM to avoid the direct numerical integration for the Sommerfeld integral enhances the numerical efficiency for the technique. Segmentation is carried out for the current on the conductors only, thus resulting in a relatively smaller impedance matrix, as compared to the impedance matrix obtained in the surface-volume integral equation formulation. Variable mesh size can be used without adding considerable numerical effort to the technique.

It should be noted that analyzing an entire, complex PCB, with many active components on it, is a daunting task for any simulations technique. The memory and computational requirements would make this task impossible for even a moderately complex PCB. The approach that is used to tackle the task of assessing the radiated emissions from a typical board is to use a combination of engineering sense, experience and/or simple numerical experiments and measurements to isolate potential problematic areas. Once this is done, the geometry of these areas is imported in the analysis software for detailed investigation. The "divide and concur" approach is maintained until all the "hot" radiation spots are identified.

6.2.2 Susceptibility Modeling

Using numerical analysis to predict radiation susceptibility of PCBs can be a time-consuming process. The complexity of the problem arises from the elaborate topology of the PCB, and the fact that the analysis has to be repeated for multiple excitation fields.

The problem of external field coupling to PCB networks has been studied in the literature. For general metallic objects inside gigahertz transverse electromagnetic (GTEM) cells, a study [113] was performed using the FDTD technique and the results were compared to the measurements performed inside the cell. To study the problem of external field coupling to multiconductor transmission lines (MTL) a comprehensive analytical and experimental study using the quasi-TEM method [114] was used. This study, also incorporated active devices successfully with MTL structures. For susceptibility analysis of general PCB structures the MoM was used in [115]-[116] and the TLM in [117].

In analyzing immunity to radiation, the MoM becomes particularly efficient; once the impedance matrix is constructed and inverted at a certain frequency, all incident field angles and polarizations can be examined, without having to rebuild the impedance matrix. The solution of the matrix equation produces the currents on the conductors. Assessment of these calculated currents will aid the PCB designer to evaluate the immunity of the simulated structure to the incident fields, or decide if the induced currents are of such a level that it will interfere with the operation of the PCB under investigation.

6.2.2.1 Susceptibility Modeling Procedure

An exhaustive testing procedure for the susceptibility would involve placing an external source at various locations, and then measuring the coupled fields at several points

on the tested PCB. The test needs to be repeated for all frequencies of interest, and various source and receiver orientations. Obviously, this elaborate testing procedure would be time consuming. Running numerical simulations using the same procedure would be even more time consuming. This suggests a need for a more efficient methodology to test the immunity of PCBs to external fields. The process would start again by identifying sensitive locations on the PCBs, which can be done using a combination of engineering sense, experience and/or simple numerical experiments and measurements. These sensitive locations are the measurements points on the PCB under test.

Next, the source locations are studied, and the question becomes do all the possible locations need to be tested, or can the location that is going to result in the highest field coupling to a specific measurement point be identified without this comprehensive search? The answer to this question can be obtained in the light of the reciprocity theorem. The theorem states that a response of a system to a source is unchanged when the source and the measurement point are interchanged. Hence, if we use the identified measurement points on the PCB, and perform an emissions test using these points as source locations. The location where the emissions are highest will be the same location where if a source is placed will couple the most energy to this measurement point. Using these two steps, a finite set of measurement points and corresponding source locations are identified. The numerical simulations can proceed for this finite set.

Any given source can be modeled as a set of incident plane waves on the given PCB. The efficiency of the MoM is evident in this step, finding the response to multiple excitations does not require the repeated evaluation for the inverse of the impedance matrix, the inverse is calculated once and then is multiplied by the incident vector corresponding

to the incident plane wave.

Therefore, the procedure followed in this research to asses the immunity or a particular location on a PCB to externally coupled fields is summarized in these steps:

- Identify "sensitive" location(s) on the PCB structure.
- Perform a radiated emissions analysis considering a source at each location.
- Select external field sources, model them as plane waves.
- Calculate induced voltage at each location.
- Perform circuit analysis to determine the effects.

6.2.3 Frequency Sweeping

The MoM matrix is evaluated and the resulting system of linear equations is solved at each frequency point of interest. The process of repeating the solution at multiple frequency points is called frequency sweeping. Normally, the EMI investigation of a PCB spans a wide frequency band, thus the numerical efficiency of the method becomes more critical. Several methods were adopted to enhance the frequency sweep associated with the method of moments. Techniques such as the complex frequency hopping and the asymptotic wave expansion were used to decrease the numerical effort associated with filling the impedance matrix elements at different frequency points. These techniques focus on predicting the values of the Green's functions or the elements of the impedance matrix at intermediate frequency points using information from other points at which the functions are calculated.

The special feature regarding the CIM is that the complex coefficients and amplitudes for the images are the only parameters needed to calculate the Green's functions

(GFs) closed form equations at any point. The radial distance is then substituted in these equations to evaluate the GFs at any point. Thus if we can interpolate the values of the complex coefficients and amplitudes at the intermediate frequency points, the GFs would be known completely.

The accuracy of these interpolations depends largely on the behavior of the GFs with respect to the frequency and the behavior of the complex amplitudes and coefficients with frequency. It was shown in [118] that the GFs themselves are smoothly varying with frequency. It was also pointed out by Torabian and Chow [119] that the variation of the coefficients of the complex images is not a smooth function of frequency. However, we notice that the simulations performed in [118] span a very wide frequency range and use only a few complex images to represent the potential function. The investigations carried out here suggest that the more complex images used, the smoother their frequency variations become. Increasing the number of complex images used does not add a significant overhead on the numerical algorithm, but is does allow for the interpolation of the complex coefficients and amplitudes for the complex images. The simulations show only a fraction percentage error for using the interpolation to predict the coefficients rather than using the GPOF to calculate them. In addition, the frequency range considered in EMI simulations is much smaller, in contrast to the one used in [119]. The result is an enhancement in the numerical efficiency of the overall algorithm.

The algorithm starts by computing the complex images coefficients at selected intervals in the frequency span. Linear interpolation is then used to predict the coefficients in between the calculated values. The impedance matrix filling then takes place, and the impedance matrix is solved at each frequency point. The resulting algorithm is simple,

reliable and easier to implement than, for example, the complex frequency hopping algorithm.

6.3 Time Domain Signal Integrity Simulations

Simulating high speed digital interconnect systems in time domain is of primary importance to ensure that the product meets electrical performance metrics. Circuit simulators, such as SPICE, have been developed to solve nodal equations for electrical networks and obtain currents and voltages given initial conditions and excitation sources. These simulators are also extended to handle transistor circuits. For digital circuits, simulating the output buffer stage with the transmission line interconnect system is the goal for signal integrity analysis. The signal integrity analysis aims to ensure that digital signals, modeled as analog waveforms, have good signal quality and arrive at their receiver within its allotted time window.

The fundamental difficulty encountered in integrating transmission line simulation in a transient circuit simulator such as SPICE arises because circuits containing non-linear devices or time dependent characteristics must be characterized in the time domain. On the other hand transmission lines with loss, dispersion and interconnect discontinuities are best simulated in the frequency domain. Several approaches have been tried with varying degrees of success.

The Laplace transform technique is good at handling multi-conductor transmission line systems. It is more efficient than the convolution technique, but it has a limited ability to handle frequency dependent effects. Also, problems dealing with nonlinear terminations restrict its usefulness. The method of characteristics [120] is relatively easy to use with the

conventional circuit simulators. It is restricted to low loss, dispersionless lines. Other techniques for simulating distributed element systems have been reviewed by Djordjevic, Sarkar and Harrington [121] and Schutt-Aine and Mittra [122].

In [123] the frequency domain Y parameter description of the distributed network is converted to a time domain description using a Fourier transform. This time domain description is then the Dirac delta impulse response of the distributed system. While the technique can handle lossy coupled networks, a difficulty arises as the Y parameters of a typical multi-conductor array have a wide dynamic range. Consequently, aliasing in the frequency domain to time domain transformation can cause appreciable errors in the simulated transient response.

An alternative formulation that avoids the dynamic range problems is given in [124], where, scattering parameter formulation is used in considering a parallel coupled transmission line system. Because of the limited range of scattering parameters this approach offers good computational stability and efficiency.

Another but more direct S parameter technique based on the approach in [123] is discussed in [125]. In this technique, a Green's function from the frequency domain S parameters is derived and used to develop a method for analyzing an arbitrary complex transmission line network terminated in nonlinear loads. The technique has reduced sensitivity to dynamic range problems as compared to approaches based on network parameters other than the S parameters. Nonuniform lines can be considered and the transmission line networks can be defined by network parameters derived through measurement or circuit simulation. An extension of the method to a generalized packaging analysis simulator was also presented in [125].

6.3.1 Convolution Method

The S parameters of a transmission line system describe the relative amplitude and phase of forward, V_j^+, and backward, V_j^-, traveling waves at each port and at each frequency on a transmission line of characteristic impedance Z_m.

Integration of the S-parameters into a transient circuit simulator requires that the description of the transmission line system be in terms of total voltages rather than traveling wave components. This can be achieved by terminating each port in its reference impedance so ensuring that there are no reflection, with respect to the system reference impedance, at the ports of the distributed network. More explicitly, the total transient response at port i of a transmission line system to a total voltage $E_j(t) = V_j^-(t) + V_j^+(t)$ with output impedance Z_m at each port is:

$$V_i(t) = \sum_{j=1}^{N} \int_{-\infty}^{t} g_{ij}(t-\tau)E_j(\tau)d\tau = \sum_{j=1}^{N} g(t) \otimes E_j \qquad (6.1)$$

where N is the number of external ports in the system and $g_{ij}(t)$ is the inverse Fourier transform of $G_{ij}(\omega)$.

Removing the effect of the reference impedance leads to a set of convolution equations which have the discrete form

$$V_i(n_t) = \sum_{j=1}^{N} \left[\sum_{n_\tau = 0}^{n_t} g_{ij}(n_t - n_\tau)V_j'(n_\tau) + \sum_{n_\tau = n_t + 1}^{N_T} g_{ij}(n_\tau)V_j'(0) \right] \qquad (6.2)$$

where,

$$V_j'(n_t) = V_j(n_t) - I_j(n_t)Z_m \qquad j = 1, N \tag{6.3}$$

In equation (6.2), N_T is the number of time points in the period of interest, $t = \Delta t \cdot n_t$ and $\tau = \Delta\tau \cdot n_\tau$ and $\Delta\tau$ and Δt are time steps. The introduced node sources V are now memory devices controlled by the present and past value of all virtual sources V_j''s.

Equations (6.2) and (6.3) are a set of coupled non-linear equations and must be solved iteratively. In iterative vector form (6.3) becomes:

$$^{k+1}\hat{V}'(n_t) = {}^{k}\hat{V}(n_t) - {}^{k}\hat{I}(n_t)Z_m \tag{6.4}$$

and (6.2) becomes

$$^{k+1}\hat{V}''(n_t) = \Lambda\, {}^{k+1}\hat{V}'(n_t) - \hat{\alpha}(n_t) \tag{6.5}$$

where $\hat{\alpha}(n_t)$ is a vector with elements:

$$\alpha_i = \sum_{j=1}^{N}\left[\sum_{n_\tau=0}^{n_t-1} g_{ij}(n_t - n_\tau)V_j'(n_\tau) + \sum_{n_\tau=n_t+1}^{N_T} g_{ij}(n_\tau)V_j'(0)\right] \tag{6.6}$$

Λ is a matrix with elements $\lambda_{ij} = g_{ij}(0)$, and $^{k+1}\hat{V}(n_t)$ is chosen to minimize $\left|{}^{k}\hat{V}(n_t) - {}^{k+1}\hat{V}''(n_t)\right|$. Then,

$$^{k+1}\hat{V}(n_t) = {}^{k}\hat{V}(n_t) - J^{-1}({}^{k}\hat{V}(n_t) - {}^{k+1}\hat{V}''(n_t)) \tag{6.7}$$

Iteration would then proceed until some predetermined tolerance is obtained. That

is until $\left|{}^{k+1}\hat{V}''(n_t) - {}^{k}\hat{V}(n_t)\right| < \varepsilon$.

This convolution technique is implemented in the SPICE based circuit simulator Eldo from Mentor Graphics [126]. The simulation process starts with characterization of the interconnect system using the MoM code, and getting the S-parameter description for it. The S-parameter block is then inserted into a circuit file which contains the output buffer stage and the load. A time domain transient analysis is run and the results for the simulation is plotted as voltage versus time. In the next section, an example is presented on the implementation of the simulation process.

6.4 Numerical Results

This chapter presents the application of the CIM to estimate the radiated emissions levels from PCBs and to assess the susceptibility of PCBs to externally coupled fields. Interpolation of the complex amplitudes and coefficients for the complex images is used to enhance the numerical efficiency of the frequency sweeps. The solution method is applied to a number of examples of PCBs found in the literature. The examples analyze how the following structures affect the radiated emissions levels; vias, slot in the ground plane, gap in the ground plane, coupling between traces and I/O lines. The analysis method is then used to study some examples of external field coupling to microstrip circuits. An outline methodology is given to incorporate active devices with the analyzed circuit.

The computed radiated emissions levels are compared to the published results, good agreement is obtained. In actual digital circuits, when the geometry of the ground plane or the traces become complex, the CIM provides a combination of efficiency and accuracy

that makes it a valuable radiated emissions and susceptibility prediction tool.

Simulations are carried out to compare the accuracy of the technique against other published results. The selected examples represent analog and digital PCB components and building blocks that are reported in the literature. Each of the circuits is simulated to determine the amount of radiated emissions for a sinusoidal current source.

6.4.1 Vertical Connections and Finite Ground Plane

In the first example the effects of vertical connections and a finite ground plane on radiated emissions from a microstrip circuit are studied. The circuit in Fig. 6.1 consists of a microstrip line with air dielectric, the line width is 0.1cm, its length is 5.0cm and its height above ground is 0.2cm [127]. The structure is using a source at one end of microstrip line and a vertical conductor resembling a via connection to ground. Two cases for the ground plane are considered, the first case is the infinite ground plane, and the second case is the finite ground plane case, in which the ground plane dimensions are 7.5cm x 15cm. The results for the radiated emissions are shown in Fig. 6.2. The simulation is carried out for the frequency range shown on the figure. The results based on the MoM analysis are compared to the infinite ground plane results published in [127]. The results for the radiated emissions for all examples including this one are plotted as maximum radiation field amplitude on a sphere of radius 3m centered around the source point.

Next, the dimensions of the structure are modified to be 6mils for the line width, 6inch for it length and 7mils for the height. The ground plane dimensions are 0.3inch x 6.1inch. The dielectric constant of the substrate is 4. The characteristic impedance for the line at these dimensions is 79.7ohms. Fig. 6.3 shows the real part of the input impedance

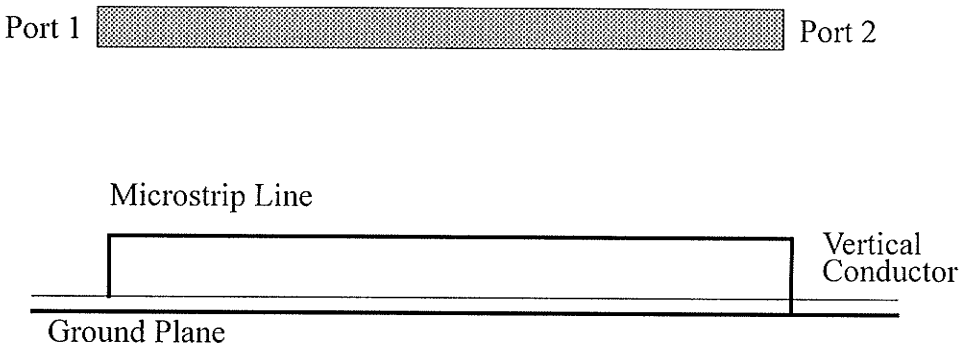

Figure 6.1 Microstrip line with vertical connections.

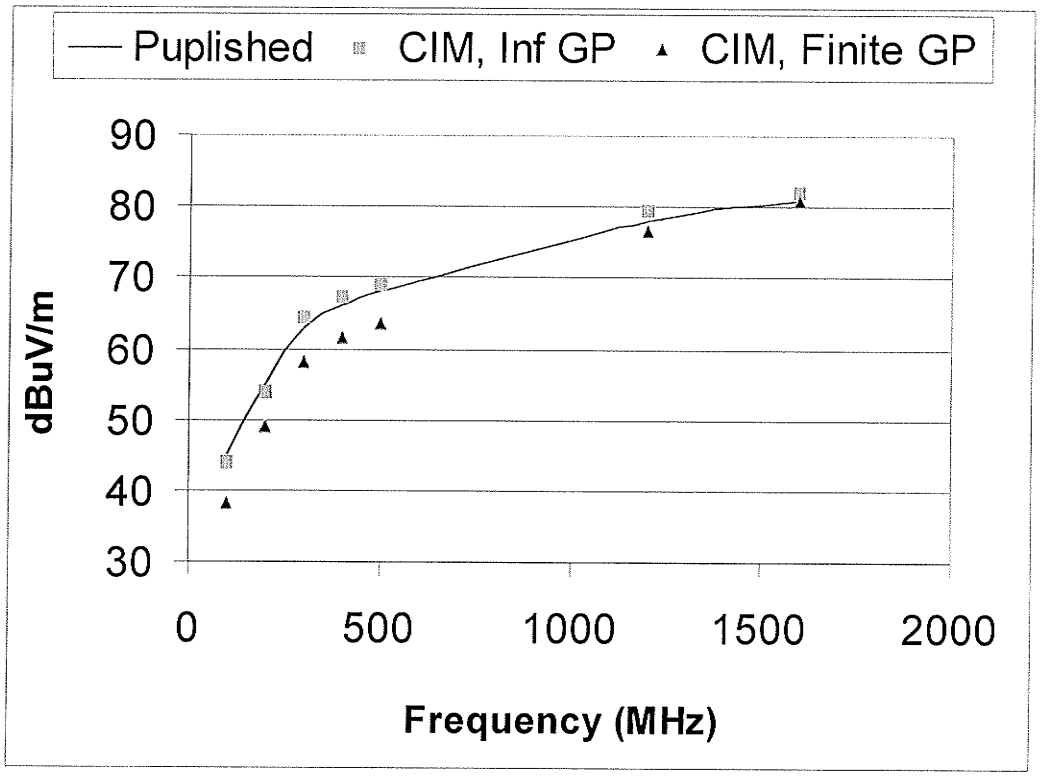

Figure 6.2 Magnitude of the electric field plotted as worst case vs. frequency.

for the structure for the frequency range shown in the figure.

6.4.2 Effects of Slots and Gaps in the Ground Plane

The simulations carried out in this section computes the emissions from microstrip circuits in the presence of gaps and slots in the ground plane. The first example is shown in Fig. 6.4, which is the same geometry and same dimensions as in the previous example, only the ground plane is infinite and a slot of dimensions 0.5inch x 2inch is centered under the microstrip line, also the vertical connection is removed and replaced with an open circuit termination. The results for the radiated emissions is shown in Fig. 6.5, which illustrates the variation of the level of emissions with the geometry of the line.

In the example shown in Fig. 6.6 another microstrip circuit [128] is studied. It represents a 20cm long and 0.5cm wide 50ohms microstrip transmission line. The height of the microstrip above the ground plane is 0.164cm and the relative dielectric constant of the substrate is 2.3. The ground plane is finite and its dimensions are 20cm x 20cm. The gap in the ground plane has a 2mm width and its length is varied from 0 to 19cm. The simulations are carried out at 50MHz for this structure. Results are shown in Fig. 6.7.

6.4.3 Coupling with I/O lines

In this example a microstrip circuit with a long I/O line is simulated [129]. The circuit is depicted in Figure 6.8. The dimensions of the lines are shown on the figure, the width of all the lines is 8mils and the spacing between the line with the source and the I/O line is also 8mils. The substrate has a 4.5 relative dielectric constant and 10mils height.

The results for the radiated emissions are shown in figure 6.9. The results show that

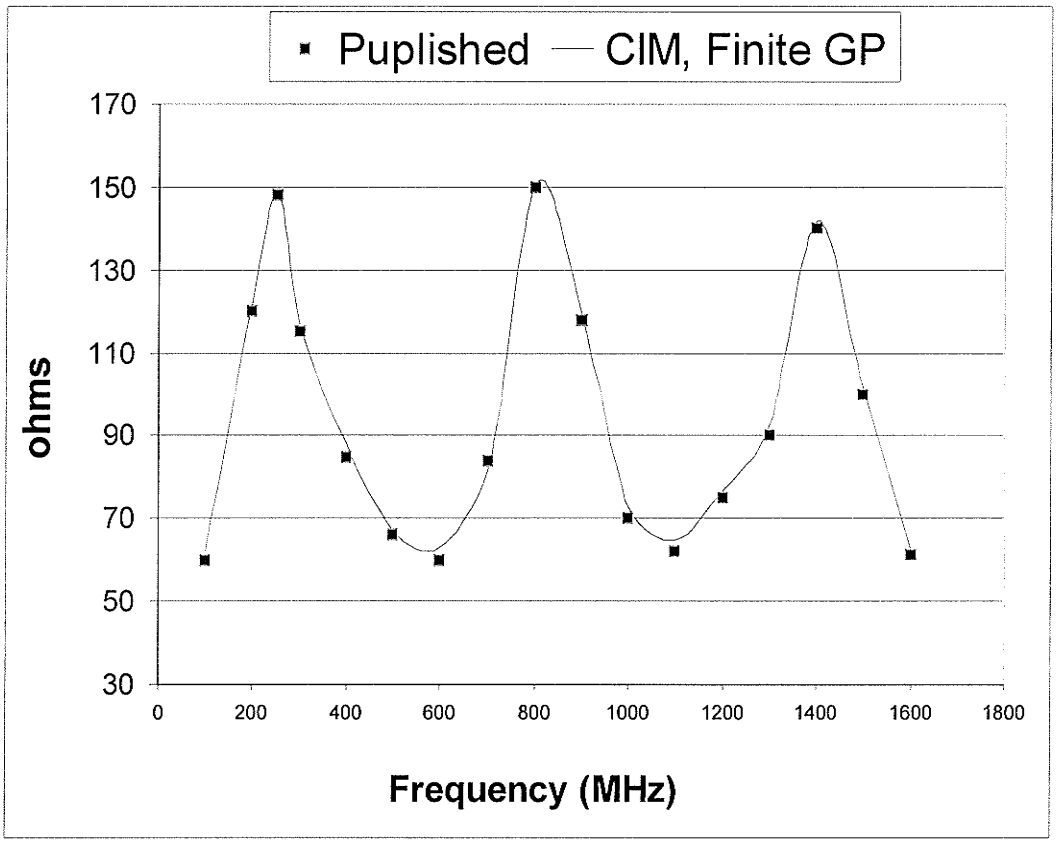

Figure 6.3 Variation of the real part of the input impedance with frequency.

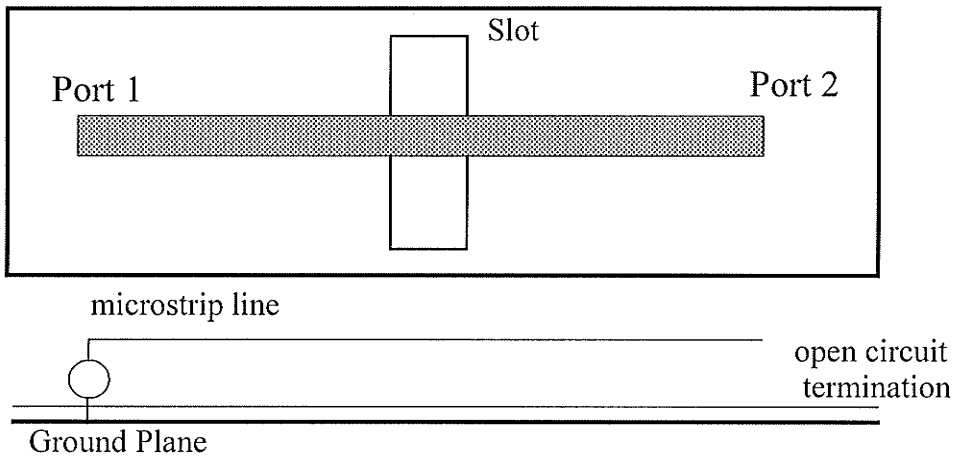

Figure 6.4 Microstrip line with slot in ground plane.

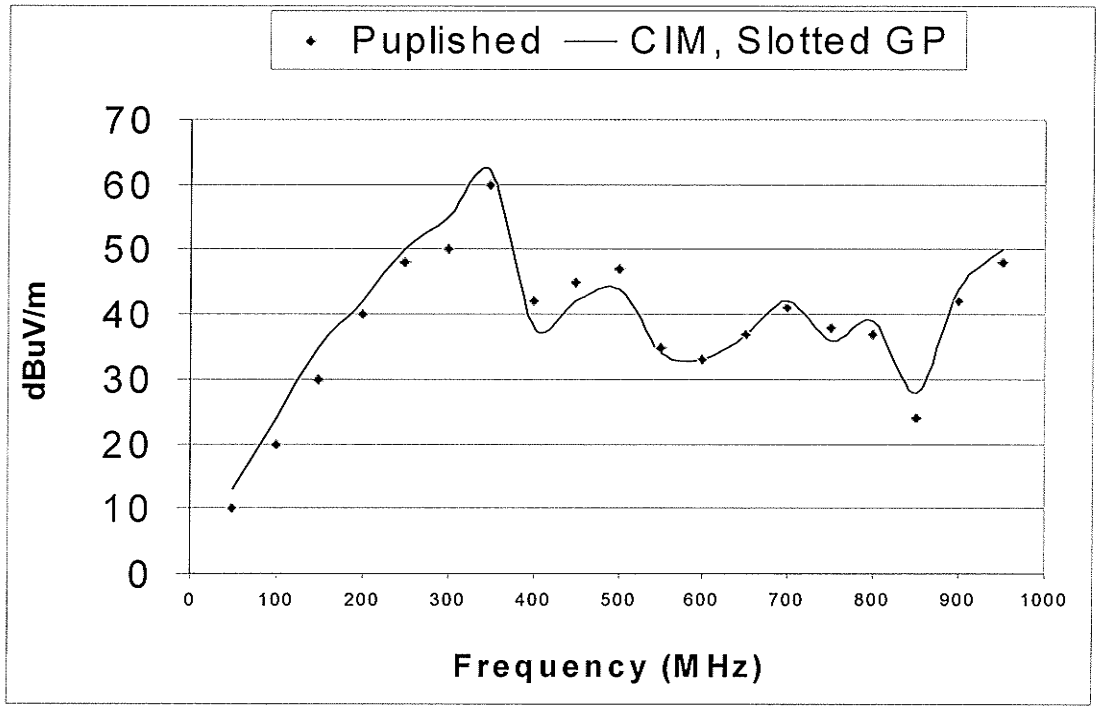

Figure 6.5 Magnitude of the electric field plotted as worst case vs. frequency.

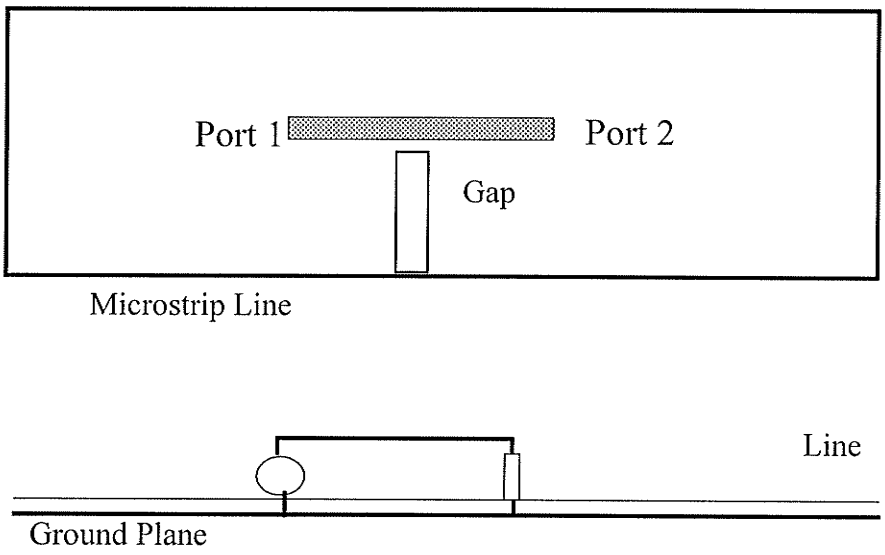

Figure 6.6 Microstrip line with gap in the ground plane.

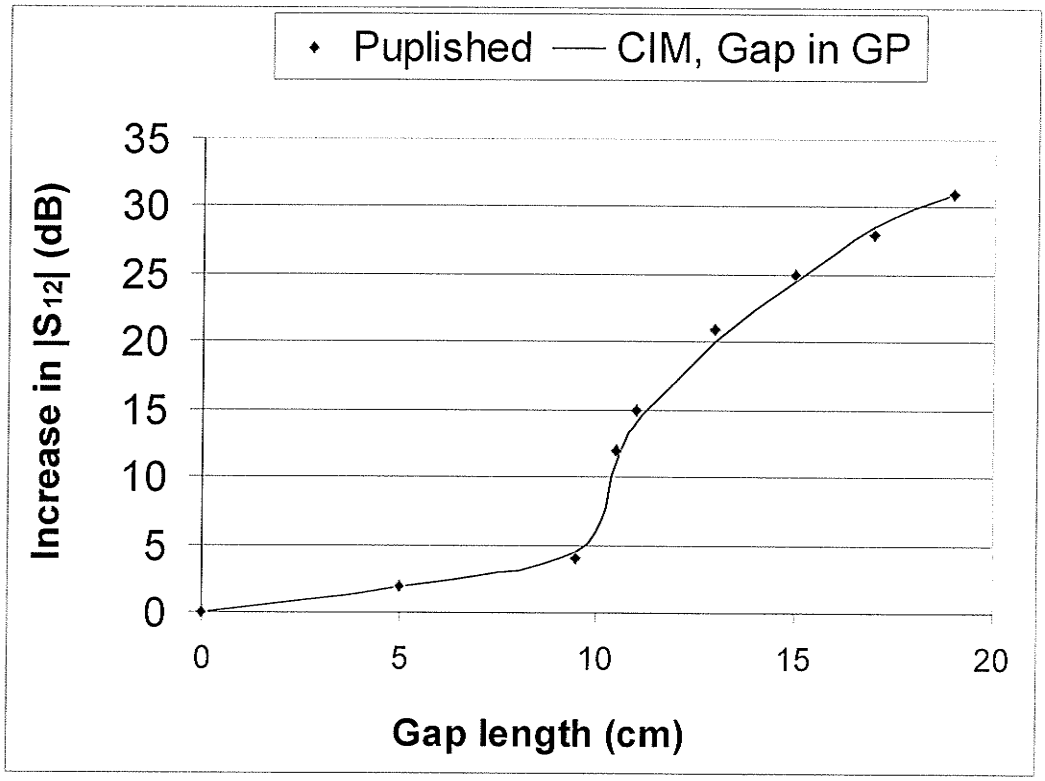

Figure 6.7 Increase in $|S_{12}|$ as a function of the gap length.

even such a simple geometry can have emissions level that exceed FCC Class B limits for the frequencies tested. Increasing the spacing between the lines reduces the coupling and emissions levels [129].

6.4.4 Immunity Assessment

The geometry in this example is the same T-Junction geometry used in section 5.3.2 of the previous chapter. Here the problem of external field coupling to this kind of microstrip circuits is considered. The simulation is first carried out at 300MHz. At this frequency the longer dimension of the T-Junction is approximately one tenth of the effective wavelength for the microstrip structure. The simulation is then repeated at 1.1GHz, for which case the same dimension approaches half the effective wavelength. X and Y-polarizations for the incident wave are considered. The normalized magnitude of the currents on the surface of the conductors is shown in Figure 6.10. and Figure 6.11. The wave is propagating in the positive Z direction.

6.4.5 Time Domain Signal Integrity Simulations

The example in this section uses the double stub tuner circuit simulated in the previous chapter, Fig. 5.10 and Fig. 5.12 for the cases of the ideal ground plane and a gap in the ground plane. The S-parameters as a function of frequency are the input to the simulations. The circuit is shown in Fig. 6.12, though simple it represents a typical single-ended digital connection. The source represents the output stage of the driver, modeled as a simple pulse voltage source in this example to prove the concept, but it can be readily replaced by a multi-transistor output stage of a digital circuit. The dynamic output

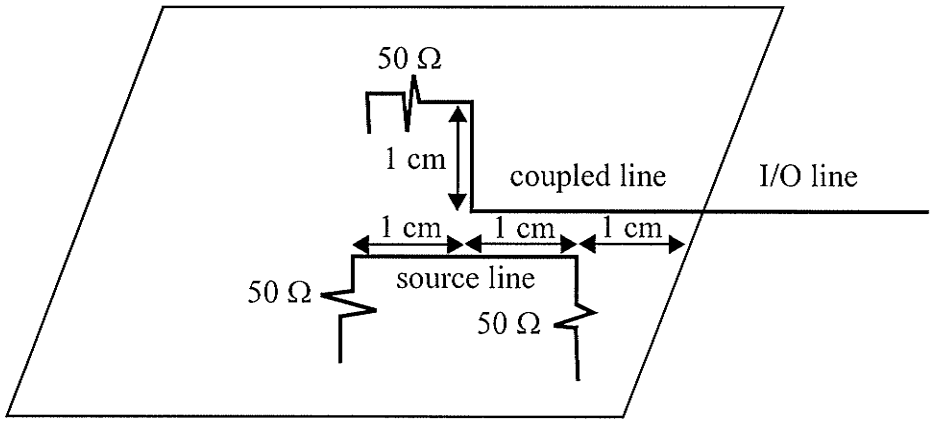

Figure 6.8 Coupled transmission lines with an attached I/O line.

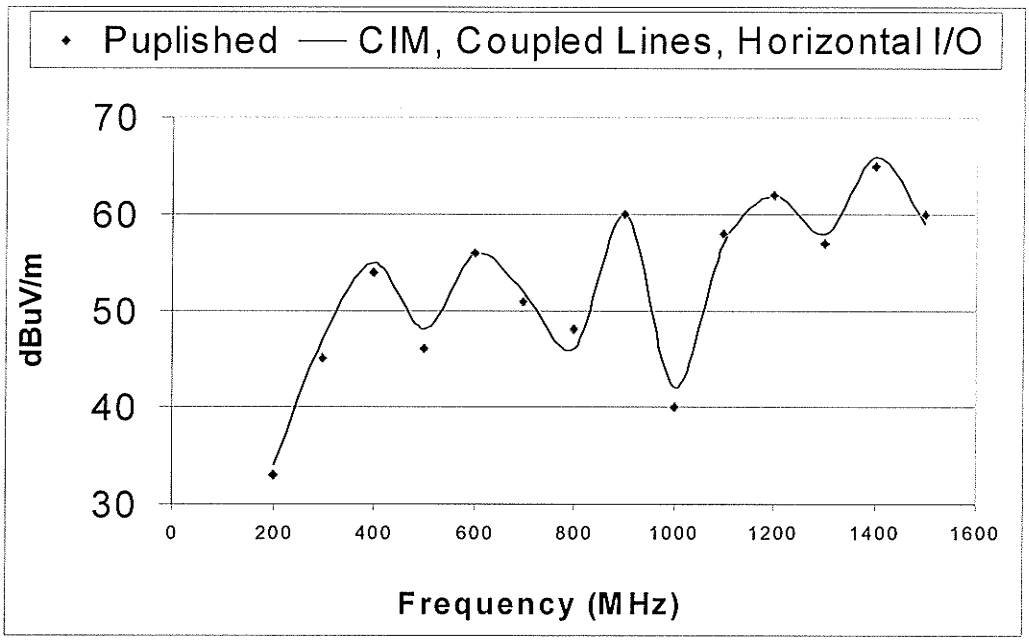

Figure 6.9 Magnitude of the electric field plotted as worst case vs. frequency.

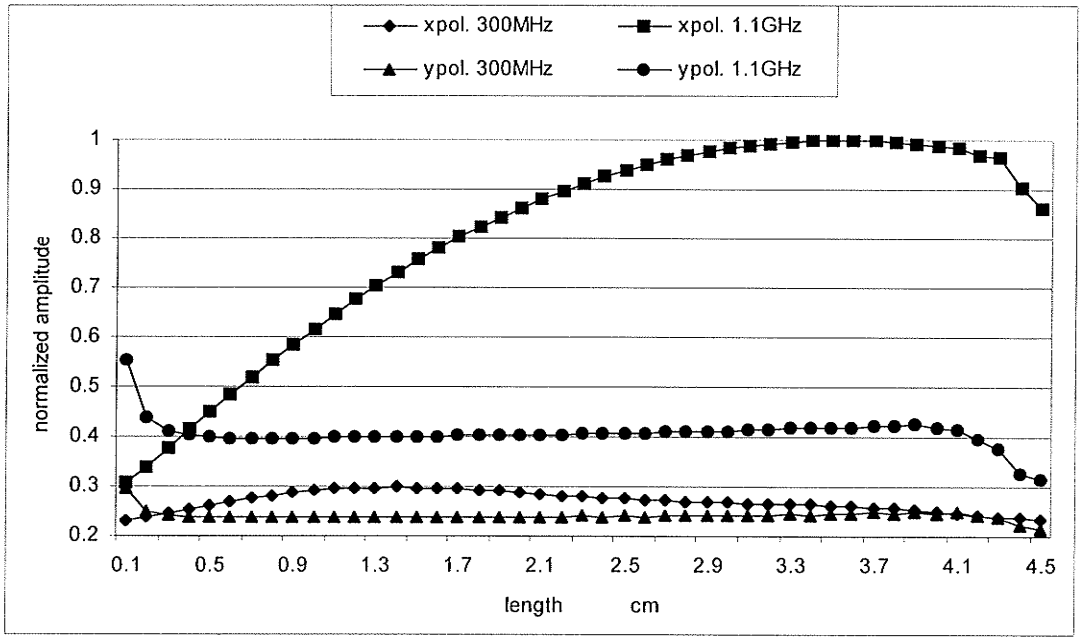

Figure 6.10 Induced currents on arm A of the T-junction.

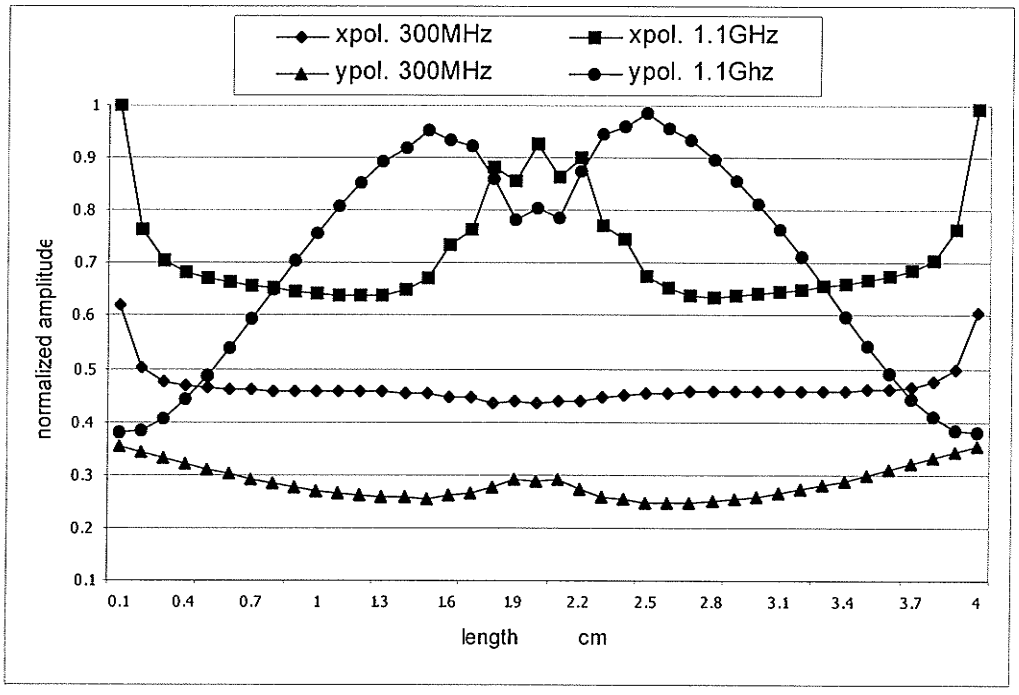

Figure 6.11 Induced currents on arm B of the T-junction.

impedance of the buffer is simplified to a 50ohms source impedance and the load is another simple 50ohms resistor. The input waveform is a trapezoidal waveform with 40ps rise and fall times, 320ps pulse repetition rate and a zero to one volt swing. The simulations are carried out in Eldo. The resulting waveforms from the simulations are plotted in Fig. 6.13. The two waveforms appear very similar to each other for the first look. One might consider that the gap in the ground plane is not affecting the digital signal.

The gap in the ground plane is 20mil wide, i.e., it is a small fraction of the wavelength at the maximum wavelength considered in the simulation. It is about one tenth of the dielectric wavelength at 8GHz. So indeed it is electrically small. However, a closer look at the waveform and the zoomed in section in Fig. 6.13 reveals that the waveform in the presence of the gap exhibits a non-monotonic edge. The non-monotonic edge can cause false trigger in the digital circuit. So even though the gap in the ground plane is electrically small it still affects the digital signal adversely to move it from a pass to a fail situation. The conclusion from this experiment is that the accuracy at which this signal is modeled using the MoM code is crucial to detecting such a hidden fault in the circuit.

6.5 Conclusion

The simulation results demonstrates the accuracy of the method as compared to published, computed and measured results. The solution technique is shown to be a valuable numerical analysis tool to predict radiated emissions levels from passive structures. In addition, the tool is used to assess the external field coupling to microstrip circuits, which is an instrumental step in the immunity analysis procedure as has been detailed in this chapter. The procedure for time domain signal integrity analysis for

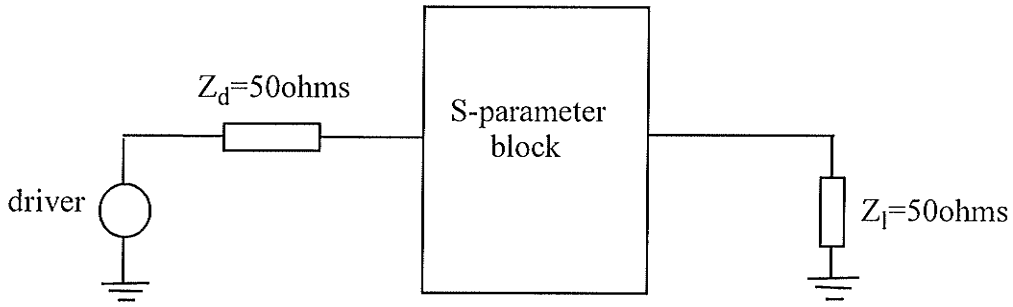

Figure 6.12 Circuit model for the double stub tuner circuit.

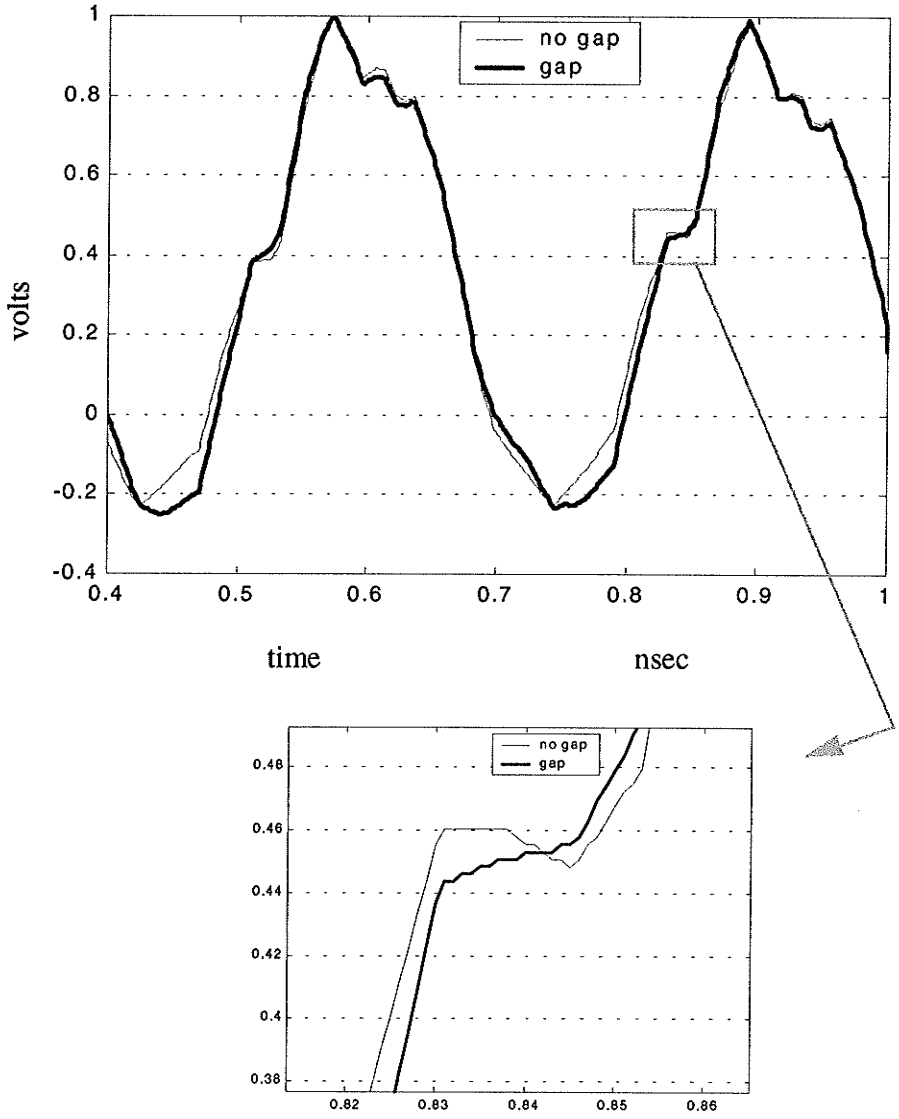

Figure 6.13 Time domain simulation results using the S-parameters for the double stub tuner circuit with and without a gap in the ground plane.

interconnect systems is presented and implemented. It is shown that modeling the interconnect system using the MoM and using its S-parameter description to carry out signal integrity simulations provides a deeper insight into the overall digital system performance.

CHAPTER 7

Conclusions and Future Work

7.1 Thesis Summary

This thesis presents the application of the CIM to the analysis of a wide variety of printed geometries in multilayered media. The CIM method is used to derive closed form Green's function in the spatial domain, hence avoiding the numerical evaluation of the Sommerfeld integrals. The original CIM is presented and its modification to the two level approach is discussed. The role of the quasi static part in the approximation process is pointed out and the importance of including its terms in the overall accuracy of the solution is demonstrated. The different approaches used to accommodate the presence of vertical conductors in the geometry are discussed. A new approach is suggested to retain the efficiency of the method. This approach allows for the seamless integration of arbitrary lengths of vertical conductors in the printed geometries.

The method is applied to several printed circuit geometries, and the reported results are in good agreement with other commercial software and published results. The method retains the advantage of being efficient. The technique also proved its potential as a valuable analysis tool for passive MMIC components, and as an EMC prediction tool.

The approach suggested here for calculating the Green's functions is a combination

of the two-level approach and the subtraction of the quasi-static images. The efficiency of this approach was demonstrated via a numerical example.

The integration of the MPIE with the MoM, combined with the usage of the CIM resulted in a versatile analysis tool for microstrip structures. The developed tool has the versatility to handle complex multilayer geometries, integrated with various feeding techniques. Line feeding, probe feeding, and aperture coupling are all included and tested for accuracy. The tested structures are of varying degree of complexity, and the obtained results are in good agreement with the commercial CAD software.

The numerical accuracy of the developed numerical technique is established against an accurate, analytical benchmark. In addition, it is shown that the error levels can be reduced to an arbitrary small level using the proper segmentations. This also demonstrates the stability of the method and its convergence. Examples of the applications to MMICs and microwave circuits further demonstrated the method's versatility and accuracy for the S-parameters extraction routines.

In the field of EMI, the method used in this thesis is applied with success to examples of different microstrip geometries and used in predicting the emissions levels from these circuits. A procedure for immunity analysis for PCBs is suggested in this research. This procedure makes the analysis for such problems efficient and reduces the redundancies associated with immunity testing and simulations. The efficiency of the MoM is particularly utilized in its ability to calculate the system response to multiple excitations without the need to re-compute the inverse of the impedance matrix.

Repeating the solution process at each frequency point of interest is always a part of the analysis process for antenna design, microwave circuit analysis or EMI analysis.

Enhancing the efficiency of the frequency sweeps using interpolation for the complex coefficients of the Green's functions enhances considerably the numerical efficiency of the analysis tool.

In combination with time domain convolution, The tool is used to analyze interconnect systems with active circuits in the time domain. Time domain convolution enables the combination of the analysis of complex active circuits and complex interconnect systems without sacrificing accuracy on either side.

7.1.1 Thesis Highlights

The thesis highlights may be summarized in the following points:

- The CIM is utilized as an accurate and efficient alternative to the numerical integration of the SIs in the analysis of printed geometries in multilayer dielectric media.
- A new approach is suggested to handle arbitrary length vertical conductors in multilayered media.
- The CIM is combined with the MPIE and the MoM to produce a versatile numerical analysis tool for printed geometries in multilayered media.
- The analysis tool is applied successfully to the analysis of multilayer antenna problems using different feeding mechanisms.
- The numerical accuracy and convergence of the tool is established via an analytical benchmark.
- The tool is applied to the analysis of microwave circuits, in the presence of finite ground planes, slots in the ground plane and to a wide frequency band interconnects.

- The tool is used to accurately predict the radiated emissions levels from printed interconnect structures.
- The frequency sweeps is made more efficient by interpolating the coefficients of the complex images used to represent the Green's functions in the spatial domain.
- An efficient susceptibility prediction procedure is suggested based on the analysis tool.
- In combination with time domain convolution, the tool is used to analyze interconnect systems with active circuits in the time domain.

7.2 The Efficiency of the Method

A basic measure for the efficiency of the CIM is the number of times the Green's functions expressions in the spectral domain are evaluated. The rational behind using that measure is the fact that the expressions for these functions are very complex as evident from Appendix A. The complexity rises with the increased number of dielectric layers. For a typical application of the CIM 200-500 samples are needed for the approximation, and this number does not depend on the size of the structure being analyzed. Once the complex coefficients are obtained using the GPOF method, the resulting simple closed form can be evaluated as many times as needed in the MoM solution. On the other hand for the direct numerical integration, the Green's function is typically evaluated thousands of times during the MoM solution, and the number increases with the size of the structure being analyzed. Hence, the CIM method is much more efficient in filling the MoM matrix than the direct numerical integration.

The resulting impedance matrix is identical in both cases (within the numerical

accuracy of the methods). The size of the impedance matrix is directly related to the size of the structure itself. And the solution process for the matrix equation does not depend on the approach used to obtain the Green's function in the spatial domain. Hence any comparison between the efficiency of the two MoM codes should distinguish between filling the impedance matrix and solving the matrix equation. The CIM based code can make use of all available efficient matrix solution techniques.

The overall efficiency achieved using the CIM is governed by the size of the analyzed structure, and its geometry. Our tool compared favorably with the commercial CAD tool IE3D [103] from the running-time point of view, for the same structure running on the same machine. This is specially evident for structures with vertical connections. The CAD tool uses direct numerical integration for the sommerfeld integrals, with acceleration and interpolation techniques.

However, as the structures become more complex and the MoM matrix gets larger, the computation time is longer than the matrix filling time and the extra numerical efficiency drops.

7.3 Future Work

Future work will include the use of variable size meshing techniques in the MoM segmentation. It may also elaborate on the susceptibility modeling procedure and its usage in different examples and actual circuit. Future work may also include a detailed investigation of using the MoM code in conjunction with the time domain convolution. Specifically, what frequency band should be employed in the analysis of interconnect structures. Together with a study of the required frequency step and the maximum

corresponding time domain step for the convolution. The investigation may also include a study of the limitations, if any, on the size of interconnect structures that can be analyzed using this method.

APPENDEX A

Green's Functions Derivation

For a general multilayer medium with magnetic and electric sources, there are 10 different types of potential functions [89], [130]. Table A.1 lists these potential functions.

Table A.1: Potential functions for different kinds of sources

VED	$\mathbf{G}_A^{zz}$	G_q^{ez}		
VMD			$\mathbf{G}_F^{zz}$	G_q^{mz}
HED	$\mathbf{G}_A^{xx}$, $\mathbf{G}_A^{zx}$	G_q^{ex}		
HMD			$\mathbf{G}_F^{xx}$, $\mathbf{G}_F^{zx}$	G_q^{mx}

V=vertical H=horizontal E=electric M=magnetic

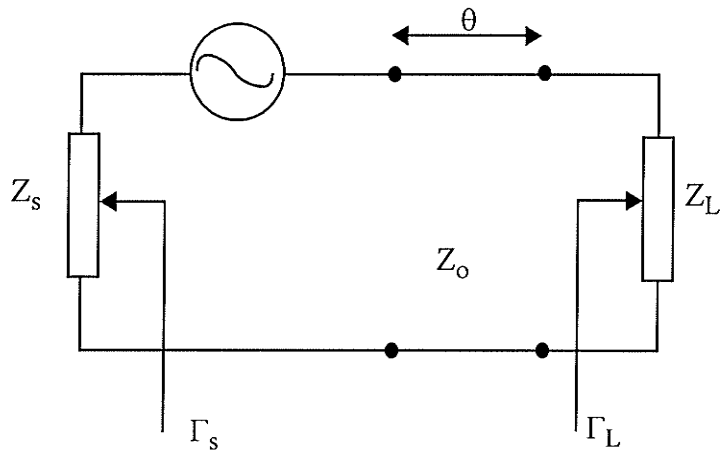

Figure A.1 A one section transmission line

For a simple one section transmission line model as shown in Fig. A.1, the voltage transfer at the load can be written as:

$$V_L = \frac{V_s}{2}\frac{(1-\Gamma_s)(1+\Gamma_L)e^{-jkd}}{1-\Gamma_s\Gamma_L e^{-2jkd}} \tag{A.1}$$

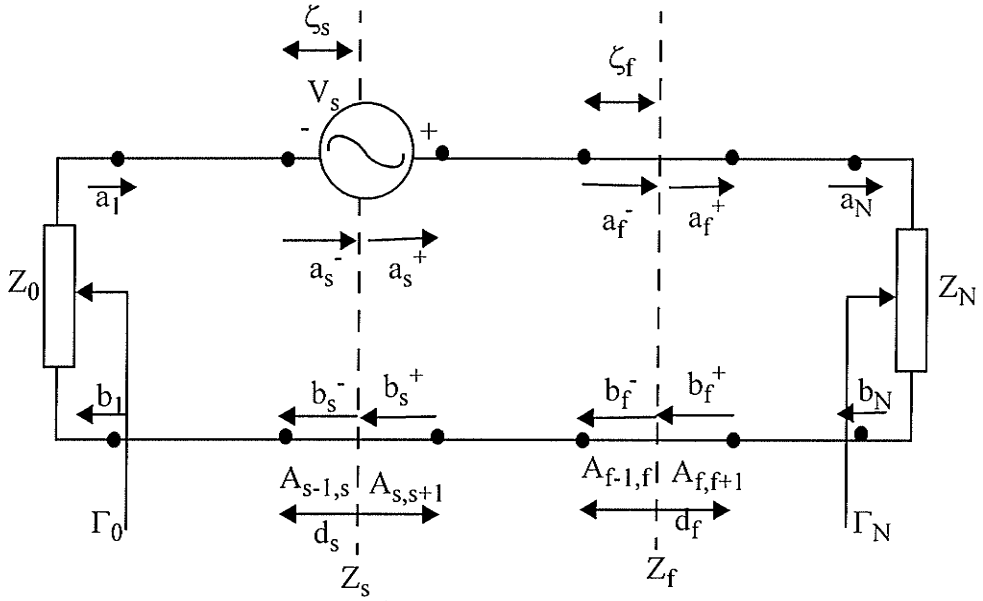

Figure A.2 Cascaded transmission line model.

In equation (A.1), the denominator can be written as:

$$\mathbf{P} = \frac{1-\Gamma_s\Gamma_L e^{-2jkd}}{e^{-jkd}} = \begin{pmatrix} 1 \\ -\Gamma_s \end{pmatrix}^T \mathbf{C} \begin{pmatrix} 1 \\ \Gamma_L \end{pmatrix} \tag{A.2}$$

where C is the transmission matrix of the transmission line:

$$\mathbf{C} = \begin{bmatrix} e^{jkd} & 0 \\ 0 & e^{-jkd} \end{bmatrix} \tag{A.3}$$

The matrix **C** in equation (A.3) simply becomes a chain product of a series of **C**'s. Thus equation (A.1) becomes a voltage transfer coefficient T of the form:

$$T = \frac{V(zf)}{V_s/2} = \frac{V_L}{V_s/2} = \frac{c_s(1-\Gamma_s)(1+\Gamma_L)c_L}{\mathbf{P}} \tag{A.4}$$

where the denominator **P** is given by:

$$\mathbf{P} = \begin{bmatrix} 1 \\ -\Gamma_o \end{bmatrix}^T \mathbf{C}_1\mathbf{C}_{12}\mathbf{C}_2\ldots\mathbf{C}_{s-}\,\mathbf{C}_{s+}\ldots\mathbf{C}_{f-}\,\mathbf{C}_{f+}\ldots\mathbf{C}_{N-1}\mathbf{C}_{N-1,N}\mathbf{C}_N \begin{bmatrix} 1 \\ \Gamma_N \end{bmatrix} \tag{A.5}$$

with

$$c_s \begin{bmatrix} 1 \\ -\Gamma_s \end{bmatrix}^T = \begin{bmatrix} 1 \\ -\Gamma_o \end{bmatrix}^T \mathbf{C}_1\mathbf{C}_{12}\mathbf{C}_2\ldots\mathbf{C}_{s-} \tag{A.6}$$

and

$$c_L \begin{bmatrix} 1 \\ \Gamma_L \end{bmatrix}^T = \mathbf{C}_{f+}\,\mathbf{C}_{f,f+1}\ldots\mathbf{C}_N \begin{bmatrix} 1 \\ \Gamma_N \end{bmatrix} \tag{A.7}$$

where $\mathbf{C}_n$ is defined as equation (A.3) with kd replaced by $k_{zn}d_n$. k_{zn} is given in terms of the propagation coefficient of the n^{th} medium k_n as: $k_{zn}^2 = k_n^2 - k_\rho^2$ and the radial spectral domain variable is k_ρ given by: $k_\rho = \sqrt{k_x^2 + k_y^2}$. $\mathbf{C}_{n,n+1}$ is the transmission matrix at the interface between lines Z_n and Z_{n+1} and has the form:

$$C_{n,n+1} = \frac{1}{\Upsilon_{n,n+1}+1} \begin{bmatrix} 1 & \Upsilon_{n,n+1} \\ \Upsilon_{n,n+1} & 1 \end{bmatrix} \tag{A.8}$$

where

$$\Upsilon_{n,\,n+1} = \frac{Z_{n+1} - Z_n}{Z_{n+1} + Z_n} \tag{A.9}$$

The transmission matrices $\mathbf{C}_{s\pm}$, $\mathbf{C}_{f\pm}$ are defined using equation (A.3) and replacing kd by $k_{zi}(d_i - \varsigma_i)$ and $k_{zi}\varsigma_i$ (i=s, f) for the + and - cases, respectively. $\varsigma_i(i = s, f)$ are distances of the sources and the field points from the first left interface, respectively, and $d_i(i = s, f)$ are the thicknesses of the layers in which the source and the field points are located.

A.1 Electric Sources

In a homogeneous medium the electromagnetic fields can be written in terms of the magnetic vector potential **A**. For an electric source of the form:

$$\mathbf{J} = I_o dl\delta(r - r_s)\hat{u}_I \tag{A.10}$$

located at r_s pointing at a unit direction $\hat{u}_I$ and radiating in a homogeneous space (μ_s,ε_s). A is given by:

$$\mathbf{A}_s = I_o\mu_s \frac{\exp(-jk_s|r - r_s|)}{4\pi|r - r_s|}\hat{u}_I \tag{A.11}$$

where $k_s^2 = \omega^2\mu_s\varepsilon_s$. The potential $\mathbf{A}_s$ may be represented in terms of the plane wave spectrum:

$$\mathbf{A}_s(r_s, r_f) = \frac{I_o \hat{u}_I}{4\pi^2} \int_{-\infty}^{\infty} \int_{-\infty}^{\infty} \tilde{A}_s(z_f, z_s, k_\rho) \exp(-jk_\rho \cdot \underline{\rho}) d_2 k_\rho \tag{A.12}$$

where (r_s, r_f) are the source and the field locations, $\underline{\rho} = (x_f - x_s)\hat{x} + (y_f - y_s)\hat{y}$, $\mathbf{k}_\rho = k_x \hat{x} + k_y \hat{y}$, and

$$\tilde{A}_s = \frac{\mu_s}{2jk_{zs}} \exp(-jk_{zs}|z_f - z_s|) \tag{A.13}$$

where $k_{zs} = \sqrt{k_s^2 - k_\rho^2}$, $\mathrm{Im}(k_{zs}) \le 0$. To prepare for the multilayer media, the spectral domain function $\tilde{A}_s$ in equation (A.13) can be written as:

$$\tilde{A}_s = \tilde{A}_{sO} T_{sO}(z_s, z_f; k_\rho) \tag{A.14}$$

$$\tilde{A}_{sO} = \frac{\mu_s}{2jk_{zs}} \tag{A.15}$$

$$T_{sO}(z_s, z_f; k_\rho) = \exp(-jk_{zs}|z_f - z_s|) \tag{A.16}$$

where $\tilde{A}_{sO}$ is the source spectral amplitude and T_{sO} is a propagation factor between the source and observation point in spectral $\mathbf{k}_\rho$ domain.

In a multilayer medium, the magnetic vector potential due to vertical electric-current element of unit intensity is assumed to have only one component $\mathbf{G}_A^{zz}$ along the z axis. For a horizontal electric source, there are two components: $\mathbf{G}_A^{xx}$ and $\mathbf{G}_A^{zx}$.

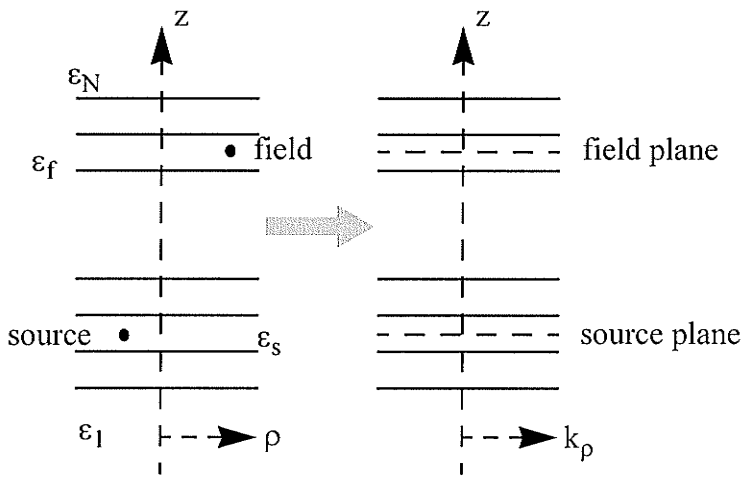

Figure A.3 Multilayer medium, spatial domain (left) and spectral domain (right).

A.1.1 Vertical Electric Dipole (VED)

The source current density is given by equation (A.10) with $\hat{u}_I = \hat{z}$. The spectral domain $\tilde{\mathbf{H}}_x$ is given by:

$$\tilde{\mathbf{H}}_x = \frac{-jk_y}{\mu_f}\tilde{\mathbf{G}}_A^{zz}(z_f, z_s; k_\rho) \tag{A.17}$$

Substituting equation (A.14) in the above equation:

$$\tilde{\mathbf{H}}_x = \tilde{H}_{xO} T_{TM}^{V,e}(z_f, z_s; k_\rho) \tag{A.18}$$

where the transfer function $T_{TM}^{V,e}$ is the propagation factor to be derived for a TM planer wave in a VED in the multilayer medium of Fig. A.3. $\tilde{H}_{xO}$ is the spectral amplitude of $\tilde{\mathbf{H}}_x$

at the source and can be given as:

$$\tilde{H}_{xO} = \frac{-jk_y}{\mu_s}\tilde{A}_{sO} \tag{A.19}$$

The analogy between the propagation of $\tilde{\mathbf{H}}_x$ and the wave behavior of the electric current on a multisection transmission line is used to determine $T_{TM}^{V,e}$. Because of the continuity of $\tilde{\mathbf{H}}_x$ at the plane of source, the source in the transmission-line model is chosen as a voltage source and its value is determined so that it can produce current $\tilde{H}_{xO}$ in the line when the line is ended by an impedance of source layer Z_s from both sides. Thus $T_{TM}^{V,e}$ can be written as:

$$T_{TM}^{V,e}(z_f, z_s; k_\rho) = \frac{\tilde{\mathbf{H}}_x(z_f)}{\tilde{H}_{xO}} = \frac{I_{z_f}}{V_s/2Z_s} \tag{A.20}$$

For this case the characteristic impedance Z_n is TM_z wave impedance in layer n, and the current reflection coefficients should be used:

$$Z_n = \frac{k_{zn}}{\omega\varepsilon_n} \tag{A.21}$$

The current-voltage transmission ratio of equation (A.20) can be written in terms of the transmission matrices of equations (A.3) and (A.8) as:

$$T_{TM}^{V,e} = \frac{c_s(1+\Gamma_s)(1+\Gamma_L)c_L}{\mathbf{P}} \tag{A.22}$$

where the parameter **P** is defined in equation (A.5).

Using equation (A.18), the following expression for $\tilde{\mathbf{G}}_A^{zz}$ at the field-observation point can be derived in terms of its source spectral amplitude:

$$\tilde{\mathbf{G}}_A^{zz}(z_f, z_s; k_\rho) = \tilde{A}_{sO}\frac{\mu_f}{\mu_s}T_{TM}^{V,e}(z_f, z_s; k_\rho) \tag{A.23}$$

The scalar potential $\tilde{G}_q^{ez}$ can be written as:

$$\tilde{G}_q^{ez} = \frac{\tilde{A}_{sO}}{\mu_s k_{z_s}^2 \varepsilon_f}\frac{\partial^2 T_{TM}^{V,e}}{\partial\varsigma_s \partial\varsigma_f} \tag{A.24}$$

where ς_i, i = s, f are distances shown in Fig. A.2.

A.1.2 Horizontal Electric Dipole (HED):

The source current density is given by equation (A.10) with $\hat{u}_I = \hat{x}$. For TE waves, this part is generated by the $\tilde{\mathbf{H}}_z$ of the incident field. Similar to equation (A.18):

$$\tilde{\mathbf{E}}_x = \tilde{E}_{xO}T_{TE}^{H,e}(z_f, z_s; k_\rho) \tag{A.25}$$

where the transfer function $T_{TE}^{H,e}$ is the propagation factor generated by a HED in the multilayer medium. $\tilde{E}_{xO}$ can be written as:

$$\tilde{E}_{xO} = jk_y\frac{j\omega\mu_s}{k_\rho^2}\tilde{H}_{zO} = -j\omega\frac{k_y^2}{k_\rho^2}\tilde{A}_{sO} \tag{A.26}$$

where $\tilde{A}_{sO}$ is given by equation (A.15). In the transmission-line model of Fig. A.2. $\tilde{\mathbf{E}}_x$ is

similar to voltage and, as it is continuous at the plane of source, the source is chosen as a current source. Based on the same argument as that used for VED $T_{TE}^{H,e}$ can be represented by the following ratio:

$$T_{TE}^{H,e} = \frac{\tilde{\mathbf{E}}_x(z_f)}{\tilde{E}_{xO}} = \frac{V(z_f)}{Z_s I_s/2} \tag{A.27}$$

which is readily been given by equation (A.22) for cascaded transmission-line sections when the series-voltage source V_s is replaced by parallel-current source I_s and the characteristic impedances in equation (A.9) are replaced by their TE equivalents:

$$Z_n = \frac{\omega \mu_n}{k_{zn}} \tag{A.28}$$

The following expression for $\tilde{\mathbf{G}}_A^{xx}$ can be written in terms of $T_{TE}^{H,e}$:

$$\tilde{\mathbf{G}}_A^{xx}(z_f, z_s; k_\rho) = \tilde{A}_{sO} T_{TE}^{H,e}(z_f, z_s; k_\rho) \tag{A.29}$$

TM waves are generated by $\tilde{\mathbf{E}}_z$ component of the incident field and thus:

$$\tilde{\mathbf{H}}_x(z_f, z_s; k_\rho) = \tilde{H}_{xO} T_{TM}^{H,e}(z_f, z_s; k_\rho) \tag{A.30}$$

where the transfer function $T_{TM}^{H,e}$ is the propagation factor for a TM constituent of HED in the multilayer medium. $\tilde{H}_{xO}$ is the spectral amplitude of $\tilde{\mathbf{H}}_x$ at the source if the source was to radiate in a homogeneous medium with parameters (μ_s, ε_s) and can be given as:

$$\tilde{H}_{xO} = \frac{-jk_x k_y k_{zs}}{\mu_s k_\rho^2} \tilde{A}_{sO} \tag{A.31}$$

where $\tilde{A}_{sO}$ is given by equation (A.15). The source in the transmission-line model is chosen as a current source due to the discontinuity of $\tilde{\mathbf{H}}_x$ at the plane of source. Thus $T_{TM}^{H,e}$ can be written as:

$$T_{TM}^{H,e}(z_f, z_s; k_\rho) = \frac{\tilde{\mathbf{H}}_x(z_f)}{\tilde{H}_{xO}} = \frac{I(z_f)}{I_s/2} \tag{A.32}$$

The current-voltage transmission $T_{TM}^{H,e}$ can be written as:

$$T_{TM}^{H,e} = \frac{c_s(1-\Gamma_s)(1+\Gamma_L)c_L}{\mathbf{P}} \tag{A.33}$$

where the parameter **P** is defined in equation (A.5). $\tilde{\mathbf{E}}_z$ can be written as:

$$\tilde{\mathbf{E}}_z = -\frac{k_x k_{zs}}{j\mu_s \omega \varepsilon_f} \tilde{A}_{sO} T_{TM}^{H,e}(z_f, z_s; k_\rho) \tag{A.34}$$

Using equations (A.29) and (A.34), the following expression for $\tilde{\mathbf{G}}_A^{zx}$ can be derived:

$$\tilde{\mathbf{G}}_A^{zx}(z_f, z_s; k_\rho) = \left(\frac{-k_x}{k_\rho^2}\right) \tilde{A}_{sO} \left(\frac{\mu_f}{\mu_s} k_{zs} T_{TM}^{H,e} - j\frac{\partial T_{TE}^{H,e}}{\partial \varsigma_f}\right) \tag{A.35}$$

The scalar potential $\tilde{G}_q^{ex}$ can be written as:

$$\tilde{G}_q^{ex} = \frac{\tilde{A}_{sO}}{\mu_s k_\rho^2 \varepsilon_f}\left(\frac{\mu_s k_f^2}{\mu_f} T_{TE}^{H,e} - jk_{zs}\frac{\partial T_{TM}^{H,e}}{\partial \varsigma_f}\right) \tag{A.36}$$

A.2 Magnetic Sources

The procedure that was used for an electric source can be used to find the potentials due to a magnetic current element or a magnetic charge point. For an magnetic dipole in a homogeneous medium of the form:

$$\mathbf{M} = m_o \delta(r_f - r_s)\hat{u}_m \tag{A.37}$$

The electric vector potential **F** is given by:

$$\mathbf{F}_s = m_o \frac{\exp(-jk_s|r - r_s|)}{4\pi|r - r_s|}\hat{u}_m \tag{A.38}$$

In the spectral domain function:

$$\tilde{\mathbf{F}}_s = \tilde{F}_{sO} T_{sO}(z_s, z_f; k_\rho) \tag{A.39}$$

$$\tilde{F}_{sO} = \frac{1}{2jk_{zs}} \tag{A.40}$$

$$T_{sO}(z_s, z_f; k_\rho) = \exp(-jk_{zs}|z_f - z_s|) \tag{A.41}$$

A.2.1 Vertical Magnetic Dipole (VMD)

The source current density is given by equation (A.37) with $\hat{u}_m = \hat{z}$. The generated

field by a VMD in a multilayer medium is TE_z and can be expressed in terms of a potential $\mathbf{G}_F^{zz}$ and a scalar potential G_q^{mz}. The field is generated by the $\tilde{\mathbf{H}}_z$ of the incident field. The transmission factor is derived as:

$$\tilde{\mathbf{E}}_x = \tilde{E}_{xO} T_{TE}^{V,m}(z_f, z_s; k_\rho) \tag{A.42}$$

Where the transfer function $T_{TE}^{V,m}$ is the propagation factor for the TE_z generated by a VMD in the multilayer medium. $\tilde{E}_{xO}$ can be written as:

$$\tilde{E}_{xO} = jk_y \frac{j\omega\mu_s}{k_\rho^2} \tilde{H}_{zO} = jk_y \tilde{F}_{sO} \tag{A.43}$$

Where $\tilde{F}_{sO}$ is given by equation (A.40). Using the transmission-line model of Fig. A.2 and the same argument for the dielectric dipole, $T_{TE}^{V,m}$ can be represented by the following ratio:

$$T_{TE}^{V,m} = \frac{\tilde{\mathbf{E}}_x(z_f)}{\tilde{E}_{xO}} = \frac{V(z_f)}{Z_s I_s/2} \tag{A.44}$$

$T_{TE}^{V,m}$ has the same form as $T_{TE}^{H,e}$. The following expressions for $\tilde{\mathbf{G}}_F^{zz}$ and $\tilde{G}_q^{mz}$ at the field-observation point can be derived in terms of its source spectral amplitude:

$$\tilde{\mathbf{G}}_F^{zz}(z_f, z_s; k_\rho) = \tilde{F}_{sO} T_{TE}^{H,e}(z_f, z_s; k_\rho) \tag{A.45}$$

$$\tilde{G}_q^{mz} = \frac{\tilde{F}_{sO}}{\mu_f k_{z_s}^2} \frac{\partial^2 T_{TE}^{H,e}}{\partial\varsigma_s \partial\varsigma_f} \tag{A.46}$$

Where ς_i, $i = s, f$ are distances shown in Fig. A.2.

A.2.2 Horizontal Magnetic Dipole (HMD)

The source current density is given by equation (A.37) with $\hat{u}_m = \hat{x}$. The generated field by a HMD in a multilayer medium can be expressed in terms of $\mathbf{G}_F^{xx}$, $\mathbf{G}_F^{zx}$ and G_q^{mx}. TM waves are generated by the $\tilde{\mathbf{E}}_z$ component of the incident field and thus:

$$\tilde{\mathbf{H}}_x(z_f, z_s; k_\rho) = \tilde{H}_{xO} T_{TM}^{H,m}(z_f, z_s; k_\rho) \tag{A.47}$$

where the transfer function $T_{TM}^{H,m}$ is the propagation factor for a TM constituent of HMD in the multilayer medium. $\tilde{H}_{xO}$ is the spectral amplitude of $\tilde{\mathbf{H}}_x$ at the source and can be given as:

$$\tilde{H}_{xO} = -j\omega\varepsilon_s \frac{k_y^2}{k_\rho^2} \tilde{F}_{sO} \tag{A.48}$$

where $\tilde{F}_{sO}$ is given by equation (A.40). $T_{TM}^{H,m}$ can now be written as:

$$T_{TM}^{H,m}(z_f, z_s; k_\rho) = \frac{\tilde{\mathbf{H}}_x(z_f)}{\tilde{H}_{xO}} = \frac{I(z_f)}{V_s/2Z_s} \tag{A.49}$$

$T_{TM}^{H,m}$ has the same form as $T_{TM}^{V,e}$. $\tilde{\mathbf{G}}_F^{xx}$ can be represented as:

$$\tilde{\mathbf{G}}_F^{xx}(z_f, z_s; k_\rho) = \tilde{F}_{sO} \frac{\varepsilon_s}{\varepsilon_f} T_{TM}^{V,e} \tag{A.50}$$

TE waves are generated by the $\tilde{\mathbf{H}}_z$ of the incident field. Thus,

$$\tilde{\mathbf{E}}_x = \tilde{E}_{xO} T_{TE}^{H,m}(z_f, z_s; k_\rho) \tag{A.51}$$

where the transfer function $T_{TE}^{H,m}$ is the propagation factor generated by a HMD in the multilayer medium. $\tilde{E}_{xO}$ can be written as:

$$\tilde{E}_{xO} = \frac{-jk_x k_y k_{zs}}{k_\rho^2} \tilde{F}_{sO} \tag{A.52}$$

Using the transmission line model, $T_{TE}^{H,m}$ can be written as:

$$T_{TE}^{H,m} = \frac{\tilde{\mathbf{E}}_x(z_f)}{\tilde{E}_{xO}} = \frac{V(z_f)}{V_s/2} = \frac{c_s(1-\Gamma_s)(1+\Gamma_L)c_L}{\mathbf{P}} \tag{A.53}$$

where the parameter **P** is defined in equation (A.5).

The following expression for $\tilde{\mathbf{G}}_F^{zx}$ can be derived:

$$\tilde{\mathbf{G}}_F^{zx}(z_f, z_s; k_\rho) = \frac{-k_x}{k_\rho^2} \tilde{F}_{sO} \left(k_{zs} T_{TE}^{H,m} - j \frac{\varepsilon_s}{\varepsilon_f} \frac{\partial T_{TM}^{V,e}}{\partial \varsigma_f} \right) \tag{A.54}$$

The scalar potential $\tilde{G}_q^{mx}$ can be written as:

$$\tilde{G}_q^{mx} = \frac{\tilde{F}_{sO}}{\mu_f k_\rho^2} \left(\frac{\varepsilon_s}{\varepsilon_f} k_f^2 T_{TM}^{V,e} - jk_{zs} \frac{\partial T_{TE}^{H,m}}{\partial \varsigma_f} \right) \tag{A.55}$$

Only four transfer functions have been used to obtain the potentials given in table1.

APPENDEX B

Surface Waves

On microstrip antennas, surface waves are excited whenever the substrate has a relative dielectric permittivity constant greater than one [131]. These surface waves give rise to coupling between various elements of an array and results also in end-fire radiation. Surface waves are launched in the substrate at an elevation angle θ lying between $\pi/2$ and $\text{asin}(1/\sqrt{\varepsilon_r})$ as shown in Fig. B.1. These waves are incident on the ground plane with this angle where they get reflected to the dielectric-air interface which also reflects them. Following this zigzag path, they finally reach the boundaries of the microstrip structure where they are reflected back and diffracted by the edges giving rise to end-fire radiation. On the way to the boundary, if there is any other antenna in the proximity, the surface waves can become coupled to it. This coupling decreases away from the point of excitation because the rate of decay of these surface waves is proportional to $1/(\sqrt{r})$.

Surface waves are TM and TE modes of the substrate. These modes are characterized by waves attenuating in the transverse direction and having a real propagation constant above the cutoff frequency. The phase velocity of the surface waves is highly dependent on the substrate thickness *h* and its relative dielectric permittivity ε_r. The lowest

order TM mode is designated as the TM_0 mode and has no cutoff frequency. The cutoff frequencies for the higher order TM_n and TE_n modes are given by:

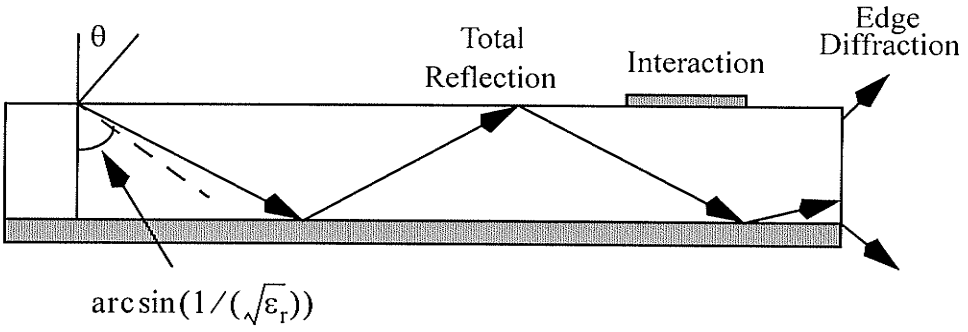

Figure B.1 Propagation of surface waves in the substrate of a microstrip structure.

$$f_c = \frac{nc}{4h\sqrt{\varepsilon_r - 1}} \tag{B.1}$$

where c is the velocity of light in free space, h is the substrate thickness and n = 1,3,5,... for TE_n modes and n = 0,2,4,... for TM_n modes. Having a zero cutoff frequency, the TM_o mode will always be excited at the open end of the microstrip antenna. It will even propagate on very thin substrates having low dielectric constant values at nearly the velocity of light. For the TE_1 mode, the calculated values of h/λ_c, where λ_c is the cutoff wavelength, are 0.217 and 0.072 for duroid ($\varepsilon_r = 2.32$) and GaAs ($\varepsilon_r = 13$) substrates, repectively.Thus, the lowest order TE mode is excited at about 41GHz for a 1.6mm thick duroid substrate and at about 109GHz for a 200μm thick GaAs substrate. The field distribution of the TE1 mode is such that it can propagate below the patch metallization and can always be excited above the cutoff frequency.

The dispersion relation for the TMn modes are given by:

$$\varepsilon_r u_0 h + uh\tanh(uh) = 0 \tag{B.2}$$

While for the TEn modes, the dispersion relation is given by:

$$u_0 h + uh\coth(uh) = 0 \tag{B.3}$$

where

$$u_0^2 = \beta^2 - k_0^2 \tag{B.4}$$

and

$$u^2 = \beta^2 - k_0^2 \varepsilon_r \tag{B.5}$$

The exact value of β has to be known for the analysis of microstrip antennas. This exact value is usually obtained using a root searching algorithm. Yet, the initial value of β is still needed in a closed form for the root searching. For the TM_o mode in lossless substrates, the radial propagation constant β is real and bounded by $1 < \beta/k_0 < \varepsilon_r$. If the substrate is electrically thin then $\beta/k_0 \approx 1$. The value of β/k_0 can be obtained by assuming:

$$\beta/k_0 \approx 1 + \delta \tag{B.6}$$

Substituting this expression in (B.2), we get

$$\varepsilon_r\sqrt{2\delta + \delta^2} - \sum_{n=0}^{\infty} \alpha_n \delta^n = 0 \tag{B.7}$$

where the infinite sum is a Taylor's series for $\sqrt{\varepsilon_r - z^2}\tan(k_0 h\sqrt{\varepsilon_r - z^2})$ around the point $z = \beta/k_0 = 1$. In (B.7)

$$\alpha_0 = s\tan(k_0 hs) \tag{B.8}$$

$$\alpha_1 = -\frac{1}{s}\left[\tan(k_0 hs) + \frac{k_0 hs}{(\cos(k_0 hs))^2}\right] \tag{B.9}$$

$$s = \sqrt{\varepsilon_r - 1} \tag{B.10}$$

Retaining only the dominant term α_0 in (B.7),

$$\beta/k_0 \approx 1 + \frac{1}{2}\left(\frac{\varepsilon_r - 1}{\varepsilon_r} k_0 h\right)^2 \tag{B.11}$$

While using a two term Taylor approximation in (B.7) yields

$$\beta/k_0 = 1 + \frac{\alpha_0\alpha_1 - \varepsilon_r^2 + \varepsilon_r\sqrt{\varepsilon_r^2 - 2\alpha_0\alpha_1 + \alpha_0^2}}{\varepsilon_r^2 - \alpha_1^2} \tag{B.12}$$

The above expression gives good accuracy for $sh < \lambda_o/4$. If the substrate has moderate losses defined as $\varepsilon_r(1 - j\tan\delta)$, then the surface wave propagation constant will also be complex valued defined as $\beta = (\beta_r - j\beta_i)$ with $\beta_i > 0$, where

$$\begin{aligned} \beta_r &= \beta \\ \beta_i &= (\varepsilon_r - 1)\tan\delta((k_0 h)/\varepsilon_r)^2 \end{aligned} \tag{B.13}$$

For a multilayer substrate consisting of *n* different thin layers, a general expression for β/k_0 for the TM_o mode can be given as:

$$\beta/k_0 = 1 + \frac{1}{2}\left(\sum_{i=1}^{N} \frac{\varepsilon_{ri} - 1}{\varepsilon_{ri}} k_0 h_i\right)^2 \tag{B.14}$$

where ε_{ri} and h_i are the constituent parameters of the i^{th} layer. For single layer thin

substrates, β_i/k_0 vary linearly with $\tan\delta$ and $k_0 h\sqrt{\varepsilon_r - 1}$.

The value of the substrate thickness that allows only the propagation of TM_o mode while keeping all other modes below cutoff is given for a single layer substrate as:

$$\frac{h}{\lambda_o} = \frac{1}{4\sqrt{\varepsilon_r - 1}} \tag{B.15}$$

For the double layer substrate case, the condition that should be satisfied is:

$$\tan(k_0 h_1\sqrt{\varepsilon_{r1} - 1})\tan(k_0 h_2\sqrt{\varepsilon_{r2} - 1}) \le \sqrt{\frac{\varepsilon_{r2} - 1}{\varepsilon_{r1} - 1}} \tag{B.16}$$

The power carried away by the surface wave increases with the increase in the substrate thickness. However, for thicknesses satisfying

$$\frac{h}{\lambda_o} = \frac{0.3}{2\pi\sqrt{\varepsilon_r}} \tag{B.17}$$

the antenna loss associated with the surface wave can be neglected. The radiation efficiency of the antenna decreases due to the power carried away by the surface waves. This decrease in efficiency can be used as a criterion in deciding the value of the substrate thickness for the patch.

REFERENCES

[1] R. S. Elliott, *Antenna Theory and Design*, Prentice Hall, Englewood Cliffs, NJ, 1981.

[2] R. Munson, "Conformal microstrip antennas and microstrip phased arrays," *IEEE Trans. Antennas Propagat.*, vol. AP-22, pp. 74-78, 1974.

[3] H. Pues and A. Van de Capelle, "Accurate transmission line model for the rectangular microstrip antenna," *IEE Proc.*, vol. 131, pp. 334-340, 1984.

[4] J. R. James and P. S. Hall, *Handbook of Microstrip Antennas.*, Peter Pereginus, London, U. K., 1989.

[5] E. Van Lil and A. Van de Capelle, "Transmission line model for mutual coupling between microstrip antennas," *IEEE Trans. Antennas Propagat.*, vol. AP-32, pp. 816-821, 1984.

[6] R. W. Dearnley and A. R. F. Barel, "A broad-band transmission line model for a rectangular microstrip antenna," *IEEE Trans. Antennas Propagat.*, vol. AP-37, pp. 6-15, 1989.

[7] A. K. Bhattacharyya and R. Garg, "Generalized transmission line model for microstrip patches," *IEE Proc.*, vol. 132, pp. 93-98, 1985.

[8] A. K. Bhattacharyya, "Generalized transmission line model of microstrip patch antennas and some applications," Ph.D. thesis, Indian Institute of Technology, Kharagpur, India, 1985.

[9] G. Dubsot and A. Rabbaa, "Analysis of a slot microstrip antenna," *IEEE Trans. Antennas Propagat.*, vol. AP-34, pp. 155-163, 1986.

[10] G. Dubost and A. Zerguerras, "Transmission-line model analysis of arbitrary shape symmetrical patch antenna coupled with a director," *Electron. Lett.*, vol. 26, pp. 952-954, 1990.

[11] Y. T. Lo and W.F. Richards, "Theory and experiment on microstrip antennas," *IEEE Trans. Antennas Propagat.*, vol. AP-27, pp. 137-145, 1979.

[12] V. Palanisamy and R. Garg, "Analysis of arbitrary shaped microstrip patch antennas using segmentation technique and cavity model," *IEEE Trans. Antennas Propagat.*, vol. AP-34, pp. 1208-1213, 1986.

[13] V. Palanisamy and R. Garg, "Rectangular ring and H-shaped microstrip antennas-alternatives to rectangular patch antenna," *Electron. Lett.*, vol. 21, pp. 874-876, 1985.

[14] V. Palanisamy and R. Garg, "Analysis of circularly polarized square ring and crossed-strip microstrip antennas," *IEEE Trans. Antennas Propagat.*, vol. AP-34, pp. 1340-1346, 1986.

[15] K. C. Gupta and A. Benalla, "Two-port transmission characteristics of circular microstrip patch antennas," *IEEE AP-S Int. Symp. Digest*, pp. 821-824, 1986.

[16] K. C. Gupta and P.C. Sharma, "Segmentation and desegmentation techniques for the analysis of two-dimensional microstrip antennas," *IEEE AP-S Int. Symp. Digest*, pp. 19-22, 1981.

[17] G. Kumar and K.C. Gupta, "Broadband microstrip antennas using additional resonators gap-coupled to radiating edges," *IEEE Trans. Antennas Propagat.*, vol. AP-32, pp. 1375-1379, 1984.

[18] R. P. Parrikar and K. C. Gupta, "Multiport network model for CAD of electromagnetically coupled patch antennas," *IEEE Trans. Microwave Theory Tech.*,

vol. MTT-46, pp. 475-483, 1998.

[19] P. C. Sharma and K. C. Gupta, "Analysis and optimized design of single feed circularly polarized microstrip antennas," *IEEE Trans. Antennas Propagat.*, vol. AP-31, pp. 949-955, 1983.

[20] G. Kumar and K.C. Gupta, "Directly coupled multiple resonator wideband microstrip antennas," *IEEE Trans. Antennas Propagat.*, vol. AP-33, pp. 588-593, 1985.

[21] A. Benalla and K. C. Gupta, "Multiport network model and transmission characteristics of two-port rectangular microstrip antennas," *IEEE Trans. Antennas Propagat.*, vol. AP-36, pp. 1337-1342, 1988.

[22] S. Akhtarzad and P.B. Johns, "Three-dimensional transmission-line matrix computer analysis of microstrip resonators," *IEEE Trans. Microwave Theory Tech.*, vol. MTT-23, pp. 990-997, 1975.

[23] A. Reineix and B. Jecko, "Analysis of microstrip patch antennas using finite difference time domain method," *IEEE Trans. Antennas Propagat.*, vol. AP-37, pp. 1361-1369, 1989.

[24] M. I. Sobhy, M. W. R. Ng, G. J. Langley and J. C. Batchelor, "TLM analysis of microstrip patch antenna on ferrite substrate," *IEEE Microwave Symp. Digest*, vol. 3, pp. 1297 -1300, 1999.

[25] S.Yang, I.G. Gosling, S. H. Tan and M. G. Sorwar, "TLM analysis of the mutual coupling of microstrip patch antenna arrays," *Microwaves Antennas and Propagat., IEE Proceedings* -, vol. 147, pp. 207 -210, 2000.

[26] T. Vlasits, E. Korolkiewicz and S. Sanbell, "Analysis of cross-aperture coupled patch antenna using transmission line model," *Electron. Lett.*, vol. 32, pp. 1934-1935, 1996.

[27] N. R. S. Simon, A. Sebak and A. Ittipiboon, "Analysis of aperture-coupled microstrip-antenna and circuit structures using the transmission-line-matrix method," *IEEE Antennas Propagat. Magazine*, vol. 37, pp. 27-37, 1995.

[28] D. M. Sheen, S. M. Ali, M. D. Abouzahra, and J. A. Kong, "Application of the three-dimensional finite-difference time-domain method to the analysis of planar microstrip circuits," *IEEE Trans. Microwave Theory Tech.*, vol. MTT-38, pp. 849-857, 1990.

[29] P. Leveque, A. Reineix, and B. Jecko, "Modelling dielectric losses in microstrip patch antennas: Application of FDTD method," *Electron. Lett.*, vol. 28, pp. 539-540, 1992.

[30] C. Wu, K.-L. Wu, Z.-Q. Bi, and J. Litva, "Accurate characterization of planar printed antennas using finite-difference time-domain method," *IEEE Trans. Antennas Propagat.*, vol. AP-40, pp. 526-533, 1992.

[31] K. Uehara and K. Kagoshima, "FDTD method analysis of mutual coupling between microstrip antennas," *IEICE Trans. Commun.*, vol. E76-B, pp. 762-764, 1993.

[32] T. Oonishi, T. Kashiwa, and I. Fukai, "Analysis of microstrip antennas on a curved surface using the conformal grids FD-TD method," *Electron. and Comm. in Japan*, Part 1 Comm., vol. 76, pp. 73-81, 1993.

[33] A. Reineix and B. Jecko, "A time domain theoretical method for the analysis of microstrip antennas composed by slots," *Annales des Télécommunications*, vol. 48, pp. 29-34, 1993.

[34] A. Reineix, J. Paillol, and B. Jecko, "FDTD method applied to the study of radar cross section of microstrip patch antennas," *Annales des Télécommunications*, vol. 48, pp. 589-593, 1993.

[35] A. Reineix, C. Melon, T. Monediere, and F. Jecko, "The FDTD method applied to the

study of microstrip patch antennas with a biased ferrite substrate," *Annales des Télécommunications*, vol. 49, pp. 137-142, 1994.

[36] R. F. Harrington, *Field Computation by Moment Methods*, Macmillan, 1968.

[37] T. K. Sarkar and E. Arvas, "An integral equation approach to the analysis of finite microstrip antennas: volume/surface formulation," *IEEE Trans. Antennas Propagat.*, vol. AP-38, pp. 305-312, 1990.

[38] A. Badawi and A. Sebak, "Analysis of microstrip antennas integrated with feed networks", *ANTEM96*, pp. 391-394, Montreal, 1996.

[39] E. Arbel and L. B. Felsen, "Theory of radiation from sources in anisotropic media, Part 1: General sources in stratified media," in *Electromagnetic Theory and Antennas, Part 1,* E. C. Jordan, Ed. NewYork: Macmillan, pp. 391–420, 1963.

[40] S. M. Ali and S. F. Mahmoud, "Electromagnetic fields of buried sources in stratified anisotropic media," *IEEE Trans. Antennas Propagat.,* vol. AP-27, pp. 671–678, 1979.

[41] J. K. Lee and J. A. Kong, "Dyadic Green's functions for layered anisotropic medium," *Electromagn.,* vol. 3, pp. 111–130, 1983.

[42] T. Sphicopoulos, V. Teodoridis, and F. E. Gardiol, "Dyadic Green function for the electromagnetic field in multilayered isotropic media: An operator approach," *IEE Proc.,* vol. 132, pt. H, pp. 329–334, 1985.

[43] J. S. Bagby, D. P. Nyquist, and B. C. Drachman, "Integral formulation for analysis of integrated dielectric waveguides," *IEEE Trans. Microwave Theory Tech.,* vol. MTT-33, pp. 906–915, 1985.

[44] D. H. S. Cheng, "On the formulation of the dyadic Green's function in a layered medium," *Electromagn.,* vol. 6, pp. 171–182, 1986.

[45] C. M. Krowne, "Determination of the Green's function in the spectral domain using a matrix method: Application to radiators immersed in a complex anisotropic layered medium," *IEEE Trans. Antennas Propagat.,* vol. AP-34, pp. 247–253, 1986.

[46] N. K. Das and D. M. Pozar, "A generalized spectral-domain Green's function for multilayer dielectric substrates with application to multi-layer transmission lines," *IEEE Trans. Microwave Theory Tech.,* vol. MTT-35, pp. 326–335, 1987.

[47] L. Beyne and D. De Zutter, "Green's function for layered lossy media with special application to microstrip antennas," *IEEE Trans. Microwave Theory Tech.,* vol. MTT-36, pp. 875–881, 1988.

[48] L. Vegni, R. Cicchetti, and P. Capece, "Spectral dyadic Green's function formulation for planar integrated structures," *IEEE Trans. Antennas Propagat.,* vol. AP-36, pp. 1057–1065, 1988.

[49] R. Kastner, E. Heyman, and A. Sabban, "Spectral domain iterative analysis of single- and double-layered microstrip antennas using the conjugate gradient algorithm," *IEEE Trans. Antennas Propagat.,* vol. AP-36, pp. 1204–1212, 1988.

[50] S. Barkeshli and P. H. Pathak, "On the dyadic Green's function for a planar multilayered dielectric/magnetic media," *IEEE Trans. Microwave Theory Tech.,* vol. MTT-40, pp. 128–142, 1992.

[51] S. G. Pan and I. Wolff, "Scalarization of dyadic spectral Green's functions and network formalism for three-dimensional full-wave analysis of planar lines and antennas," *IEEE Trans. Microwave Theory Tech.,* vol. MTT-42, pp. 2118–2127, 1994.

[52] A. Dreher, "A new approach to dyadic Green's function in spectral domain," *IEEE Trans. Antennas Propagat.,* vol. AP-43, pp. 1297–1302, 1995.

[53] W. C. Chew and Q. Liu, "Resonance frequency of a rectangular microstrip patch," *IEEE Trans. Antennas Propagat.*, vol. AP-36, pp. 1045–1056, 1988.

[54] T.-S. Horng, N. G. Alexopoulos, S.-C. Wu, and H.-Y. Yang, "Full-wave spectral analysis for open microstrip discontinuities of arbitrary shape including radiation and surface-wave losses," *Int. J. Microwave Millimeter-Wave Comput.-Aided Eng.*, vol. 2, pp. 224–240, 1992.

[55] T. Becks and I. Wolff, "Analysis of 3-D metallization structures by a full-wave spectral domain technique," *IEEE Trans. Microwave Theory Tech.*, vol. MTT-40, pp. 2219–2227, 1992.

[56] J. R. Mosig and F. E. Gardiol, "A dynamical radiation model for microstrip structures," in *Advances in Electronics and Electron Physics*, P. W. Hawkes, Ed. New York: Academic, vol. 59, pp. 139–237, 1982.

[57] J. R. Mosig and F. E. Gardiol, "Analytic and numerical techniques in the Green's function treatment of microstrip antennas and scatterers," *IEE Proc.*, vol. 130, pt. H, pp. 175–182, 1983.

[58] J. R. Mosig and F. E. Gardiol, "General integral equation formulation for microstrip antennas and scatterers," *IEE Proc.*, vol. 132, pt. H, pp. 424–432, 1985.

[59] R. C. Hall and J. R. Mosig, "The analysis of coaxially fed microstrip antennas with electrically thick substrates," *Electromagn.*, vol. 9, no. 4, pp. 367–384, 1989.

[60] D. Zheng and K. A. Michalski, "Analysis of arbitrarily shaped coax-fed microstrip antennas—A hybrid mixed-potential integral equation approach," *Microwave Opt. Tech. Lett.*, vol. 3, pp. 200–203, 1990.

[61] G. A. E. Vandenbosch and A. R. Van de Capelle, "Mixed-potential integral expression formulation of the electric field in a stratified dielectric medium—Application to the case of a probe current source," *IEEE Trans. Antennas Propagat.,* vol. AP-40, pp. 806–817, 1992.

[62] F. Alonso-Monferrer, A. A. Kishk, and A. W. Glisson, "Green's function analysis of planar circuits in a two-layer grounded medium," *IEEE Trans. Antennas Propagat.,* vol. AP-40, pp. 690–696, 1992.

[63] T. K. Sarkar, P. Midya, Z. A. Maricevic, M. Kahrizi, S. M. Rao, and A. R. Djordjevic, "Analysis of arbitrarily shaped microstrip patch antennas using the Sommerfeld formulation," *Int. J. Microwave Millimeter-Wave Comput.-Aided Eng.,* vol. 2, pp. 168–178, 1992.

[64] W. C. Chew, *Waves and Fields in Inhomogenous Media*, New York: Van Nostrand, 1990.

[65] P. B. Katehi and N. G. Alexopoulos, "Real axis integration of Sommerfeld integrals with applications to printed circuit antennas," *J. Math. Phys.*, vol. 24, 527-533, 1983.

[66] Y. Rahmat-Samii, R. Mittra, and P. Parhami, "Evaluation of Sommerfeld integrals for lossy half-space problems," *Electromagnetics*, vol. 1, 1-28, 1981.

[67] P. Gay-Balmaz and J. R. Mosig, "Three-dimensional planar radiating structure in stratified media," *Int. J. Microwave Millimeter-Wave CAE,* vol. 7., 330-343, 1997.

[68] J. R. Mosig and F. E. Gardiol, "Analytic and numerical techniques in the Green's function treatment of microstrip antennas and scatterers," *IEE Proc.*, pt. H, vol. 130, 175-182, 1983.

[69] K. A. Michalaski, "Extrapolation methods for Sommerfeld integral tails," *IEEE Trans.*

Antennas Propagat., vol. AP-46, pp. 1405-1418, 1998.

[70] D. M. Pozar, "Input impedance and mutual coupling of rectangular microstrip antennas," *IEEE Trans. Antennas Propagat.*, vol. AP-30, pp. 2-24, 1981.

[71] D. R. Jacson and N. G. Alexopoulos, "An asymptotic extraction technique for evaluating Sommerfeld-type integrals," *IEEE Trans. Antennas Propagat.*, vol. AP-34, pp. 1467-1470, 1986.

[72] S. Barkeshli and P. H. Pathak, "An asymptotic closed-form microstrip surface Green's function for the efficient moment method analysis of mutual coupling in microstrip antenna," *IEEE Trans. Antennas Propagat.*, vol. AP-38, pp. 1374-1383, 1990.

[73] M. J. Dunn, "A uniform asymptotic expansion for the Green's functions used in microstrip calculations," *IEEE Trans. Microwave Theory Tech.*, vol. MTT-39, pp.1223-1226, 1991.

[74] R. W. King, "Electromagnetic field of dipoles and patch antennas on microstrip," *Radio Science*, vol. 27, pp. 71-78, 1992.

[75] A. Hoorfar and D. C. Chang, "Closed form solutions to Green's functions in microstrip problems with a thin substrate," *Radio Science*, vol. 30, pp. 343-351, 1995.

[76] J. J. Yang, Y. L. Chow, G. E. Howard, and D. G. Fang, "Complex images of an electric dipole in homogeneous as layered dielectrics between two ground planes," *IEEE Trans. Microwave Theory Tech.*, vol. MTT-40, pp. 595-600, 1992.

[77] Y. L. Chow, J. J. Yang, D. G. Fang, and G. E. Howard, "A closed form spatial Green's functions for thick microstrip substrates," *IEEE Trans. Microwave Theory Tech.*, vol. MTT-39, pp. 588-593, 1991.

[78] Y. Hua and T. K. Sarkar, "Generalized pencil-of-function method for extracting poles

of an EM system from its transient response," *IEEE Trans. Antennas Propagat.*, vol. AP-37, pp. 229-234, 1989.

[79] M. I. Aksun, "A robust approach for the derivation of closed-form Green's functions," *IEEE Trans. Microwave Theory Tech.,* Vol. MTT-44, pp. 651-658, 1996.

[80] I. Park, R. Mittra, and M. I. Aksun, "Numerically efficient analysis of planar microstrip configurations using closed-form Green's functions," *IEEE Trans. Microwave Theory Tech.*, vol. MTT-43, pp.394-400, 1995.

[81] A. A. Omar, "Efficient full wave analysis of transition from microstrip to microstrip through an aperture," *Int. J. Microwave Millimeter-Wave CAE,* vol. 7, pp. 380-387, 1997.

[82] D. Yau and N. V. Shuley, "Numerical analysis of an aperture coupled microstrip patch antenna using mixed potential integral equation and complex images," *PIER 18*, pp. 229-244,1998.

[83] C. H. Chan and R. A. Kipp, "Application of the complex image method to multilevel, multiconductor microstrip lines," *Int. J. Microwave Millimeter-Wave CAE,* vol. 7., pp. 359-367, 1997.

[84] N. Kinayman and M. I. Aksun, "Efficient and accurate EM simulation technique for analysis and design of MMICs," *Int. J. Microwave Millimeter-Wave CAE*, vol. 7, pp. 344-358, 1997.

[85] R. M. Shubair and Y. L. Chow, "A Simple and accurate complex image interpretation of vertical antennas present in contiguous dielectric half-spaces," *IEEE Trans. Ant. Propagat.*, vol. AP-41, pp. 806-812, 1993.

[86] K. A. Michalski and J. R. Mosig, "Discrete complex image MPIE analysis of coax-fed

coupled vertical monopoles in a grounded dielectric substrate: two formulations," *IEE Proc.*, pt. H, vol. 142, pp. 269-274, 1995.

[87] G. Dural and M. I. Aksun, "Closed form Greens function for general sources and stratified media," *IEEE Trans. Microwave Theory Tech.*, vol. MTT-43, pp. 1545-1552, 1995.

[88] C. H. Chan and R. A. Kipp, "Complex image method for sources in bounded regions of multilayer structures," *IEEE Trans. Microwave Theory Tech.*, vol. MTT-42, pp. 860-865, 1994.

[89] K. A. Michalski and J. R. Mosig, "Multilayered media Green's functions in integral equation formulations," *IEEE Trans. Antennas Propagat.*, vol. AP-45, pp.508-519, 1997.

[90] A. A. Omar and Y. L. Chow, "A Solution of coplanar waveguide and air-bridges using complex images," *IEEE Trans. Microwave Theory Tech.*, vol. MTT-40, pp. 2070-2077, 1992.

[91] A. Badawi and A. Sebak, "Analysis of stacked microstrip patch antennas using closed form Green's function" URSI meeting Montreal, pp. 104, 1997.

[92] J. M. Laheurte, M. Rousta and S. Marchetti, "Improved frequency domain analysis of microstrip circuits by the method of moments", *IEE Proc.*, pt. H, vol. 142, pp. 421-428, 1995.

[93] R. C. Hall, and J. R. Mosig, "The analysis of arbitrarily shaped aperture-coupled patch antenna via a mixed potential integral equation" *IEEE Trans. Antennas Propagat.*, vol. AP-44, pp. 608-614, 1996.

[94] N. Hojjat, S. Safavi-Naeini and Y. L. Chow, "Numerical Computation of complex

image Green's functions for multilayer dielectric media: near-field zone and the interface region," *IEE Proc.*, pt. H, vol. 145, pp. 449-454, 1998.

[95] D. Yau and N. V. Shuley, "Numerical analysis of an aperture coupled rectangular dielectric resonator antenna using a surface formulation and the method of moments," *IEE Proc.*, pt. H, vol. pp. 146, 105-110, 1999.

[96] R. F. Harrington, *Time-Harmonic Electromagnetic Field,* McGraw-Hill, New York, 1961.

[97] C. H. Chan and R. A. Kipp, "Application of the complex image method to microstrip vias," *Int. J. Microwave Millimeter-Wave CAE*, vol. 7, pp. 368-379, 1997.

[98] I. S. Gradshteyn and I. M. Ryzhik, *Tables of Integrals, Series, and Products*, Academic Press, New York, 1965.

[99] N. Hojjat, S. Safavi-Naeini, R. Faraji-Dana and Y. L. Chow, "Fast computation of the nonsymmetrical components of the Green's function for multilayer media using complex images," *IEE Proc.*, pt. H, vol. 145, pp. 285-288, 1998.

[100] M. I. Aksun and R. Mittra, "Choices of expansion and testing functions for the method of moments applied to a class of electromagnetic problems," *IEEE Trans. Microwave Theory Tech.*, vol. MTT-41, pp. 503-509, 1993.

[101] R. A. York, R. C. Compton and B. J. Rubin, "Experimental verification of the 2-D rooftop approach for modeling microstrip patch antennas," *IEEE Trans. Antennas Propagat.*, vol. AP-39, pp. 690-694, 1991.

[102] R. E. Colin, *Field Theory of Guided Waves*, McGraw-Hill, New York, 1991.

[103] IE3D User's Manual, ©Zeland Software Inc., 1993-2001.

[104] D. M. Pozar, "A reciprocity method of Analysis of slot-coupled microstrip antenna".

IEEE Trans. Antennas Propagat., vol. AP-34, pp. 1439-1446, 1986.

[105] P. R. Haddad and D. M. Pozar, "Analysis of an aperture coupled patch antenna with a thick ground plane" *IEEE Antennas Propagat. Symp. Dig.*, pp. 932-935, 1994.

[106] D. P. Gray, C. B. Ravipati and L. Shafai, "Corporate fed microstrip arrays with non radiating edge fed microstrip patches," *IEEE Antennas Propagat. Symp. Dig.*, pp. 1130-1133, 1998.

[107] M. L. Oberhart, Y. T. Lo, and R. Q. H. Lee, "New simple feed network for an array module of four microstrip elements," *Electron. Lett.*, vol. 22, pp. 436-437, 1987.

[108] C. B. Ravipati, D. Gray and L. Shafai, "High gain planar antenna candidates: review and design," Internal report, Dept. of Electrical and Computer Engineering, University of Manitoba, 1997.

[109] J. C. Rautio, "MIC simulation column - a standard stripline benchmark," *Int. J. Microwave Millimeter-Wave CAE*, vol. 4, pp. 209-212, 1994.

[110] A. Jentzch and W. Heinrich, "Theory and measurements of flip-chip interconnects for frequencies up to 100 GHz," *IEEE Trans. Microwave Theory Tech.*, vol. MTT-49, pp. 871-873, 2001.

[111] C. R. Paul, *Introduction to Electromagnetic Compatibility*, John Wiley, New York, 1992.

[112] L. B. Gravelle and P. F. Wilson, "EMI/EMC in printed circuit boards-- a literature review," *IEEE Trans. Electromag. Compat.*, vol. EMC-34, pp. 109-116, 1992.

[113] D. Schiavoni, M. Cappio Borlino, M. Giunta, R: Pomponi, and G. Pierucci, "Finite volume time domain technique for evaluation of scattering in GHz-TEM cell," *Proceedings IEEE-EMC Symp.*, Austin, TX, pp. 602-607, 1997.

[114] T. Lapohos, J. Lo Vetri, and J. Seregelyi, "External field coupling to MTL networks with nonlinear junctions: numerical modeling and experimental validation," *IEEE Trans. Electromag. Compat.*, vol. EMC-42, pp. 16-28, 2000.

[115] Bruce Archambeault, and H. Steven Berger, "Susceptibility modeling analysis of parasitics in unshielded products with long wires attached," *Proc. IEEE-EMC Symp.*, pp 459-464, 1996.

[116] R. Gillard, H. Legay, J. M. Floch and J. Citerne, "Rigorous modelling of receiving active microstrip antenna," *Electron. Lett.*, vol. 27, pp. 2357-2358, 1991.

[117] C. Christopoulos, "The application of the TLM method to electromagnetic compatibility studies of systems," *Proceedings IEEE-EMC Symp.*, Austin, TX, pp. 242-247, 1997.

[118] D. Lee and S. Safavi-Naeini, "A wideband closed-form Green's function for multi-layered RF/microwave circuits," *IEEE Elec. Engrg. Symp.*, pp. 861-864, 2000.

[119] A. Torabian and Y. L. Chow, "Simulated image method for Green's function of multilayer media," *IEEE Trans. Microwave Theory Tech.*, vol. MTT-47, pp. 1777-1781, 1999.

[120] F. Y. Chang, "The generalized method of characteristics for waveform relaxation analysis of lossy coupled transmission lines," *IEEE MTT-S Digest*, pp. 821-826, 1989.

[121] A. R. Djordjevic, T. K. Sarkar and R. F. Harrington, "Time-domain response of multiconductor transmission lines," *IEEE Proceedings*, vol. 75, pp. 743-764.

[122] J. E. Schutt-Aine and R. Mittra, "Scattering parameter transient analysis of transimission lines loaded with nonlinear terminations," *IEEE Trans. Microwave Theory Tech.*, vol. MTT-36, pp. 529-536, 1988.

[123] A. R. Djordjevic, T. K. Sarkar and R. F. Harrington, "Analysis of lossy transmission lines with arbitrary nonlinear terminal networks," *IEEE Trans. Microwave Theory Tech.*, vol. MTT-34, pp. 660-665, 1986.

[124] J. E. Schutt-Aine and R. Mittra, "Nonlinear transient analysis of coupled transmission lines," *IEEE Trans. Circuits Systems*, vol. CAS-36, pp. 959-967, 1989.

[125] J. E. Morris, *Electronics Packing Forum*, IEEE Press, Piscataway, NJ, 1994.

[126] Eldo User's Manual, ©Mentor Graphics Corp., 1997-2001.

[127] R. Kaires, "Radiated emissions from printed circuit board traces including the effect of vias, as a function of source, termination and board characteristics," *Proc. IEEE-EMC Symp.*, pp 872-877, 1998.

[128] D. S. Britt, D. M. Hockanson, F. Sha, J. L. Drewniak, T. H. Hubing and T. P. Van Doren, "Effects of gapped groundplanes and guard traces on radiated EMI," *IEEE EMC Symp.*, pp. 159-164, 1997.

[129] W. Cui, M. Li, X. Luo, J. L. Drewniak, T. H. Hubing, T. P. VanDoren and R. E. DuBroff, "Anticipating EMI from coupling between high-speed digital and I/O lines," *IEEE EMC Symp.*, pp. 189-194, 1999.

[130] Y. L. Chow, N. Hojjat, S. Safavi-Naeini and R. Faraji-Dana, "Spectral Green's functions for multilayer media in a convenient computational form," *IEE Proc.*, pt. H, vol. 145, pp. 85-90, 1998.

[131] R. Garg, P. Bhartia, I. Bahl and A. Ittipiboon, *Microstrip Antenna Design Handbook*, Artech House, Norwood, MA, 2001.